

Dichroic Photoemission Electron Microscopy Imaging of Magnetic Surfaces

Dissertation

zur Erlangung des Doktorgrades der Naturwissenschaften
(Dr. rer. nat.)

der

Naturwissenschaftlichen Fakultät II
Chemie, Physik und Mathematik

der Martin-Luther-Universität
Halle-Wittenberg

vorgelegt von

Herrn Maximilian Paleschke
geboren am 16.01.1994 in Halle (Saale)

Gutachter:

Prof. Dr. Wolf Widdra
Prof. Dr. Georg Woltersdorf
Prof. Dr. Wolfgang Kuch

Datum der Verteidigung:

29.08.2022

*“Bridges built for better days, but they won’t hold our weight
The ropes have been wearing thin, entangling in the wind
How’s one meant to grow when walls keep caving in?
The ceiling above us has denied its existence”*

Delta Sleep - Camp Adventure

Abstract

In this thesis, we investigate magnetic surfaces and microstructures via near-threshold photoemission electron microscopy (PEEM). For this purpose, we built a new ultra-high vacuum chamber in combination with several light sources, notably a tunable femtosecond fiber laser setup. This setup offers a unique combination of high spatial and temporal resolution in PEEM. We point out the capabilities of the setup by investigating three material classes and focus on different dichroism contrast mechanisms. First, we present plasmonic dichroism images of propagating surface plasmon polaritons on ferromagnetic alloy microstructures by utilizing the plasmonic spin-Hall effect. Second, we analyze state-of-the-art real-space and k -space images revealing the in-plane and out-of-plane magnetic surface structure of Ni thin films and Fe single crystals, as well as details of the respective $3d$ electron band structure. Third, we discuss and present first preliminary results of linear dichroism PEEM measurements of a NiO single crystal. These findings may pave the way for future ultrafast investigation and manipulation of magnetic systems in general, which in return could be the foundation for future spintronic devices.

In dieser Arbeit werden Ergebnisse der Untersuchung von magnetischen Oberflächen mittels schwellennaher Photoemissionselektronenmikroskopie (PEEM) vorgestellt. Hierfür wurde eine neue Ultrahochvakuumkammer aufgebaut, welche mit unterschiedlichen Lichtquellen ausgestattet wurde, insbesondere einem durchstimmbaren Femtosekunden-Faserlaser. Dieser Aufbau bietet eine einzigartige Kombination aus hoher räumlicher und zeitlicher Auflösung in PEEM. Die vielseitigen Möglichkeiten des Aufbaus werden durch die Untersuchung von drei verschiedenen Materialklassen demonstriert, wobei wir uns auf deren unterschiedliche Dichroismus-Kontrastmechanismen fokussieren. Zunächst präsentieren wir Messungen von frei propagierenden Oberflächenplasmonen auf ferromagnetischen Mikrostrukturen, bei welchen der plasmonischen Spin-Hall-Effekt genutzt wird. Anschließend untersuchen wir Realraum- und k -Raum-Bilder, die die magnetische Oberflächenstruktur von ferromagnetischen Dünnschicht- und Einkristallsystemen sowie die Details der je\(-weiligen elektronischen $3d$ -Bandstruktur aufzeigen. Drittens präsentieren wir erste vorläufige Ergebnisse der Untersuchung des linearen Dichroismus im Antiferromagneten NiO. Die Erkenntnisse dieser Arbeit könnten den Weg für die künftige ultraschnelle Untersuchung und Manipulation von magnetischen Systemen bereiten, welche wiederum die Grundlage für neuartige spintronische Bauelemente bilden könnten.

Contents

Abstract	v
1 Introduction	1
2 Dichroism in Photoemission Electron Microscopy	5
2.1 Photoemission Electron Microscopy	5
2.1.1 Theory	5
Photoemission in the three-step model framework	7
General concepts of PEEM	9
2.1.2 The Femto-PEEM chamber	13
Design & Specs	13
Light sources	16
Performance results	20
2.2 Dichroism Phenomena in PEEM	25
2.2.1 General overview	25
2.2.2 Experimental considerations	26
2.2.3 The problem of defining helicity	27
3 Plasmonic Dichroism in threshold PEEM	29
3.1 Introduction	29
3.2 Theory	33
3.3 Experimental details	37
3.4 Results & Discussion	38
3.5 Conclusion	49
4 Ferromagnetic Dichroism in threshold PEEM	51
4.1 Introduction	51
4.2 Theory	53
4.2.1 Ferromagnetism	54
4.2.2 Domain theory	56
4.2.3 Kerr-like magnetic dichroism	57
4.2.4 Magnetic valence-band dichroism	59

4.3	Experimental details	61
4.4	Results & Discussion	64
4.4.1	Out-of-plane domains on Ni/Cu(001)	64
4.4.2	In-plane domains of Fe(001)	75
4.5	Conclusion & Outlook	82
5	Antiferromagnetic Dichroism in PEEM	87
5.1	Introduction	87
5.2	Experimental details	89
5.3	Results & Discussion	90
5.4	Conclusion & Outlook	93
6	Summary & Outlook	95
A	Preparation of Fe/MgO wedges	I
B	OMNI package for calculating photoemission	V
	Curriculum Vitae	XI
	List of publications	XIII
	Acknowledgements	XV
	Declaration of Authorship	XVII

List of Abbreviations

1PPE	One-Photon PhotoEmission
2PPE	Two-Photon PhotoEmission
AES	Auger Electron Spectroscopy
AF	AntiFerromagnet(ic)
AFM	Atomic Force Microscopy
ARPES	Angle-Resolved PhotoEmission Spectroscopy
BBO	Barium BOrate (BaB_2O_4)
CAD	Computer-Aided Design
CCD	Charge-Coupled Device
CD	Circular Dichroism
CMOS	Complementary Metal-Oxide-Semiconductor
EAL	Effective Attenuation Length
FFT	Fast Fourier Transform
FoV	Field of View
IEF	Imaging Energy Filter
IMFP	Inelastic Mean Free Path
KKR	Korringa-Kohn-Rostoker
LD	Linear Dichroism
LED	Light-Emitting Diode
LEED	Low-Energy Electron Diffraction
LSP	Localized Surface Plasmon
MBE	Molecular-Beam Epitaxy
MCD	Magnetic Circular Dichroism
MCP	MultiChannel Plate
MFM	Magnetic Force Microscopy
ML	MonoLayer
MLD	Magnetic Linear Dichroism
MOKE	Magneto-Optic Kerr Effect
NI	Normal Incidence
NOPA	Noncollinear Optical Parametric Amplifier
PEEM	PhotoEmission Electron Microscopy
PES	PhotoEmission Spectroscopy

PMMA	PolyMethyl MethAcrylate
QMB	Quartz MicroBalance
SAM	Spin-Angular Momentum
SHG	Second-Harmonic Generation
SOC	Spin-Orbit Coupling
SPP	SurfacePlasmon Polariton
SRT	Spin-Reorientation Transition
THG	Third-Harmonic Generation
UHV	Ultra-High Vacuum
UV	UltraViolet
VUV	Vacuum-UltraViolet
XMCD	X-ray Magnetic Circular Dichroism
XMLD	X-ray Magnetic Linear Dichroism
XPEEM	X-ray PhotoEmission Electron Microscopy
XPS	X-ray Photoelectron Spectroscopy
bcc	body-centred cubic
cp	circularly polarized
cw	continuous wave
fcc	face-centred cubic
ip	in-plane
lcp	left-circularly polarized
lp	linearly polarized
oop	out-of-plane
rcp	right-circularly polarized

Chapter 1

Introduction

Big challenges...

The world is currently witnessing several crises and revolutionary developments at once, such as the climate crisis, a global pandemic, a rise in populism and authoritarianism, and also a crisis of neoliberalism leading to more inequality and social disruption. The main reason for this seeming ubiquitousness of problems is the fact that basal certainties in our way of living and growing as a western society have worked for decades, but are now eroding by encountering natural limits, and the systematic shortcomings are starting to pile up in a way that is hard to comprehend in all its complexity [1]. This increasing complexity makes finding easy solutions increasingly difficult. In any case, these developments will fundamentally change our lives more rapidly than they did in the past. One important part of the solution to this riddle will be played by information technology, which has already immensely changed our perception of life, communication, work and research, also at an increasing speed in the past 30 years. Yet, the end of Moore's law again crushes another certainty, which is the exponential scaling of computational power of transistor-based integrated circuits [2]. Here, scaling down this almost 70 years old technology finally hits basic physical barriers, which more and more raises the need for fundamentally different ways to process, store and transport information in a non-transistor-based way. This *need* may be a capitalist one (as will be commented on in the very end of the thesis), but it implies interesting physical challenges and questions, which we will focus on.

...and the slightly smaller ones

Currently, the two most promising candidates for a *post-Moore* world are quantum computing (which we will not cover here) and spintronics, which describes information processing by utilizing the spin of an electron instead of its charge. The spin is a rather elusive, purely quantum-mechanical quantity, determining pretty much all fundamental properties of (fermionic) matter via the Pauli principle (in

conjunction with the classical Coulomb interaction between the electrons carrying the spin). It also causes the emergence of magnetic order in solids, which itself is a cornerstone of all modern information technology devices. Binary information can be encoded in spin-up and spin-down states, and pure spin currents can transport this information without necessarily moving charges. Already, spin currents are generated at frequencies below 10 GHz by electric or magnetic fields or by thermal gradients in spintronic devices made of metals and magnetic insulators [3–5]. Yet, despite its progress, this *low-frequency* spintronics needs to be pushed to ultrafast, i.e. femtosecond or THz, regimes in order to be a viable competition to or addition for conventional CMOS devices.

In 1996, the breakthrough experiment by Beaurepaire *et al.* showed that this push is indeed possible [6]. They measured the ultrafast, sub-picosecond demagnetization of a Ni film, which proved that magnetization dynamics are set by inherently *fast* mechanisms like exchange interaction rather than by *slow* processes like ordinary spin-lattice coupling as previously believed (although recent publications suggest that there also exists an ultrafast phonon excitation channel [7, 8]). This result started an avalanche of further investigations in the following years. The interest in this field gained additional traction after the first successful single-pulse switching of the magnetization of a metallic transition-metal/rare-earth compound without the need for any external magnetic field, which is now coined all-optical switching [9]. In 2011, Radu *et al.* discovered a magnetization inversion of an antiferromagnetically coupled Gd-Fe alloy, where the ferrimagnet undergoes a transient ferromagnetic state upon optical excitation [10]. And from 2014 until today, more and more groups tried to shed light on the fundamental microscopic understanding of the coupling between the spin, electron and lattice subsystems under non-equilibrium conditions induced by ultrafast excitation [11–22].

Our contribution

The research presented here is part of this ongoing scientific endeavor. It is the result of a new project, which started in 2018 as part of the *Ultrafast Spin Dynamics* Collaborative Research Center Transregio 227 with the Free University of Berlin. Our goal is to combine a new photoemission electron microscope (PEEM) with several light sources, especially a tunable femtosecond fiber laser, which allows to unite the high spatial resolution of the electron microscope with the high temporal resolution of the laser setup. As far as the author is aware, this combination together with the already operating angle-resolved photoemission spectroscopy (ARPES) setup provides a worldwide unique in-lab playground for threshold dichroism experiments. This marks a significant contribution to this young and exciting field of research.

Thus, we built a new ultra-high vacuum (UHV) chamber, the so-called Femto-PEEM chamber, based on previous experiences with PEEM in the group [23–25]. The long-term goal is to image and control processes on magnetic samples, including antiferromagnets [26].

Therefore, this thesis presents results contributing to three main fields of our collaborative research, which emphasizes the versatility of the now fully working setup.

First, these results include magnetoplasmonic investigations of $\text{Ni}_{80}\text{Fe}_{20}$ microstructures (Chapter 3), where we utilize the recently discovered plasmonic spin-Hall effect to investigate propagating Surface Plasmon Polaritons (SPPs) on a ferromagnetic metal for the first time. We show clear edge-induced SPPs with sub-micrometer wavelength and propagation length of about $3.5\ \mu\text{m}$ on polycrystalline $\text{Ni}_{80}\text{Fe}_{20}$ microstructures. By this, we get interesting insights into the dielectric properties of the material upon ultrafast optical excitation.

Second, we performed ferromagnetic dichroism imaging of in-plane and out-of-plane domains on Ni and Fe in real and momentum space (Chapter 4). We optimize the contrast of the asymmetry images by consequently applying a group-theory ansatz, which enables an increase in magnetic sensitivity never reported for threshold PEEM measurements. Especially the analysis of energy-resolved k-space PEEM images gives a deeper understanding of the valence-band photoemission process and possible future improvements of this technique.

Third, we present first preliminary results of antiferromagnetic dichroism imaging on NiO single crystals (Chapter 5). We observe a surface photovoltage shift, which causes a contrast in linear dichroism PEEM images. Thus, we support previous publications that the observed dichroism contrast in threshold PEEM is not of antiferromagnetic origin.

We conclude this work with proof-of-principle laser experiments, which pave the way for ultrafast investigation of magnetic states in near-threshold PEEM. In Appendix A, we show preliminary attempts of growing Fe wedges on MgO(100) single crystals, which build the foundation for upcoming time-resolved back-side pump, front-side probe experiments. Additionally, the calculation framework OMNI is briefly discussed in Appendix B, which is relatively easy to set up and use for the interested experimentalist. The OMNI package is a numerical calculation toolkit developed by Dr. Jürgen Henk employing a fully relativistic one-step layer-KKR (Korringa–Kohn–Rostoker) photoemission model [27, 28] in order to simulate expected photoemission currents and asymmetry values. We started to implement it in our group to support our experimental work, which we comment on throughout several parts of this thesis.

Chapter 2

Dichroism in Photoemission Electron Microscopy

This chapter covers the theoretical and experimental concepts necessary to understand the upcoming measurements and discussions. First, the general aspects of photoemission electron microscopy (PEEM) are explained, whereupon the specifics of the newly built setup, the Femto-PEEM chamber, are introduced. Within this context, models to conceptually understand the photoemission process itself are also explained. Additionally, experimental results for common, first-order contrast mechanisms are presented. The chapter concludes with a brief introduction to dichroism techniques in order to investigate second-order contrasts in PEEM, priming the reader for the following chapters. Some standard surface science techniques like LEED, MBE and AES are used throughout this work, but regarding the omnipresent availability of very good literature to these experiments and the secondary importance to our scientific contribution, we kindly point to textbooks by Henzler and Göpel [29], Oura *et al.* [30] as well as Rocca *et al.* [31].

2.1 Photoemission Electron Microscopy

At first, this section deals with PEEM in general, starting from the photoelectric effect and how to generate an image from photoelectrons. After that, we discuss the specifics of the Femto-PEEM chamber in detail.

2.1.1 Theory

The foundation of PEEM is the photoemission process and hence, the photoelectric effect proposed by Einstein [32] and Lenard [33, 34]. The famous Einstein equation reveals that the kinetic energy of the detected electrons E_{kin} scales linearly with the

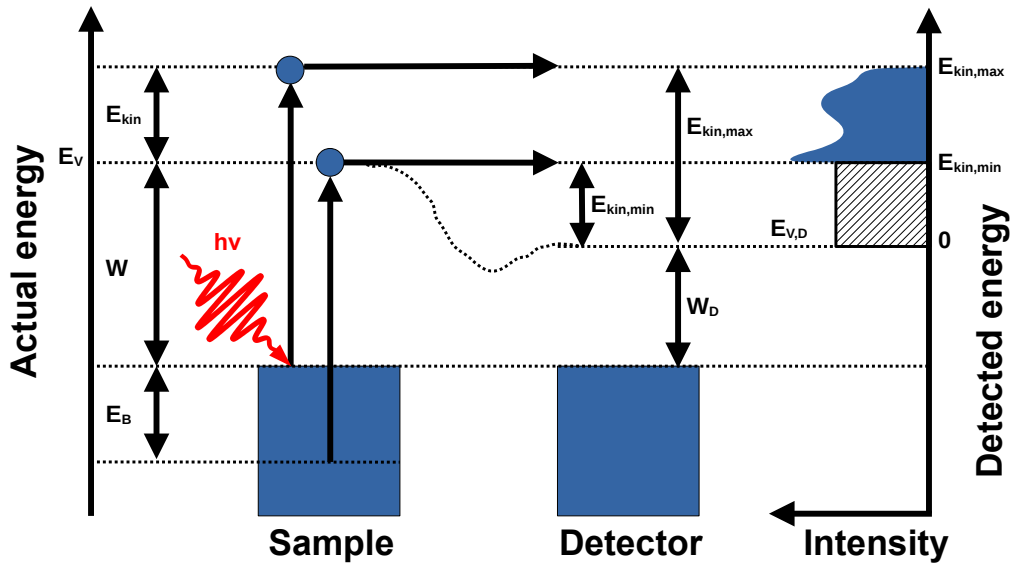


Figure 2.1: Schematic of the photoemission process showing the important energy levels mentioned in the text as well as the influence of the detector. The graph on the right depicts a detected energy spectrum, which differs from the actual energy levels marked on the left. The black hatched box marks the energy region inaccessible by the experiment [35].

frequency ν of the exciting light:

$$E_{kin} = h\nu - W - E_B \quad . \quad (2.1)$$

Here, h is the Planck constant, hence $h\nu$ is the energy of a photon, W is the work function of the surface, i.e. the difference between the Fermi energy E_F and the vacuum level E_V , and E_B denotes the binding energy of the electron, i.e. the difference between the electron energy and the Fermi level. The respective energy levels are shown on the left side of Figure 2.1.

This simple single-electron picture of equation 2.1 correctly describes the photoemission process in a metal. Nevertheless, up to now, we ignored several key properties of electrons such as their momentum k and consequently their k -dependent energy. Electrons have a spin s and they are influenced by exchange interaction and spin-orbit coupling. Thus, the polarization of the exciting photon is important. Considering all these aspects, photoexcitation and photoemission processes are highly complicated, relativistic many-body problems [36]. Generally, two frameworks are discussed when trying to understand and predict photoemission. The first is the simpler three-step model, which is explained in the following. The other is the fully relativistic one-step model based on a spin-dependent Dirac [37, 38] or Hubbard [39, 40] formalism, which generates very good quantitative results calculating the expected photoemission currents for non-magnetic and ferromagnetic metals, respectively [41]. But, suitable (DFT-)calculations providing the necessary information

of the band structure are often not available for a specific system of interest and the formalism is not very didactically appealing, since the concept of a coherent single-step process is hard to grasp on an intuitive level. Besides, this formalism is generally based on a simplified single-particle picture and is often limited to highly symmetric cases [42]. Nevertheless, it is still state-of-the-art to simulate experimental results via these *ab initio* calculations on the basis of local spin-density functional theory and modifications of these models such as the orbital-dependent correction for many-body self-energy effects [43] can extend the applicability of their theoretical predictions. A calculation package currently implemented in the group is briefly described in Appendix B.

Photoemission in the three-step model framework

The three-step model divides the photoemission process in three consecutive steps. First, the incoming photon excites a bulk electron into an unoccupied state above the vacuum level according to the dipole selection rules [44–46]. Second, the electron moves through the bulk to the surface, being exposed to scattering processes. Third, it leaves the bulk by transmitting through the surface potential. It is apparent that all these steps are spin dependent. The excitation process of an electron from an initial many-body state $|\Psi_i\rangle$, perturbed by an electric field, ending up in a final state $|\Psi_f\rangle$ is described by *Fermi's Golden Rule*:

$$I(E_i, E_f, hv) \sim |\langle \Psi_f | \Delta | \Psi_i \rangle|^2 \delta(E_f^N - E_i^N - hv) \quad . \quad (2.2)$$

Here, I is the current of photoemitted electrons, the subscripts i and f mark the initial and final state, respectively, and the superscript N indicates the many-body framework. The δ function describes the energy conservation and corresponds to the aforementioned Einstein equation. The perturbation operator Δ represents the interaction of the incoming light with the initial state electrons. Since the wavelength of light is usually much larger than the distance between the atoms, this perturbation can be described by the dipole approximation:

$$\Delta = E \cdot \boldsymbol{\mu} \quad , \quad (2.3)$$

with $\boldsymbol{\mu}$ being the dipole operator and E the electric field of the exciting electromagnetic wave. This means that initial and final states $|\Psi_i\rangle$ and $|\Psi_f\rangle$ derived from bulk band structure calculations are needed in order to interpret photoemission measurements in detail. These stem from single-particle approximations, hence, equation 2.2 is

adapted in the following manner:

$$I(h\nu) \sim \sum_{i,f} |\langle \Phi_f | \Delta | \Phi_i \rangle|^2 \delta(E_f - E_i - h\nu) = \sum_{i,f} |M_{f,i}|^2 \delta(E_f - E_i - h\nu) \quad . \quad (2.4)$$

Now, $|\Phi_i\rangle$ and $|\Phi_f\rangle$ refer to the single-electron states, and $M_{f,i}$ is the so-called transition matrix element of the dipole selection rules. To be precise, these include the spatial symmetry character of the initial and final state but omit the spin. To include it, which is necessary to describe magnetic materials, relativistic selection rules have to be applied, which are derived for some highly symmetric cases only [47, 48]. During excitation process, the spin of the electron is conserved. With regard to the last step, the transmission through the surface potential, an inclusion of the symmetry breaking properties of the surface is needed. Naturally, the photoelectron changes its momentum k_\perp , but this also depends on the surface structure due to spin-orbit coupling.

This implies to an important conclusion, which is the fact that almost every photocurrent resulting from standard photoemission experiments is spin-polarized [49].

Up to now, we only discussed a so-called one-photon photoemission (1PPE) process, i.e. one photon excites one electron according to equation 2.4. Additionally, two simultaneously arriving photons can also excite one electron, which then incorporates both. When dealing with very high photon intensities and low energies, the probability for these two-photon photoemission (2PPE) processes can become the dominant excitation channel. The subsequent photocurrent is described by:

$$I_{2PPE}(h\nu) \sim \sum_{i,f,m} \left| \frac{\langle \Phi_f | \Delta | \Phi_m \rangle \langle \Phi_m | \Delta | \Phi_i \rangle}{E_m - E_i - h\nu} \right|^2 \delta(E_f - E_i - 2h\nu) \quad . \quad (2.5)$$

The subscript m refers to an unoccupied intermediate state, which is directly probed by this process. Equations 2.4 and 2.5 show that the detected photocurrent scales linearly and quadratically with the light intensity in the case of 1PPE and 2PPE, respectively. This scaling is used to experimentally distinguish both processes.

In conclusion, the three-step model gives an intuitively understandable explanation of the photoemission process. It allows for a qualitative prediction or interpretation of the expected or measured photocurrents when knowing the relativistic band structure and the experimental symmetries.

This already covers the basics of photoemission. The specifics of the second step, i.e. the electron propagation in the material, are discussed in the next section.

Chapter 4 and 5 highlight the impact of magnetization, i.e. exchange interaction, on the photoemission process.

General concepts of PEEM

The general concept of PEEM is the excitation of surface electrons via electromagnetic radiation above the work function and imaging them with an electron microscope. When detecting the electrons, the work function of the detector becomes important. The difference between the sample and detector work function results in an energy range within the photoelectron spectrum which is not accessible. The black hatched box in the spectrum on the right side of Figure 2.1 already illustrates this. Applying a bias voltage to the sample compensates for these work function differences.

There are two different types of PEEM depending on the energy range of the radiation, namely X-ray PEEM (XPEEM) and (near-)threshold PEEM, referring to excitation via an X-ray source, i.e. a synchrotron, or optical light sources, i.e. lasers, mercury discharge lamps, respectively. The term *threshold* refers to the energy required to overcome the work function. Thus, strictly speaking, true *threshold* PEEM is practically impossible, since the photoelectron yield is too low. In practice, the light source defines an energy window close to the threshold, so the term *near-threshold* is more accurate. We use both terms interchangeably throughout this thesis.

The contrast in a PEEM image is the result of local electron yield differences caused by different contrast mechanisms. There are so-called first-order mechanisms, which are directly visible in a measurement. These are [50]:

- Topographic contrast, caused by the topography of the surface changing the local illumination intensity, hence changing the local detected photoelectron yield. Furthermore, electrostatic microfields induced by topographic features significantly influence the photoelectron trajectories. They are almost omnipresent in PEEM images and are more pronounced for oblique angles of incidence. An example is given in Figure 2.10, where the edges of the structure facing the light source appear brighter than the other edges.
- Work function contrast, caused by differences in the surface work function, due to different materials, crystallographic domains or adsorbates, resulting in an increased or decreased photoelectron yield. An example is given in Figure 3.7(d), where the $\text{Ni}_{80}\text{Fe}_{20}$ structure appears much brighter than the GaAs substrate. In general, this is the dominant effect in case of threshold PEEM.
- Chemical contrast, caused by excitation of core level electrons, hence resulting in an element specific absorption of the incoming light. In general, this is the dominant effect in case of XPEEM.

Furthermore, there are second-order contrast mechanisms, which result in a change of the first-order mechanisms due to an additional physical phenomenon. Some of these relevant to this work are:

- Ferromagnetic contrast, caused by a changed photoelectron yield depending on the magnetization of the surface. It is discussed in detail in Chapter 4.
- Ferroelectric contrast, caused by a change in the work function due to ferroelectric domains. This was extensively studied in the group in the thesis of Dr. Anke Höfer [24, 51].
- Light diffraction contrast, caused by topography changes with dimensions similar to the wavelength of the incoming light. It results in an oscillatory change of the photoelectron yield in the vicinity of sharp edges or defects. An example is shown in Figure 2.10 parallel to the bright edges of the Ag structure. The oscillation follows a Bessel function, resulting in a decreasing “wavelength” when looking at the cross section perpendicular to the structure causing the diffraction [52–55].
- Plasmonic contrast, caused by an oscillatory change in the photoelectron yield due to the interference of an excited surface plasmon polariton with the illuminating radiation. It is discussed in detail in Chapter 3.
- Antiferromagnetic contrast, caused by a changed photoelectron yield depending on antiferromagnetic domains at the surface. This contrast mechanism is well known and understood for XPEEM, but is controversially debated in case of near-threshold PEEM and therefore discussed in Chapter 5.

PEEM is rightfully considered a very surface sensitive technique. This statement is often justified by referencing the universal curve of the inelastic mean free path (IMFP) of electrons in bulk, as shown in Figure 2.2(a) [56]. This curve shows a minimum at a kinetic energy of around 10-50 eV, which corresponds to excitation of electrons with a helium lamp (see also Section 2.1.2), resulting in an IMFP of < 1 nm. In this case, photoelectrons detected by PEEM stem from only the topmost layers of the sample, according to this data. However, when looking at our case of threshold PEEM, the kinetic energy of the detected photoelectrons rarely exceeds 1 eV, resulting in an IMFP > 10 nm. In fact, capping layers of several nm of transparent MgO and other materials were successfully used in combination with PEEM studying the underlying layers [59].

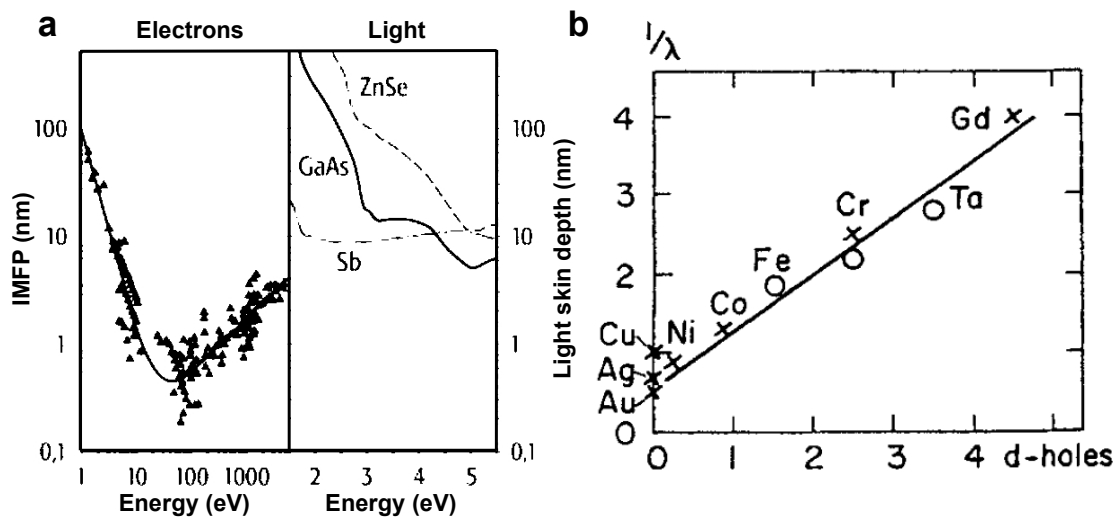


Figure 2.2: (a) The universal curve by Seah and Dench [56] plotting the IMFP of an electron against its kinetic energy when propagating through the material. As every black dot represents a measurement from a different material, the curve is universal in the sense that it is valid for a wide variety of elements. The skin depth of light in different materials depending on the energy is depicted next to the universal curve (taken from reference [57]). (b) IMFP of electrons with < 5 eV in different materials against number of holes in the d band, revealing a linear increase (taken from reference [58]).

However, in most cases, the electron-hole interactions become dominant for very low electron energies. Thus, the universal curve is not an appropriate description for energies < 10 eV as it is by no means *universal* anymore. These interactions are highly dependent on the density of states close to the Fermi level and therefore the IMFP becomes material and spin dependent [60–65]. Hence, for most materials, the escape depth does not exceed a few nanometers in threshold PEEM (but there are exceptions! [66]).

To account for this, Siegmann *et al.* proposed a different rule of thumb for low-energy electrons regarding their effective attenuation length (EAL). It suggests a linear scaling of the EAL with the number of holes in the d band [58, 67]. Despite the staggering lack of reliable data in this energy region, this rule seems to describe $3d$ transition metals and lanthanides very well [68, 69]. It predicts an EAL of a few monolayers for the materials of interest within the context of this work, as depicted in Figure 2.2(b). Additionally, the surface sensitivity stems from the interplay of the experimental geometry and the dominance of the work function contrast. Generally speaking, the work function is an inherent property of the surface and is therefore dependent on reconstructions and adsorbates within the topmost monolayers [51, 70].

A schematic of the standard PEEM electron optics is shown in Figure 2.3. Photoelectrons excited by obliquely incident light are extracted with a high voltage applied by the so-called extractor. This potential gradient reaches up to 15 kV between the sample and the objective lens. Thereby, even slow photoelectrons with a few meV are imaged. The accessible angular acceptance region theoretically covers the full half-space. Furthermore, with the objective lens, the focus point is directly adjusted onto the surface of the sample. Next, the contrast aperture is located behind the objective lens in the objective plane. This aperture imposes an additional limit to the electron acceptance angle. A smaller aperture results in better resolution and lower transmitted photoelectron yield. The adjacent stigmator and deflector correct for astigmatism, pincushion and barrel distortions, after which the field aperture is located within the first image plane. This aperture is important for k-space imaging, since it limits the acceptance region in real space to the desired region of interest. The two subsequent projective lenses produce two magnified images, one between the two lenses and the final one at the imaging unit consisting of the multichannel plate (MCP) and a fluorescent screen. The MCP serves as an electron multiplier while the screen emits light when hit by electrons. Finally, this light signal is detected by a CCD camera. We use an ORCA-Flash4.0 V3 digital CMOS camera (C13440-20CU) by Hamamatsu Photonics. It resolves the imaging unit with 1024×1024 pixels, with 16 bit gray scale intensity levels per pixel. The maximum acquisition time is 10 s per image.

The electrons emitted from the sample are highly sensitive to magnetic field distortions due to their low kinetic energy. This is why a mu-metal shielding encloses the whole PEEM optics and sample stage. Since the interest of this work primarily extends to magnetic samples (see Chapter 4), an active magnetization control would be beneficial. However, the risk of any remanent fields distorting the image as well as space constraints due to the back-side pumping geometry make such a setup a very delicate task. Therefore, we desisted from this possibility.

The amount of magnification can be controlled via the extractor voltage as well as the so-called lens mode. These modes are shown in Figure 2.4. The thesis of Dr. Anke Höfer [51] gives a detailed description of each mode as well as a manual way of switching between these. Figure 2.4(a) shows the two-lens standard mode, covering an FoV range of 10-300 μm in real-space. The three-lens standard mode shown in Figure 2.4(b) is used for high-resolution real-space images, but only covers an FoV of 3-12 μm . Also, the additional second projection lens mirrors the image horizontally and vertically. The telescopic mode shown in Figure 2.4(c) uses an additional transfer lens which leads to a significantly higher FoV range of 50-1000 μm . This is the default mode in most of the measurements, only switching to three-lens mode if very high

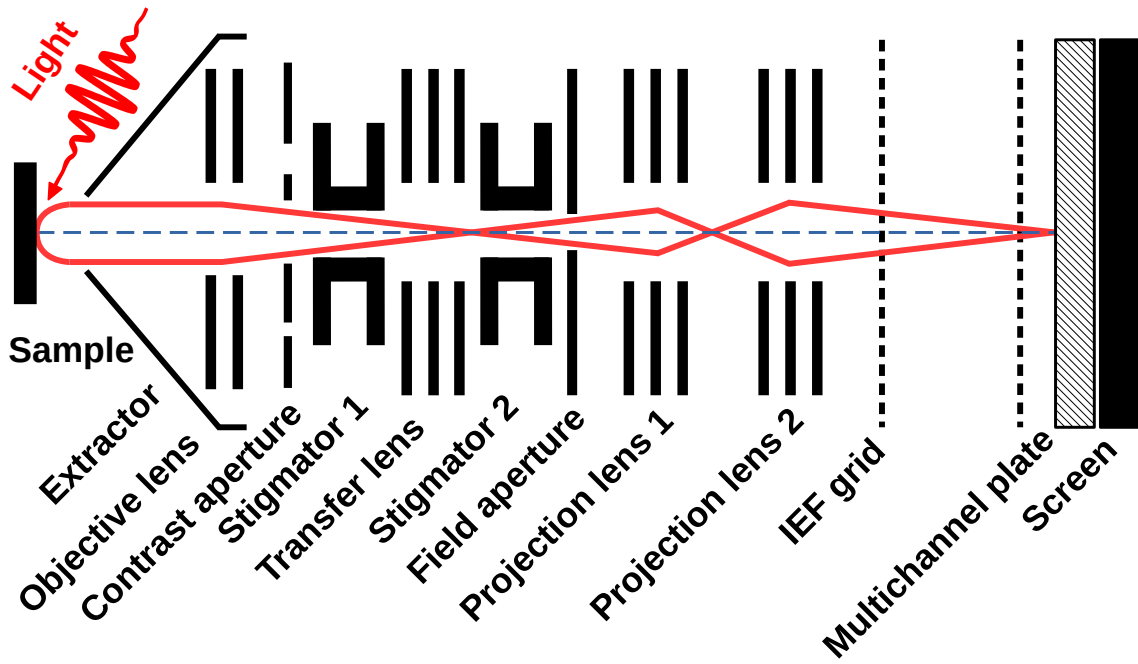


Figure 2.3: Schematic of the general setup of the PEEM electron optics for oblique incidence. Additionally, dashed lines between the second projection lens and the multichannel plate display the retarding grids of the energy high pass filter [50].

magnification and resolution is needed. Last, the k -space imaging mode is shown in Figure 2.4(d), where the lateral angular distribution, imaged in the back focal plane of the objective lens, is projected onto the imaging unit. The maximum accessible wave number k_{\parallel} for this setup is given by:

$$k_{\parallel} = 0.512 \text{ \AA}^{-1} \sqrt{E_{\text{kin}} / \text{eV}} \quad . \quad (2.6)$$

Normally, a desired area of interest is chosen in real space, whereupon the area of investigation is limited via the iris aperture in the first intermediate image plane. This limits the number of collected electrons, minimizes aberrations and increases lateral resolution in k -space.

2.1.2 The Femto-PEEM chamber

Design & Specs

During this thesis, the so-called Femto-PEEM chamber was built. The basic design of the UHV chamber consists of two independent subchambers, the preparation and PEEM chamber, respectively. The goals for the design were threefold: First, the design should enable photoexcitation via different light sources and different directions. This includes standard oblique incidence via mercury-discharge lamp,

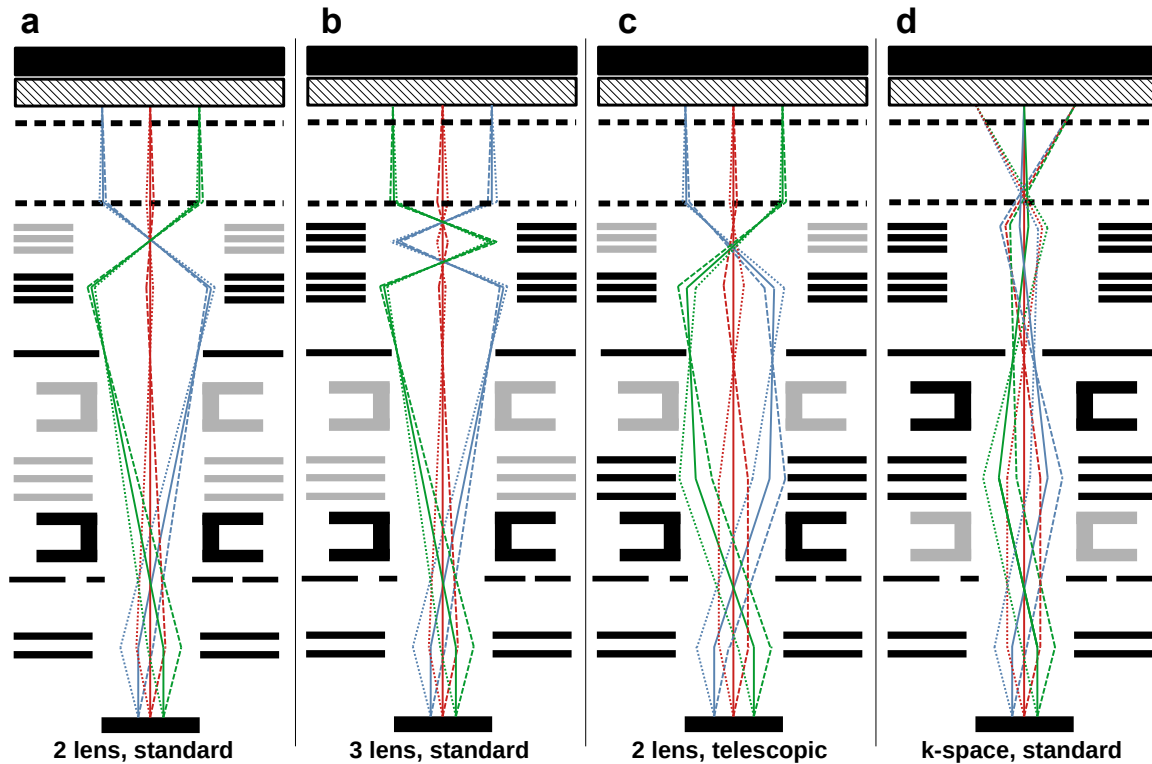


Figure 2.4: Schematic overview of the electron trajectories and lens configurations of the different PEEM measurement setups mentioned in the text. The inactive parts of the electron optics within each mode are grayed out. Redrawn based on information from the FOCUS PEEM manual.

helium lamp and the femtosecond laser system. Additionally, it includes optical excitation via normal incidence (NI) from the front and back side of the sample, the latter through a transparent substrate. Second, all light-controlling optics, especially for the laser, should be placed *ex situ*. And third, the setup should allow future upgrades. Therefore, it already features additional electric feedthroughs for sample heating as well as mounting attachments for liquid nitrogen cooling. The final design was manufactured by Pfeiffer Vacuum Technology AG.

The 3D-CAD model of the Femto-PEEM UHV chamber is shown in Figure 2.5(a). The preparation chamber is mounted with a quadruple MBE evaporator, including Fe, Co, Ni and Au rods, an Ar sputter gun, a manipulator, including a heating stage with active temperature control and a quartz microbalance (QMB), a low-energy electron diffraction (LEED) instrument, an Auger electron spectrometer (AES) and a simple magneto-optic Kerr effect (MOKE) setup consisting of electric coils for in-plane (*ip*) and out-of-plane (*oop*) magnetization. Additionally, the geometry of LEED and AES allows for reflection high-energy electron diffraction measurements. This was successfully tested, but was not used for the characterization of the layer-by-layer growth of the samples shown in this work. Alternatively, we calibrated the sample

thickness via QMB measurements.

All experiments were performed under ultra-high vacuum conditions at a base pressure of about 5×10^{-10} mbar with an NI-PEEM by FOCUS GmbH (Hünstetten, Germany), which has an integrated sample stage, i.e. the sample is mechanically coupled to the electron column, hence reducing drift and vibrations. The PEEM is additionally modified for back-side pumping, shown as the blue path in Figure 2.5. This is achieved by a direct optical path from the view port through the sample stage and the sample holder. The back-side pumping geometry is used to excite a thin film through a transparent substrate, e.g. MgO (see Appendix A). Pumping from the back reduces space charge effects, which, under normal front-side illumination, limit the feasible pulse power and reduce spatial and temporal resolution [71]. Additionally, Figure 2.5 shows the NI excitation path in green, which works via a small mirror inside the electron optics. An *in situ* microslide unit controls the position of the mirror. It is either retraced under standard configuration or completely blocks the electron column. At perfect position, the reflected light impinges the sample under an angle $\theta = 4^\circ$. A unilaterally polished, $(2 \times 2 \times 1)$ mm³ rhodium (100) single crystal works as the reflective mirror. The material handles high temperatures during bake-out of the chamber, and its optical properties are constant over a broad energy spectrum in the visible regime [72]. However, it suffers from low reflectivity for UV light as well as different reflectivity for *s*- and *p*-polarized light. This means that incoming circularly polarized (*cp*) light changes its polarization to an elliptical status after reflection. This renders controlling the polarization on the surface a cumbersome task. The PEEM is additionally equipped with a so-called imaging energy filter (IEF). It consists of two retarding grids between the last projective lens and the imaging unit, as depicted in Figure 2.3. The grids create a retarding field, serving as an energy high-pass filter for the extracted photoelectrons. With this, we achieve an energy resolution of ≈ 100 meV. When performing an energy scan, the voltage between the grids is kept constant, but the sample bias voltage is scanned. Due to the work function difference between the sample and the detector, it is always necessary to apply an appropriate bias voltage. In this work, we denote the IEF cut-off energy with E_B , which means that all electrons up to this binding energy are *integrated*. For example, by choosing $E_B = 0$ eV, only electrons directly from E_F are able to reach the detector, whilst $E_B = 1$ eV integrates all electrons from 0 eV to 1 eV below E_F . Therefore, we can also calculate the contribution of an individual energy slice by subtracting each integrated yield signal from the next energy step. This gives the *differential* yield signal of the respective energy window. Normally, we choose steps of 100 meV. Thus, the differential yield of $E_B = 0.3$ eV is the integrated contribution from 0.2 eV to 0.3 eV.

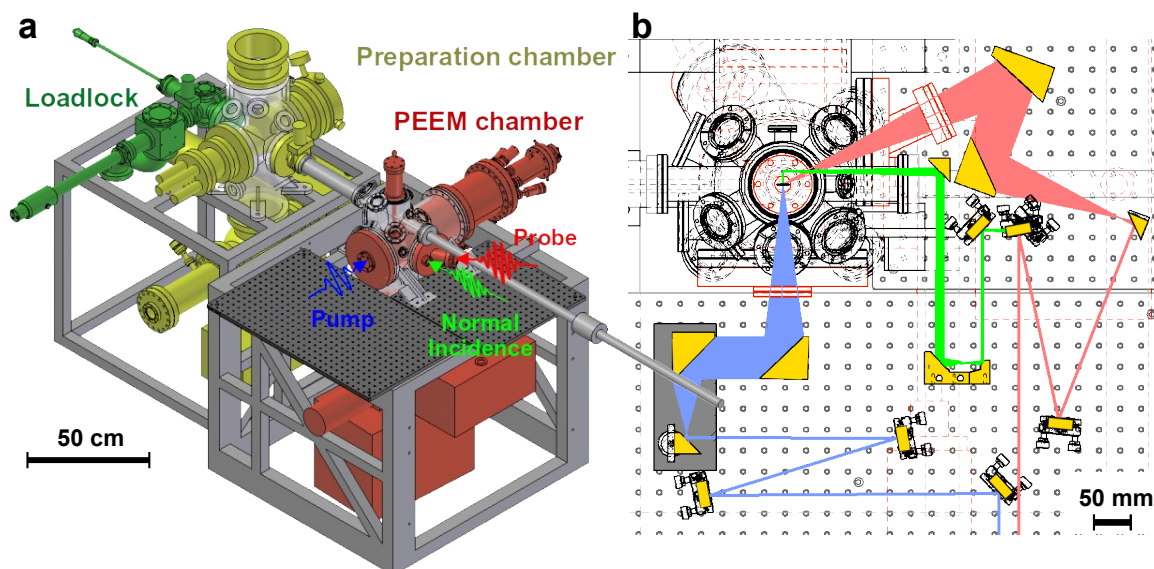


Figure 2.5: (a) 3D-CAD model of the Femto-PEEM experiment with different false colors to indicate the subchambers, with the manipulator on top of the preparation chamber (yellow) hidden. The optical excitation paths accessible by the laser are marked at the PEEM chamber (red) close to its viewports. (b) Schematic top view of the PEEM chamber with the optical components guiding the laser into the UHV chamber via oblique (red), normal (green) or back-side (blue) access.

Light sources

For this work, we implemented three different light sources in combination with the new Femto-PEEM chamber. Exemplary PEEM images are shown in Figure 2.6. These are discussed in the following, starting with the femtosecond fiber laser already used for previous PEEM measurements in the group as well as for several ARPES publications. The mercury discharge lamp (Hg lamp) was specifically implemented for static dichroism imaging and the newly acquired He-I lamp is primarily used for static k -space imaging in combination with the IEF. Lastly, the possibilities of a pulsed laser diode are briefly discussed. The general advantage of all these light sources is their photon energy close to the work function, which results in a very sharp energy distribution of the detected photoelectrons, hence reducing chromatic aberration and increasing spatial resolution [50].

Femtosecond Laser System

The unique feature of the Femto-PEEM chamber is its combination with the tunable femtosecond laser system, which was already used in several works of the group [23, 25, 26, 73–75]. In principle, the system contains a pump fiber laser (IMPULSE, Clark MXR, Dexter, USA) and a double noncollinear optical parametric amplifier (double NOPA, *i-NOPA duo*). For simplicity, the IMPULSE itself is just seen as an elaborate

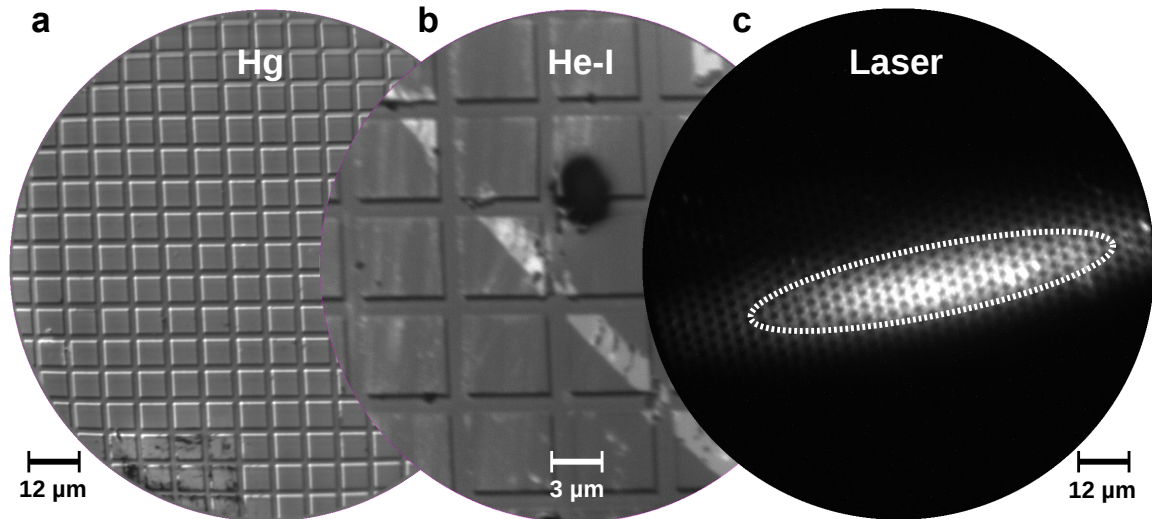


Figure 2.6: Exemplary PEEM measurements using different light sources. (a) Image of an Ag/Si-calibration sample using a mercury discharge lamp (5.2 eV). (b) Image of the same sample using a He lamp (21.2 eV). (c) PEEM image of a Ag/Si-grid sample with smaller pattern using the femtosecond laser system at ≈ 4.45 eV.

light source. For a detailed description, the reader may refer to other publications [76–79]. It creates 200 fs long, linearly polarized (*lp*) laser pulses with a tunable kHz to MHz repetition rate, resulting in a maximum pulse power of ≈ 11 μJ. In this work, we exclusively choose 1.23 MHz.

The laser setup is depicted in Figure 2.7(a) and the accessible pulse energy, power and length are given in Figure 2.7(b). The NOPA was developed by the group of Prof. Riedle at LMU Munich [80]. It provides two separately tunable output wavelengths. This is achieved by splitting the incoming beam coming from the IMPULSE into two arms: One for the generation of a white-light continuum in a rotating sapphire plate, the other for subsequent generation of the second and third harmonic in appropriate birefringent BaB₂O₄ (BBO) crystals (SHG and THG respectively). These beams are then noncollinearly overlapped with the white light inside another BBO. Depending on the phase shift during spatial overlap, the temporal overlap with a specific part of the white-light continuum changes, which determines the amplified photon energy. Two prism compressor lines subsequently compress the two pulses from the NOPA output in time. Two appropriate BBOs can double the photon energy of the respective beams again in order to create UV pulses. After this, another compressor stage is used. Therefore, by simply changing the delay of the white-light pulse compared to the two colors in the NOPA, the energy of the output is correspondingly chosen in a range of 1 eV to 4.8 eV. Once optimized, we can change the wavelength within a few minutes, without massively changing the spatial overlap of the pulses at the experiment. The convenience of this setup cannot be stressed enough (for further

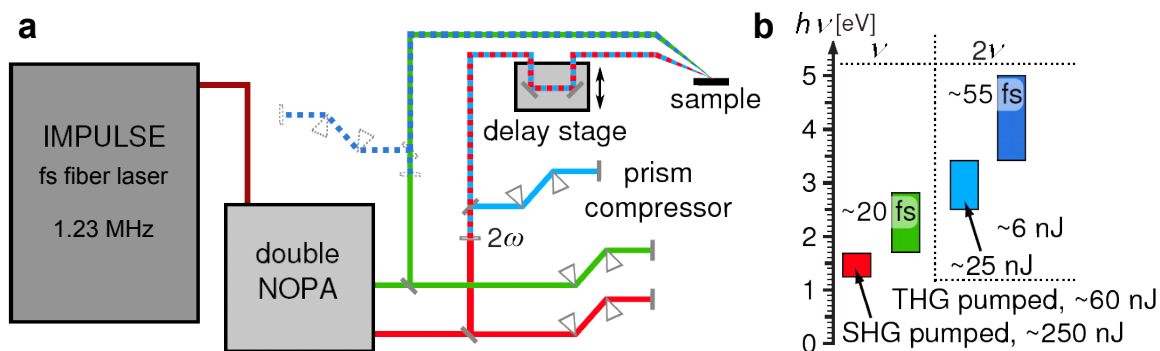


Figure 2.7: (a) Schematic of the femtosecond laser setup, combining a femtosecond fiber laser with a double NOPA and two subsequent prism compressor stages. (b) Overview of the energy range and pulse length available for the respectively coloured NOPA branches (taken from the reference [23, 82]).

details, refer to [23, 73, 81]). The laser beam polarization is adjusted with appropriate achromatic wave plates, which are automatically rotated via a computer-controlled piezoelectric rotation mount for fast polarization switching. We use the ELL14K mount by Thorlabs GmbH which achieves $430^\circ/\text{s}$ rotation speed and an accuracy of 0.1° , but suffers from low durability due to the delicate piezoelectric drives. Space charge effects are avoided by reducing the pulse power to ≈ 1 nJ. In case of dichroic imaging, the yield for each polarization direction is accumulated for approximately 30 min to obtain a sufficient signal-to-noise ratio. Via the rotation mount, the light helicity is automatically alternated every 10 s in order to suppress long-term drifts of the laser intensity, which enhances the quality of the dichroic signals. Via a movable, three-inch parabolic mirror, the laser spot size on the sample can be varied down to a diameter of $10\ \mu\text{m}$, i.e. the minor axis of the ellipse in Figure 2.6(c). The position of the mirror with respect to the sample surface is suitably chosen to illuminate the full FoV as well as to avoid space charge effects.

Mercury discharge lamp

The mercury discharge lamp is the standard source for static imaging in PEEM. It is a reliable cw source of UV light. It uses an HBO 103W/2 mercury short-arc lamp to generate an extreme high luminance of $1700\ \text{cd}/\text{mm}^2$, one third of which is in the UV region of the energy spectrum. This output power can be attenuated via a 1:10 and 1:100 neutral density filter. The peak energy in the UV spectrum is located at 5.2 eV. Wavelengths longer than 280 nm are dumped by a heat filter, which is basically a beam-splitter reflecting UV light. Thus, the output of the lamp has an inhomogeneous polarization distribution. The UV light is filtered by a Glan-Taylor polarizer, which guarantees a reliable polarization configuration. The angle of the

polarizer axis is calibrated to the maximum photoelectron yield in PEEM, which corresponds to the p -polarization state. After that, the same rotation mount setup as for the femtosecond laser system is used, where appropriate $\lambda/2$ and $\lambda/4$ -wave plates generate linear and circular polarization, respectively. Finally, the output of the lamp is focused by an *in situ* lens, which results in an illumination spot of ≈ 3 mm on the sample surface. Figure 2.6(a) shows an example for a calibration measurement of a Ag film on patterned Si(100), revealing the aforementioned contrast mechanisms, predominantly topography and work function contrast.

Helium-I lamp

We use a customized HIS 14 Helium-lamp by FOCUS GmbH as a source for high flux vacuum-ultraviolet (VUV) *cw* light at 21.2 eV. The lamp is a capillary discharge tube of the principle proposed by Schönhense *et al.* [83]. It is connected to a pure helium gas inlet and two subsequent differential pumping stages. Despite these precautions, some helium will be leaked into the PEEM chamber, increasing the base pressure to 5×10^{-9} mbar while operating. A high voltage supply ignites the gas inside the lamp cavity, which then forms a stable discharge plasma. In theory, any other noble gas like Ne or Ar can be used in the device for creating even higher photon energies. The average intensity output is roughly the same, reaching $\approx 10^{11}$ photons/s, but the discharge properties, i.e. ignition pressure and voltage, are not as stable as for He-I. An example for a He-I PEEM measurement is shown in Figure 2.6(b), where the difference in excitation photon energy is apparent in the changed chemical contrast when comparing the image to the mercury discharge lamp measurement shown in Panel (a). Additionally, the HIS 14 is equipped with a gold coated toroidal focusing mirror, increasing the photon density on the sample. The focus spot diameter is $\approx 300\mu\text{m}$, as proven by Figure 2.8. The mirror is mounted at an oblique incidence angle, which reduces aberrations but introduces a small amount of p polarization to the otherwise unpolarized, incoherent beam.

Pulsed LED

As an intermediate and flexible tool for illumination, we also implemented a pulsed laser LED. We use a PLS 255 laser head driven by a PDL 800-D laser driver of PicoQuant GmbH, which creates UV laser pulses at 4.86 eV with a width of 700 ps. Advantages are the small size of the device, the absence of any external cooling and the repetition rate which can be changed and triggered very easily. The latter is completely flexible, covering a range from *cw*, to single pulse, to the highest repetition rate of 10 MHz. The downsides are the incoherence, the small power of about 1 pJ

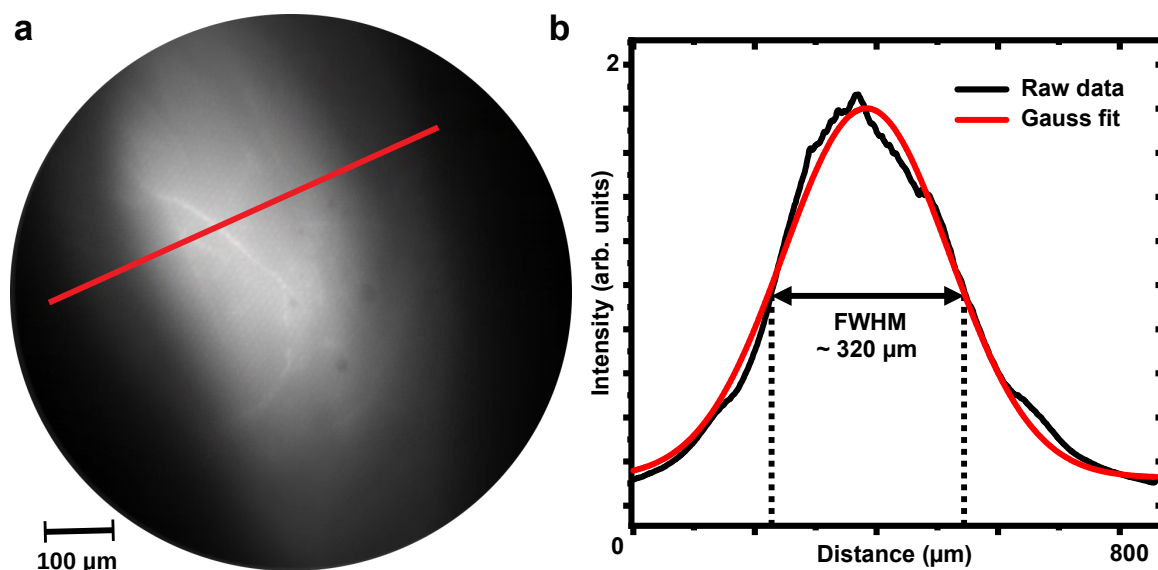


Figure 2.8: (a) PEEM image of the VUV light spot of the HIS 14 on a silver surface. (b) Cross section of the area marked in (a) by the solid red line, revealing the maximum focus of the helium lamp.

per pulse and the high divergence of the beam. Because of this, additional focusing optics are a necessity. These devices are normally used for time-resolved fluorescence experiments, but also suit simple proof-of-principle photoemission experiments, where a pulsed excitation is needed without going through the calibration process of the whole femtosecond laser setup.

Performance results

A LabView program provided by FOCUS GmbH is used (intelliPEEM software) for data acquisition of PEEM images, which implements many quality-of-life features like the one-button switching between the imaging modes shown in the last section. The PEEM images are subsequently processed via ImageJ2 [84] (or rather its scientific flavor Fiji [85]) or OpenCV Python routines [86], whereas the extracted data from these images is either further processed in Python or OriginPro [87].

As explained in Section 2.1.1, the photoelectrons excited above the vacuum level by a light source are extracted by an electron lens column and focused onto an MCP, after which a fluorescent screen transfers the electric signal into an optical signal, which is finally measured by the CCD camera. One downside of this technique is the double MCP, which always imprints its structure onto every PEEM image. Depending on the overall brightness and acquisition time, this MCP structure, resembling a honeycomb pattern of varying size and intensity, is often the dominant feature in a live PEEM measurement. Figure 2.9(a) shows a raw PEEM image of a patterned Ag sample. Here, the topography contrast is superimposed by the contribution of the

MCP structure. Thus, it is very difficult to give an interpretation of weaker contrast mechanisms during live imaging. To correct for this MCP contribution, a so-called bright-field image is taken. This calibration measurement is done with the exact same PEEM lens settings, whilst only changing the focus point to a higher level above the surface, hence defocusing the image. An example is shown in Figure 2.9(b). Ideally, such an image is taken after each measurement, since the brightness of the MCP structure changes nonlinearly with the photoelectron yield.

Additionally, the CCD chip itself has a different black-level threshold for every pixel, which is apparent during low intensity measurements. This is easily corrected by measuring a so-called dark-field image. Therefore, we take images for all common acquisition times while the MCP and screen are turned off. An example is shown in Figure 2.9(c). These dark-field images are stored and subtracted during any subsequent live image acquisition. This database is regularly updated after extensive use of the camera, since the CCD pixels tend to degrade over time.

Both images, dark and bright-field, are needed to correct raw PEEM images via the following formula:

$$I_{\text{cor}} = C \cdot \frac{I_{\text{raw}} - I_{\text{dark}}}{I_{\text{bright}} - I_{\text{dark}}} . \quad (2.7)$$

Here, I_{cor} , I_{raw} , I_{dark} and I_{bright} are the pixel gray value of the corrected, raw, bright-field and dark-field PEEM image, respectively. C is a normalization constant which is set to the ratio between the mean gray value of the area of interest of the raw image and the bright-field image. An example for a background-corrected PEEM image is shown in Figure 2.9(d). The Ag/Si-pattern is clearly visible, with a homogeneous intensity on top of and in between the squares. Nevertheless, the shortcomings of this technique become obvious, too. Samples with high contrast differences now contain a “shadow” of these sharp structures due to the correction with a defocused image, since we cannot infinitely defocus the image without decreasing the brightness in the process. In Figure 2.9(d), this “shadow” is apparent in the vicinity of the bright edges on the right and bottom corner of the squares, which now encompass a 2 μm wide brighter rim. On the other hand, if the photoelectron yield is too low in the first place, this correction tends to overcompensate the MCP structure. So, ideally $I_{\text{bright}} \gg I_{\text{dark}}$. Standard PEEM images shown in the rest of this work are all background corrected.

Prior to every experiment, the PEEM lens parameters are optimized via calibration measurements with the mercury discharge lamp. In a best-case scenario, the Femto-PEEM easily achieves 20 nm spatial resolution. This value is defined by the scale parameter σ , which is the square root of the variance of a normal distribution. To calculate it experimentally, a cross section line scan of a step edge is measured, causing a defined topography or work function contrast. The spatial distribution of

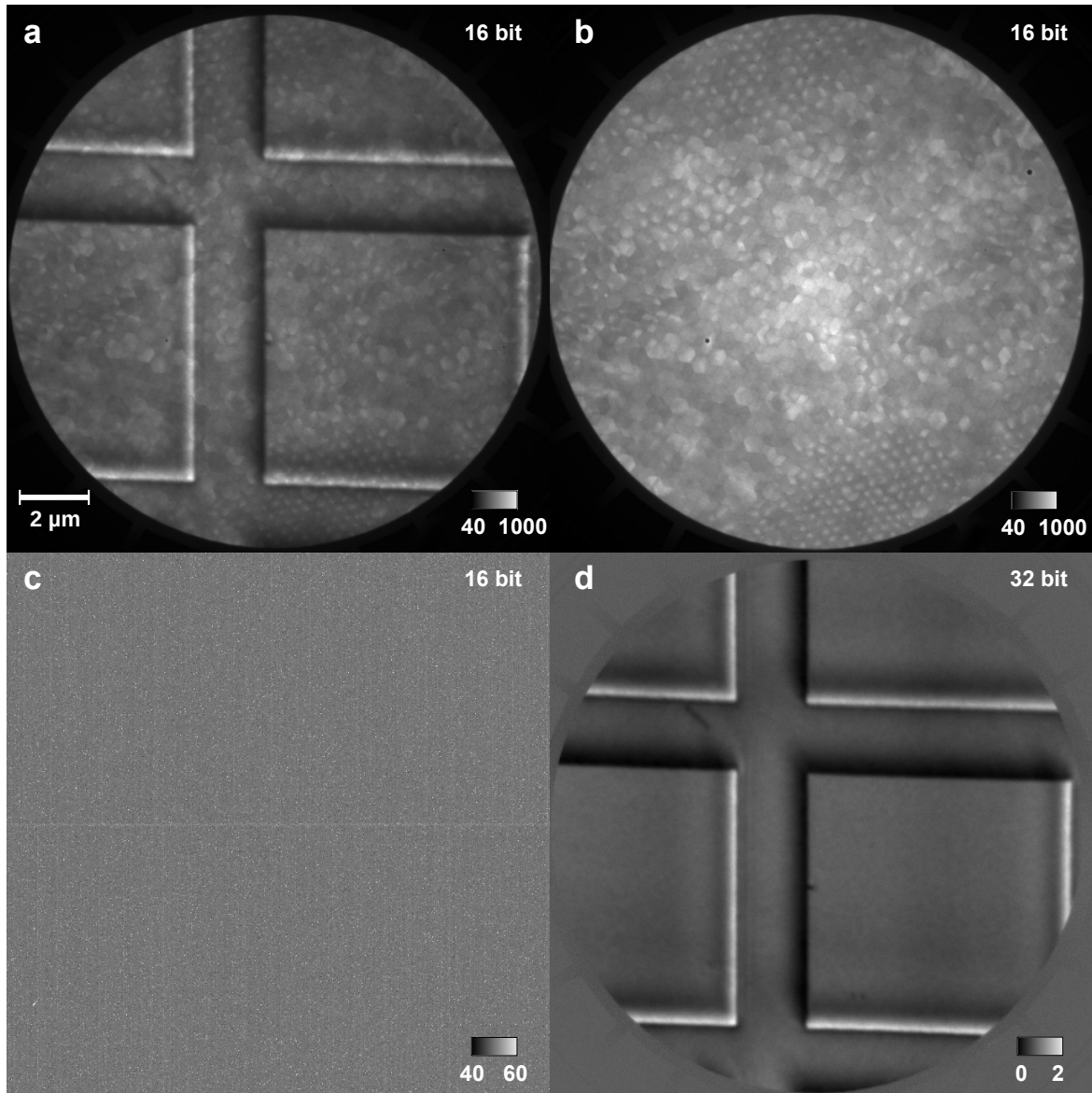


Figure 2.9: (a) Raw PEEM image at 5.2 eV of a patterned Ag/Si-calibration sample. (b) Defocused PEEM image of the same area. This is the so-called bright-field image. (c) Image transferred by the CCD camera when screen and MCP are turned off. This is the so-called dark-field image. (d) Background-corrected PEEM image, calculated with the data from (a)-(c) according to equation 2.7.

the total photoelectron yield signal is fitted by an error function $\text{erf}(x)$, which is the cumulative distribution function of the normal distribution. Hence, the following equation is used to fit the line scan:

$$I(x) = a + b \cdot \text{erf}\left(\frac{x - c}{\sigma\sqrt{2}}\right) \quad (2.8)$$

Here, a , b and c are free fit parameters, $I(x)$ is the photoelectron yield at position x of the respective line scan. Figure 2.10 shows a PEEM image of a silver film on a

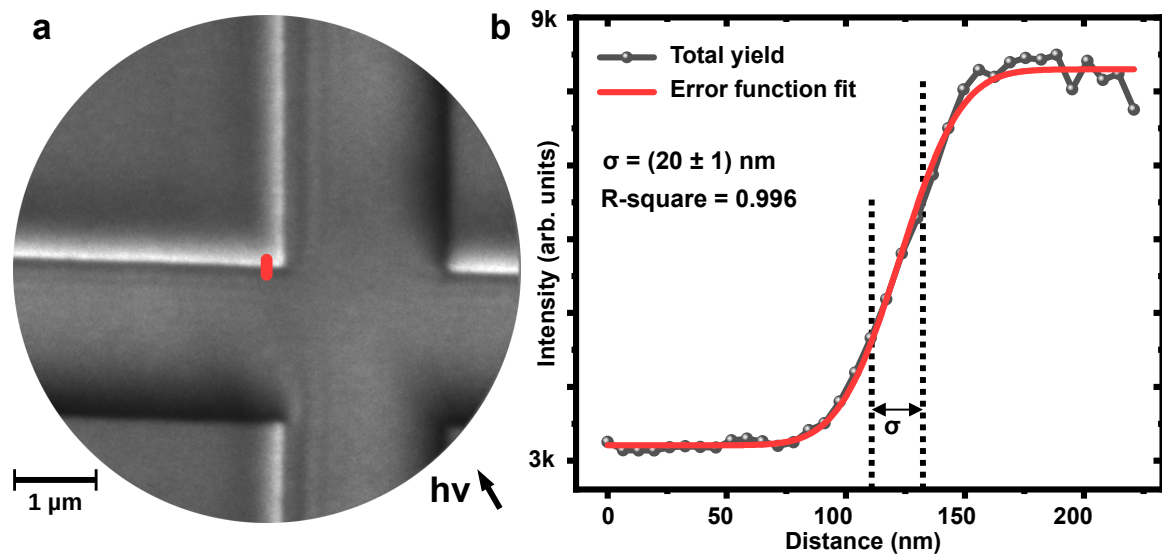


Figure 2.10: (a) PEEM image of a patterned Ag/Si-calibration sample provided by FOCUS GmbH. (b) Line scan of the area marked by the red line in (a), showing a step edge fitted by the error function (see equation 2.8). The 20 nm scale parameter σ is marked accordingly in the graph. The scales of the Ag structures are given in the text.

patterned Si substrate used for such calibration purposes. The squares are 300 nm in height, have a lateral size of $(8 \times 8) \mu\text{m}^2$ and are arrayed with $10 \mu\text{m}$ pitch.

The physical limit of the spatial resolution of the instrument is mainly determined by chromatic and spherical aberrations of the objective tube lenses. In a real measurement, other factors like the topography and illumination angle also play a role. Counterintuitively, the addition of the IEF grids *improves* the spatial resolution of the microscope. They cause a parallelization of the trajectories of the incoming electrons between the last projective lens and the MCP. Hence, the filter is used in almost all measurements within this work, even if no energy filtering is required.

This way of determining the spatial resolution in PEEM gives a good estimate of what to expect from a realistic experiment in general. However, depending on the applicable contrast mechanism, the morphology of the sample and the angle of illumination and polarization, the achieved resolution may be drastically different. Besides, using a topographically patterned sample is inherently flawed when seeking maximum spatial resolution due to natural broadening of the electron beam at a step edge. Therefore, a surface with a sharp work function contrast might serve as a better calibration tool for determining the best achievable resolution as compared to a sharp topographic change.

Nevertheless, the setup built during this work marks a significant upgrade to the existing capabilities of the group. The interplay of increased spatial resolution and several quality-of-life improvements regarding the handling of the sample and

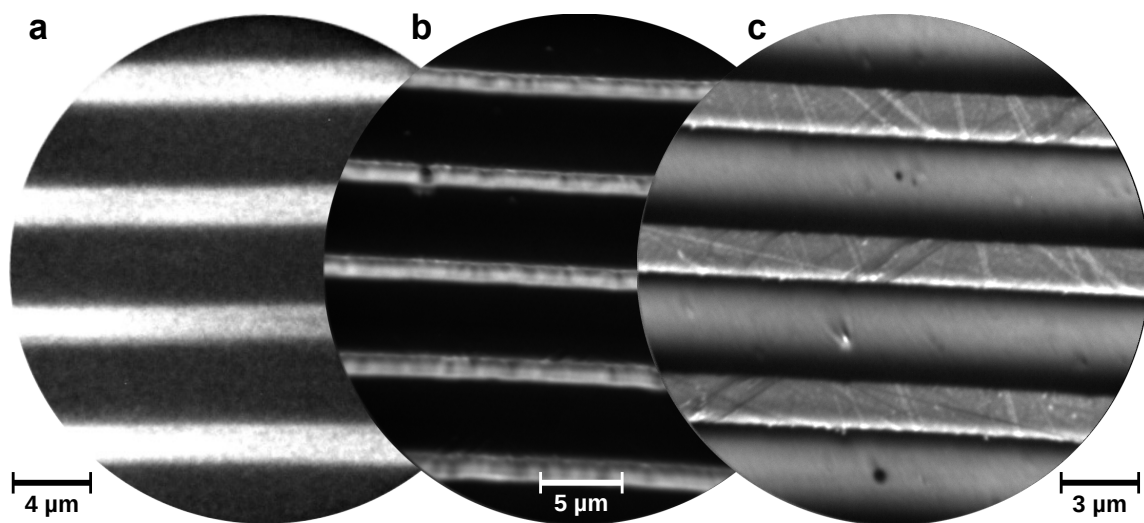


Figure 2.11: (a) PEEM image of Pd stripes on Si measured by Dr. Anke Höfer at the old setup (taken from the reference [51]). (b) Same sample measured with the new Femto-PEEM system and with the aperture aligned off-axis in the vertical direction. (c) Same sample and position, zoomed-in with correctly aligned aperture.

the microscope results in better quality images and an easier interpretation of the gathered data. A striking example is depicted in Figure 2.11. Here, panel (a) shows a PEEM image measured by Dr. Anke Höfer with the old PEEM setup [51], presumably revealing a work function contrast between the bright Pd stripes and the dark Si substrate. With the new Femto-PEEM, we notice that the observed contrast stems from the aperture diaphragm not being perfectly centered. Figure 2.11(b) shows the same sample measured in the Femto-PEEM setup with the 70 μm aperture positioned slightly off-axis. In panel (c) we see the same position with properly aligned aperture. There is still a work function contrast visible, but the topography of the stripes is clearly the dominant contribution here.

In conclusion, the Femto-PEEM chamber is a combination of a state-of-the-art, high-resolution PEEM with various modifications for different excitation directions, wavelengths and polarizations as well as energy filtering capabilities. The ultrashort time resolution offered by the femtosecond laser system makes this a worldwide unique setup for studying ultrafast electron dynamics in k- and real-space on femtosecond time and nanometer length scales.

2.2 Dichroism Phenomena in PEEM

The term *dichroism* was originally used to describe the polarization dependence of the absorption of light in birefringent crystals [88]. Within the context of photoemission, this term is used in a more general way. Section 2.1.1 introduced the dependence of the detected photoelectron yield on the light polarization and direction of incidence, as well as on the electron band structure and surface morphology. In this sense, *dichroism* refers to a change in the photoelectron yield, when changing one of the experimental parameters breaking spatial or time-reversal symmetry. These are for example the momentum of the incoming photon q , the momentum of the photoelectron k , the polarization of the incoming light P or the magnetization of the sample M . Whether a change in an experimental parameter changes the photoelectron yield depends on the specific dichroism mechanism at hand. In the following, some dichroism phenomena in context of PEEM measurements are discussed. The detailed explanation for the origin of the plasmonic, ferromagnetic as well as antiferromagnetic dichroism is given in Chapter 3, Chapter 4 and Chapter 5, respectively.

2.2.1 General overview

Whenever we talk about dichroism in the context of PEEM, we imply that there is a so-called asymmetry value A left when comparing two measurements. This asymmetry can occur when the detected intensity I changes to I^* upon changing one experimental parameter of the photoexcitation setup or the sample. The general formula for calculating A is

$$A = \frac{I - I^*}{I + I^*} . \quad (2.9)$$

Since an asymmetry value reveals small changes between two consecutive measurements, it is the norm rather than the exception. Hence, dichroism imaging is a common technique used to identify physical properties and dynamics hidden within static experimental conditions. For example, it is possible to detect ferromagnetic in-plane (*ip*) and out-of-plane (*oop*) domains by changing the polarization of the exciting light, or by switching said domains to a different magnetic state via an external magnetic field. These changes to the experimental setup can also be applied indirectly by electric or spin currents or strain. Furthermore, it is possible to detect ferrimagnetic, ferroelectric or plasmonic properties by changing one of the respective parameters and calculating the asymmetry [89–94]. There is even the possibility to detect antiferromagnetic domains via dichroic measurements in XPEEM [95, 96].

A common setup for imaging ferromagnetic domains in PEEM via oblique incidence is circular dichroism (CD). In this case, all experimental parameters are kept

constant and only the helicity of the exciting light is switched from left-circularly polarized (*lcp*) to right-circularly polarized (*rcp*). Hence, equation 2.9 is specified as follows:

$$A = \frac{I_{lcp} - I_{rcp}}{I_{lcp} + I_{rcp}} . \quad (2.10)$$

Here, I_{lcp} and I_{rcp} are PEEM intensities measured for excitation with *lcp* and *rcp* light, respectively. A helicity dependent signal results in a non-vanishing asymmetry value A contributing to the dichroic PEEM image. Again, other factors despite magnetization can cause such dichroic contributions. Some of these factors are discussed in the following section.

2.2.2 Experimental considerations

All the aforementioned effects can be defined as *dichroic* in the context of PEEM, although they do not necessarily include an optical, i.e. birefringent, change. It is therefore important to carefully interpret asymmetry values, since they can be of fundamentally different origin. A misaligned wave plate may also result in asymmetry, which might be misinterpreted as being of dichroic origin (see discussion in Chapter 3). Hence, it is key to carefully exclude other influences caused by the experimental setup like temperature drifts, misalignment of optics, mechanical vibrations, or changes in the sample's position, morphology or purity. Therefore, higher acquisition times might increase the quality of a single measurement by averaging over longer time scales, but it often reduces the quality of the subsequent asymmetry image. In case of the Femto-PEEM chamber and within the context of this work, we exclusively change the polarization of the light between measurements while keeping all other parameters fixed.

Two experimental aspects of the different light sources are apparent when performing wave plate angle scans as depicted in Figure 2.12. The laser data in panel (a) reveals a sinusoidal change of the photoelectron yield, averaged for half an hour, with the $\lambda/2$ wave plate angle. But, due to the 2PPE process and drifts of the laser power, the intensity of a single measurement can vary drastically, as shown by the light gray dots. In Figure 2.12(b), a $\lambda/4$ wave plate changes the intensity in a sinusoidal manner, too, but with doubled frequency and considerable deviations from the fit at higher angles. These deviations stem from the Hg lamp used here, since the additional optics (mirror and focus lens) cause an additional modulation of the output intensity of the lamp with respect to the chosen polarization. Comparing the two light sources in (a) and (b) reveals the very good polarization control for the laser light whilst needing to average over long times in order to reduce drifts. Contrary, the Hg lamp is not affected by drifts but suffers from a weakly defined polarization state.

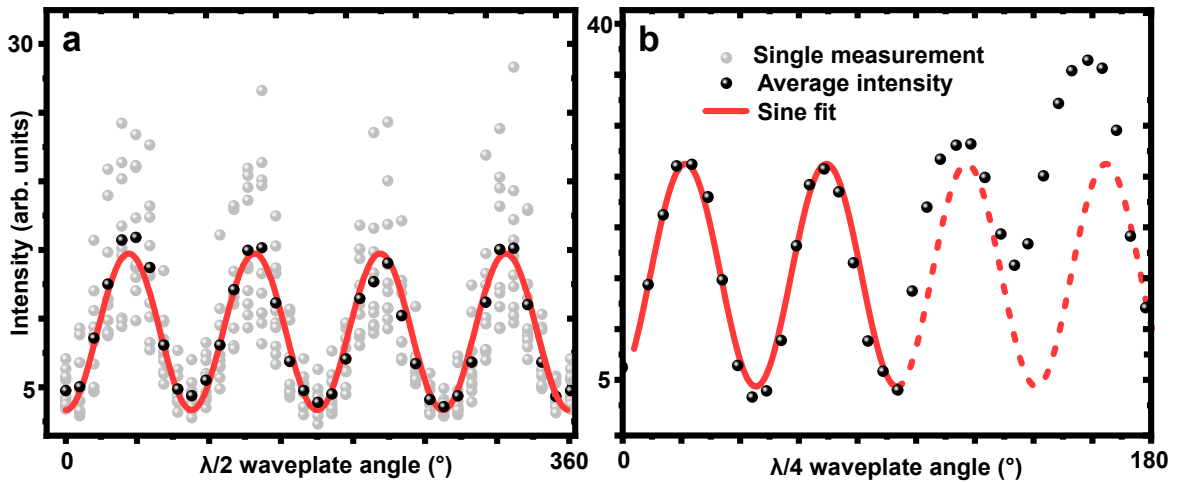


Figure 2.12: (a) Average photoelectron yield versus $\lambda/2$ wave plate angle for femtosecond laser pulses with 3.32 eV on a GaAs substrate, resulting in a regular sinusoidal change whilst the single measurements spread over a large intensity range. (b) Same scan with a $\lambda/4$ wave plate and a mercury discharge lamp on an Ag surface, revealing no intensity drifts between measurements but deviations from the sine fit (red solid/dashed line) at higher angles.

2.2.3 The problem of defining helicity

We want to briefly address one problem of an experimentalist often overlooked regarding the definition of the helicity of a light source. The linear polarization state is easily checked with a standard polarizing filter or, in case of UV light, a Glan-Taylor prism. The experimental validation of the circular polarization state is somewhat more complicated. In a simple picture, *cp* light can be described as the superposition of two linearly polarized waves propagating in $+z$ direction and oscillating in the xz and yz plane, respectively, whereby one is shifted by a phase of $\lambda/4$ in relation to the other. Starting from a linear polarized state, a $\lambda/4$ wave plate is used to retard one of the two contributions. When the angle between the optical axis of the wave plate and P is 45° , the result is a *cp* wave. But, it is not trivial to tell, if the resulting circular wave is *lcp* or *rcp*.

First, this depends on what we actually mean by *lcp* and *rcp* [97]. In other words, these terms refer to the handedness of the circular wave. The wave itself is circular in the sense that the electric field vector E rotates in time, and therefore also in space. We can now define the handedness as the direction of rotation of E as seen by the source or by the receiver, i.e. our sample, which corresponds to looking in the $+z$ or $-z$ direction. Generally speaking, in most physics publications, the helicity is defined in $-z$ direction, since this accurately resembles the impact of the light on the sample. In engineering, it is often the other way around. To add to the confusion, some define the helicity not by handedness but via the screw convention, i.e. the chirality of the shape E traces when propagating in space, which confusingly leads to the opposite

sign when defining *lcp* and *rcp*. In many publications, the convention used is not properly named or defined. This negligence stems from the fact that the specific helicity, i.e. the direction of the spin-angular momentum (SAM) vector, does not really matter in most cases. Hence, the question of left and right just becomes a question of changing a sign. But, in some instances, the physical impact of this SAM is actually very important, which is apparent in Chapter 3.

Second, most manufacturers only specify the direction of the fast axis of their optics, which tells nothing about the convention at hand. In case of the two manufacturers inquired within this work, the screw convention was said to be used without guarantee. In order to check the resulting SAM direction after the wave plate, a Mach-Zehnder interferometer can be used, as shown in the PhD Thesis of Philip Alexander Kahl [98]. Alternatively, the Stokes polarization parameters of a given wave plate can be determined with a set of polarizing elements [99].

Third, there is a difference between the polarization impinging on the sample and the polarization within it [100].

In the context of this work, we define *lcp* in the handedness convention looking in $-z$ direction, which is equivalent to having the fast axis of the $\lambda/4$ wave plate oriented -45° from the light polarization axis (counter-clockwise) when looking in $+z$ direction. Before CD PEEM measurements, we perform a wave plate calibration as shown in Figure 2.12. Once the wave plate scan is a regular sine wave, we start from a linear polarized state, where the maximum photoelectron yield in PEEM marks the p-polarized state. Introducing the $\lambda/4$ wave plate, we define the minima at -45° as *lcp* and $+45^\circ$ *rcp* light.

Chapter 3

Plasmonic Dichroism in threshold PEEM

This chapter deals with the imaging of surface plasmon polaritons propagating in magnetic materials via near-threshold PEEM. This topic is introduced by a short literature review, after which we present our experimental approach and discuss subsequent results. We conclude the chapter with an outlook on upcoming magneto-plasmonic experiments.

3.1 Introduction

Simply put, a plasmon is a collective excitation of the electron bath of a metal. Therefore, when talking about plasmons, the specific topic is either bulk plasmons, localized surface plasmons (LSP) or surface-plasmon polaritons (SPP) [101], as schematically depicted in Figure 3.1(a). Since the first is a bulk phenomenon, it is not of interest for the upcoming discussions. The latter two are intrinsically connected to the surface and are thereby dominant effects often appearing in PEEM measurements. Hence, when loosely using the word *plasmons* in the following, it is implied that this refers to either LSPs or SPPs.

The first observation of plasmonic field enhancement in PEEM via LSPs was documented by Cinchetti *et al.* [102, 103]. Before that, spatially-resolved measurements of plasmons were mostly limited to photon scanning tunneling microscopy, which suffered from complicated plasmon-excitation setups and long data-acquisition times [104–108]. In 2007, Kubo *et al.* [109] managed to excite and image propagating SPPs on silver and gold via a simple step-edge geometry. At the same time, Chelaru *et al.* observed similar dynamics on Ag nanowires [52, 110]. From there on, almost all plasmonic investigations were performed on these two noble metals, due to their ideal optical properties favoring low damping and a high SPP quality factor [111]. Thereby, the propagation length of an SPP in silver can exceed several tens of micrometers [107, 112–114]. Conventionally, the plasmon dispersion relation is used for

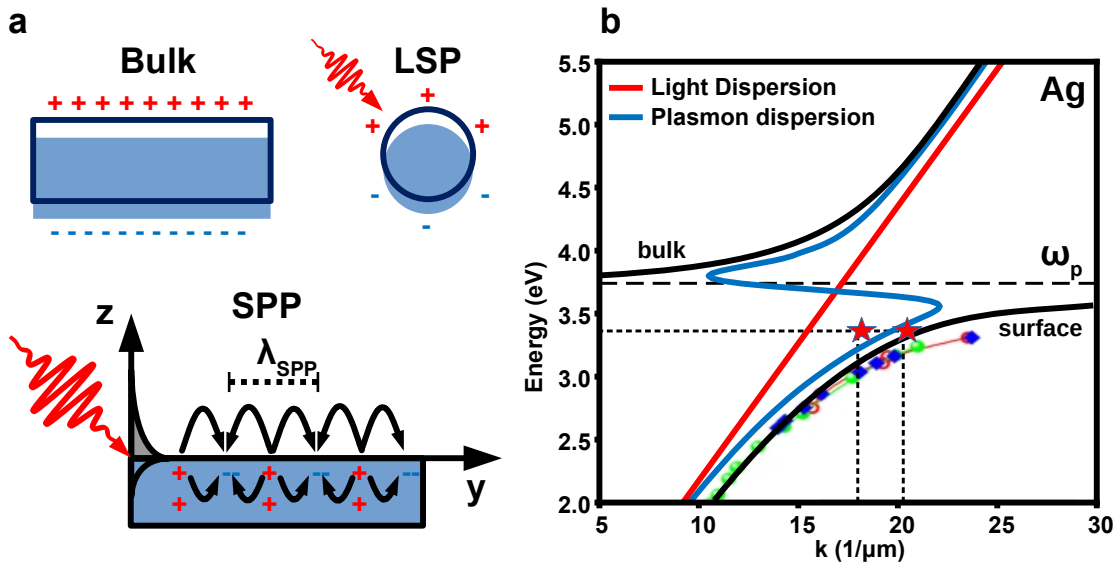


Figure 3.1: (a) Schematic representation of a bulk plasmon oscillation as well as the excitation of LSPs and SPPs by a short laser pulse. (b) Plasmon dispersion relation of Ag. The blue solid line marks the theoretical dispersion derived from the dielectric function from the reference [118], the red solid line is the light line and the black solid lines mark the SPP and bulk dispersion branches. The dots and stars mark experimental data from the reference [119] and results from our plasmonic dichroism PEEM measurements, respectively.

distinguishing propagating SPPs and ordinary diffraction phenomena, prescribing a distinctly different wavelength of an SPP as compared to that of the incident light [101]. Following the dispersion relation as depicted in Figure 3.1(b), the wavelength of SPPs differs significantly from the free-space radiation when their energy is close to the plasma frequency ω_p . For silver, this plasma frequency is located at around 3.8 eV due to interband transitions contributing to the screening response [115–117]. This energy is very convenient, since standard frequency-doubled Ti-sapphire lasers can easily provide it.

Combining the excitation of plasmons with magnetic materials, hence studying the interplay of the excited electron and spin system, is often referred to as magnetoplasmonics [120]. Ordinarily, this is realized in a heterostructure, for example by using typical plasmonic noble metals to create plasmons, which then interact with magnetic metastructures, films or alloys [121–124]. In the last 20 years, the remarkable progress in nanofabrication on the one hand and magneto-optical methods on the other have made this field more and more accessible by a variety of excitation and observation techniques [120, 125]. Despite the heterostructure approach, there is another, more literal approach to magnetoplasmonics. By trying to directly excite and utilize plasmons in a magnetic material, a coupling and deterministic control of the electron and the spin systems via plasmonic or magnetic excitation seems very promising. Contrarily to silver or gold, the optical properties of most commonly

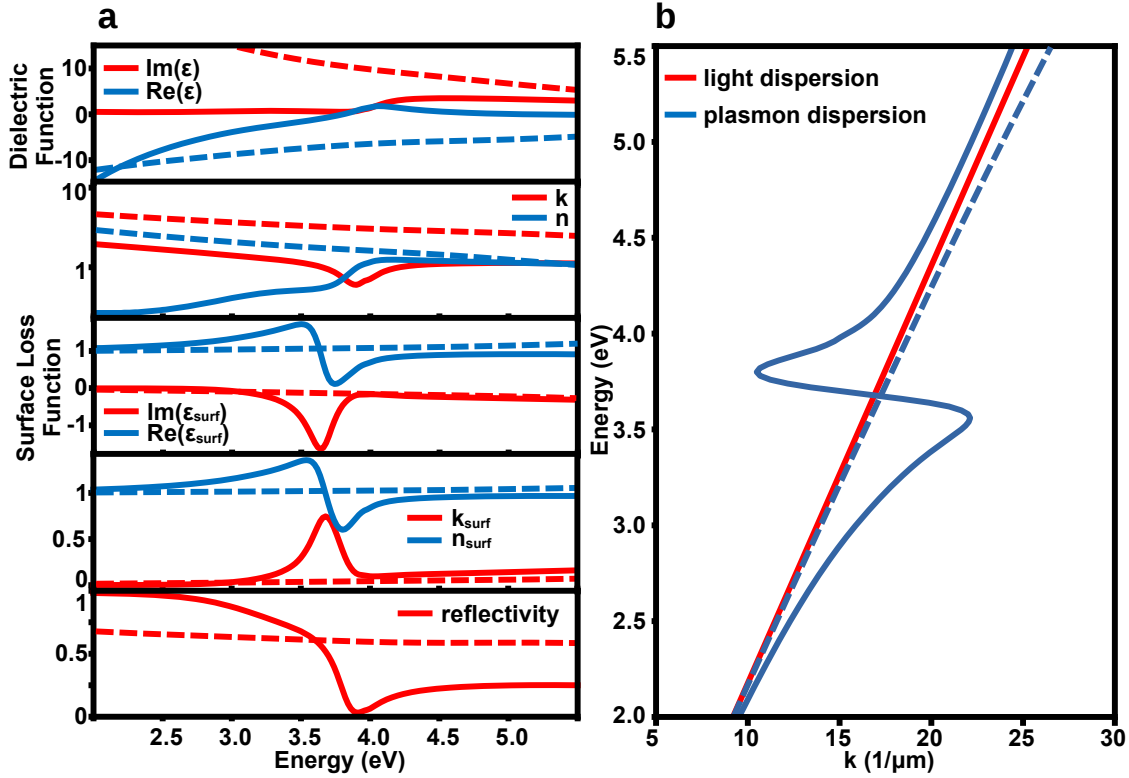


Figure 3.2: (a) Overview of the optical properties of the bulk and surface derived from the bulk dielectric functions of Ag (solid line, derived from the reference [118]) and Ni₈₀Fe₂₀ (dashed line, derived from the reference [126]). (b) Comparison of the light and plasmon dispersion relation in Ag (solid line) and Ni₈₀Fe₂₀ (dashed line) as derived from the respective data in (a).

used ferromagnetic materials are not ideal, causing strong damping. Hence, the amplitude of an SPP is expected to decrease exponentially within a few micrometers in Ni. A second conceptual challenge for the investigation of SPPs on transition metal surfaces comes from their dispersion relation. Figure 3.2 shows a comparison of optical properties derived from the dielectric functions of Ag [118] and Ni₈₀Fe₂₀ [126]. Most ferromagnetic transition metals exhibit a plasma frequency above 6 eV, which is higher than the photon energy available with laboratory light sources in most optical experiments [127, 128]. The corresponding differences between the wavelength of the incident photon and the SPP wavelength are generally below the spatial resolution limit of conventional optical microscopy experiments.

Experimentally, it is a challenging task to distinguish a plasmon from a common light wave with similar energy and momentum propagating in the metal [112]. This problem is often circumvented in the community by focusing on local excitations such as LSPs, which create a strong experimental response via a drastically enhanced photoelectron yield, or nonlocal effects via dipolar fields, which are easily detectable even in low-resolution conditions. The increase of the photoelectron yield in the

vicinity of patterned structures or defects is widely considered as the smoking gun for plasmonic field enhancement and therefore the detection of LSPs, and it is extensively investigated for standard plasmonic materials [103, 104, 107, 108] and ferromagnetic metals [122, 123, 129]. The existence of LSPs, however, implies also the existence of propagating SPPs in these materials, since both rely on the same light-matter interaction governed by the dielectric properties of the materials involved.

In this spirit, another approach is to coherently launch SPPs with the aid of an array referred to as magnetoplasmonic crystal, resulting in a plasmonic standing wave pattern and a resonant enhancement of the magneto-optical activity [130, 131]. Following this ansatz in photoemission electron microscopy (PEEM) experiments, SPPs at magnetic microstructures were imaged directly with nanometer spatial resolution by Rollinger *et al.* using variable incident light polarization and photon energy [59, 131].

In the following, we build upon these developments and demonstrate a more straightforward approach to excite and investigate propagating SPPs launched at magnetic microstructures, utilizing circular dichroism (CD) imaging in PEEM. Simultaneously, we use the evanescent character of propagating SPPs to circumvent the aforementioned problem of distinguishing SPPs from ordinary diffraction. Therefore, we differentiate the bound surface state from free-space radiation often present in PEEM measurements [52, 54, 55, 132, 133] by means of the so-called plasmonic spin-Hall effect. Framing this as a *spin-Hall effect* might not be ideal since it suggests a *spin*-selective excitation of the electron system of the material, i.e. a spin-orbit related phenomenon. It rather describes a *helicity*-dependent excitation of SPPs according to the topography of the coupling structure. The evanescent electric field creates an additional spin angular momentum (SAM) perpendicular to the propagation direction of the SPP [134–136], which can be experimentally utilized via a selective excitation of SPPs at different edges of a microstructure [137, 138]. This experimental characteristic is related to the plasmonic spin-Hall effect. The effect is absent in a plane (diffracted) wave propagating in the bulk, since it relies on the presence of an additional perpendicular SAM to which the longitudinal SAM of the incident light can couple [135]. The coupling was already discovered in PEEM experiments on patterned silver samples [139]. In the following, we show that the plasmonic spin-Hall effect is also present in Ni₈₀Fe₂₀ microstructures, known as permalloy, and that it can serve as a tool to directly image and characterize propagating SPPs at magnetic surfaces via CD PEEM [140]. Thereby, this work marks a significant extension of the existing plasmonics of noble metals.

We show that the plasmonic spin-Hall effect gives rise to CD in threshold laser PEEM. We facilitate this observation to identify propagating SPPs on Ni₈₀Fe₂₀ for the first time and extract their wavelength and propagation length, providing valuable insights into the dielectric properties of the surface. Furthermore, we coin this phenomenon *plasmonic dichroism*.

The term avoids the reference to a spin-Hall type effect, due to the implicit confusions mentioned above, and it also fits the general definition of dichroic effects observed in PEEM experiments as explained in Section 2.2. To be precise, we consider this to be a plasmonic dichroism signal in the context of SPPs, since the term is already used to describe helicity dependent excitation of plasmonic colloid materials [141–143]. In addition, it was used to describe the same effect for LSPs and patterned metamaterials, suggesting the applicability of the term for SPP excitation [94].

3.2 Theory

The theoretical description for the existence and properties of plasmons is extensively covered in literature, and the interested reader may turn to the instructive publications by Maier *et al.*, Maradudin *et al.* and Zayats *et al.* [101, 144, 145]. Here, we summarize the most important derivations with a focus on SSP dynamics.

Due to the free electron-like nature of conduction band electrons in a metal, their collective behavior and the resulting optical properties can be described in a plasma picture. This model results in the complex dielectric function of the electron gas $\epsilon(\omega)$:

$$\epsilon(\omega) = 1 - \frac{\omega_p^2}{\omega^2 + i\omega\gamma} = \left(1 - \frac{\omega_p^2}{\omega^2 + \gamma^2}\right) + i \left(\frac{\omega_p^2\gamma}{\omega^3 + \omega\gamma^2}\right) . \quad (3.1)$$

Here, ω is the frequency of the driving field and γ is the collision frequency, i.e. the frequency damping of the moving electrons, sometimes described as $\gamma = \frac{1}{\tau}$, with τ being the relaxation time of the electron gas. Most importantly, ω_p is the bulk plasma frequency, i.e. the eigenfrequency of the electron bath, described by:

$$\omega_p^2 = \frac{Ne^2}{m_e\epsilon_0} . \quad (3.2)$$

Here, N is the electron density, e is the electron charge, m_e is the effective electron mass and ϵ_0 is the vacuum permittivity. The latter is derived from kinetic gas theory, i.e. unbound electrons moving through a lattice of relatively immobile ions, famously referred to as the Drude model [146]. Hence, the plasma frequency depends on the electron band structure and density of states. The optical properties of a material are

therefore inscribed in the dielectric function ϵ , which is a complex number:

$$\epsilon = \epsilon_1 + i\epsilon_2 = (n + ik)^2 \quad (3.3)$$

where ϵ_1 and ϵ_2 refer to the real and imaginary part of the bulk dielectric function, respectively. These can be translated into the more common values n and k , i.e. the refractive index and the extinction coefficient. We now consider our experimental case of a femtosecond laser pulse propagating in vacuum, i.e. a non-absorbing dielectric, and impinging on a conducting metal surface under an angle θ . The propagation through the metal-dielectric interface is described by the Maxwell equations, and the continuity condition results in a solution for an evanescent, electromagnetic wave propagating at the interface, where the amplitude decreases exponentially in the direction perpendicular to said interface. This evanescent wave is the aforementioned SPP, which follows a specific dispersion relation for $\omega < \omega_p$:

$$k_{\text{SPP}} = \frac{\omega}{c} \sqrt{\frac{\epsilon}{1 + \epsilon}} = k_0 \sqrt{\epsilon_{\text{surf}}} \quad , \quad (3.4)$$

where k_0 is the wave vector of the incident light in vacuum, i.e. the intersection point of the light line at a given photon energy, and ϵ_{surf} the dielectric function of the surface. Since we are only concerned with the dielectric properties at the surface of our material, i.e. the interface between a metal ϵ_m and the dielectric vacuum ϵ_d , we set $\epsilon_d = 1$ and $\epsilon_m = \epsilon$. All optical properties for the two materials of interest, Ag and Ni₈₀Fe₂₀, are shown in Figure 3.2.

A phenomenological comparison between an ordinary cp wave and a cp SPP is depicted in Figure 3.3. In panel (a), respective cross sections are marked by dashed boxes, which are schematically enhanced in panel (b) and (c). For the plane wave propagating in direction of k_L , the circular polarization introduces an SAM s_L parallel to k_L . The same is true for the evanescent wave in (c), but s_L decreases with increase in z . When integrating over z , as schematically illustrated by the blue-shaded areas, an uncompensated perpendicular SAM remains. This means that the evanescence in z is the inherent origin of the additional, perpendicular SAM of the SPP [134–136].

From the dispersion relation in Figure 3.2(b), it is clear that the additional momentum must have a certain origin. In other words, it is required to overcome the parallel momentum mismatch at a specific energy to optically excite the SPP. In the simplest case, this additional momentum is provided by a notch or an edge on the sample [109]. At such a discontinuity, the SPP is launched by an ultrashort laser pulse and travels along the metal-dielectric interface. In most experiments, the light angle of incidence θ with respect to the surface normal is not 0° , hence, the pump laser

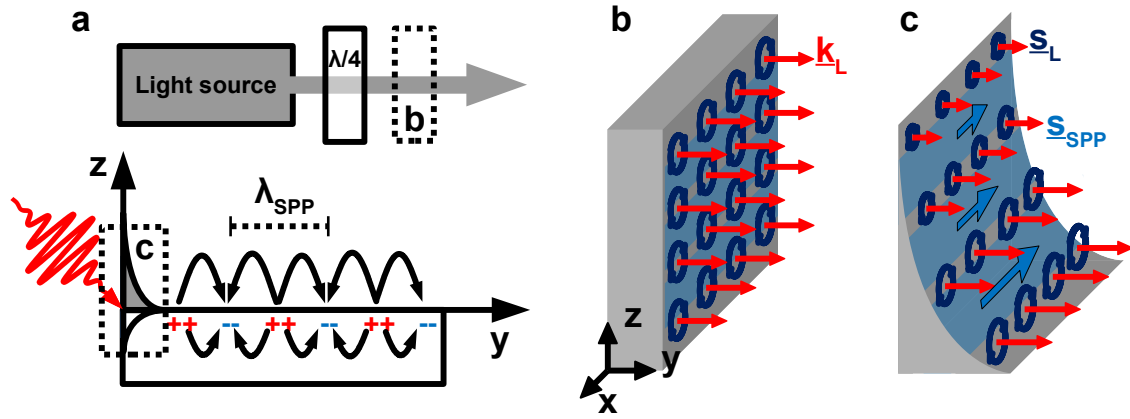


Figure 3.3: (a) Schematic difference between a cp planar wave in free space (top) and an SPP (bottom). The dashed boxes mark the cuts through the wave front discussed in panel (b) and (c). (b) Schematic cut through a light wave front propagating in direction of k_L with circular polarization, i.e. parallel angular momentum s_L . (c) Similar schematic for an evanescent, cp wave, revealing the perpendicular angular momentum s_{SPP} when integrating over the blue-shaded area due to the field gradient in z direction [140].

pulse interferes with the SPP launched, giving rise to a plasmonically enhanced and oscillating two-photon photoemission yield in PEEM [109]. This plasmonic moiré pattern observed in PEEM depends significantly on the polarization of the exciting laser pulse. In general, the direction of the pattern is always parallel to the edge of the structure where the SPP is launched. This edge is determined by the polarization, since an SPP is only launched when there is a component of the electronic field vector perpendicular to the coupling edge direction [137, 147].

An analysis of the moiré patterns can therefore provide an estimation for the dielectric function of the surface. The wavelength λ_M and the exponential decay of the interference pattern can be used to estimate the SPPs wavelength λ_{SPP} and its propagation length L_{SPP} [101, 147, 148]. The SPP wavelength can be extracted from the equation

$$\lambda_M = \frac{\lambda_{L,||} \lambda_{SPP}}{\sqrt{\lambda_{L,||}^2 + \lambda_{SPP}^2 - 2\lambda_{L,||} \lambda_{SPP} \cdot \cos \phi}}, \quad (3.5)$$

where $\lambda_{L,||} = \frac{\lambda_L}{\sin \theta}$ is the wavelength component of the incident laser light parallel to the surface. Here, we want to emphasize that the propagation direction of the SPP is given by k_{SPP} and is not necessarily collinear to the direction of the moiré pattern k_M . Thereby, ϕ in equation 3.5 is introduced as the angle spanned by the vectors k_L and k_{SPP} . It is therefore similar to a refraction angle and can be derived experimentally from the angle between the edge of the microstructure and the onset of the interference pattern observed in PEEM. These wave vectors, the general experimental configuration, and the respective angles are depicted in Figure 3.6 and

in the inset of Figure 3.7(f), where ϕ is marked by the dotted line. In other words, the SPP is an evanescent electromagnetic wave refracted at the coupling edge. Hence, ϕ can alternatively be calculated by Snell's law according to

$$\phi = \sigma_1 - \sigma_2 = \sigma_1 - \arcsin\left(\frac{1}{n_{\text{surf}}}\sin\sigma_1\right) . \quad (3.6)$$

Here, σ_1 is the angle between the in-plane projection of k_L and the normal vector of the edge where the SPP is launched and σ_2 describes the angle between the edge normal and the direction of k_{SPP} . The refractive index of the metal surface n_{surf} is defined by

$$n_{\text{surf}} = \text{Re}\left(\sqrt{\frac{\epsilon_{\text{bulk}}}{1 + \epsilon_{\text{bulk}}}}\right) \quad (3.7)$$

according to equation 3.3 and 3.4. Therefore, λ_{SPP} can be calculated from the observed moiré pattern according to the experimental parameters. Furthermore, λ_{SPP} is fully determined by the complex dielectric function. Equation 3.5 results in a quadratic equation:

$$\lambda_{\text{SPP}}^2 \left(\lambda_M^2 - \lambda_{L,\parallel}^2 \right) + \lambda_{\text{SPP}} \left(-2\lambda_{L,\parallel} \lambda_M^2 \cos\phi \right) + \lambda_M^2 \lambda_{L,\parallel}^2 = 0 . \quad (3.8)$$

Finally, the propagation length, i.e. the length where the intensity is decreased to $1/e$, can be derived from the decay length of the interference pattern L_M by

$$L_{\text{SPP}} = \frac{L_M}{\sin\phi} = \frac{1}{k_0} \left(\frac{1 + \text{Re}(\epsilon)}{\text{Re}(\epsilon)} \right)^{3/2} \frac{(\text{Re}(\epsilon))^2}{\text{Im}(\epsilon)} . \quad (3.9)$$

For the extreme case $\theta = 0^\circ$, i.e. normal incidence, $k_{L,\parallel} = 0$ and $k_M = k_{\text{SPP}}$, hence the observed pattern is of very short wavelength and gives a direct measure of the SPP wave vector [149]. This simplifies the interpretation of the data, but increases experimental complexity.

In conclusion, literature values of the bulk dielectric function of the metal of interest can be used to calculate the properties of the SPP and the expected moiré patterns observable in PEEM. Vice versa, PEEM measurements of these SPP patterns can give a good quantitative estimation for the respective dielectric function.

The derivations included here are only valid within the simple Drude picture. Although it is surprisingly accurate regarding its simplicity, it completely omits the quantum theory of solids. For example, it cannot explain the low plasma frequency of gold and silver. For this, one needs to account for the fully relativistic band structure and the respective interband transitions within these materials. Hence, it might be useful to expand upon the results and discussions presented in the following by

taking into account more advanced models and band structure effects.

3.3 Experimental details

Microstructures of metallic $\text{Ni}_{80}\text{Fe}_{20}$ supported on undoped GaAs(001) substrates were fabricated using electron beam lithography, thermal evaporation and lift-off by Niklas Liebing and Liane Brandt in the group of Prof. Georg Woltersdorf. For this, undoped GaAs(001) crystals were cleaned in ultrasonic baths of acetone and isopropanol with final processing in an ozone cleaner. For the e-beam writing process, 150 nm of PMMA positive e-beam resist (Allresist AR-P 641.09 200 K) was spin-coated and several arrays of squares and rectangles with 1 to 20 μm side length were written at $160 \mu\text{C}/\text{cm}^2$. Afterwards, the resist was developed for 10 seconds in a one-to-one mixture of methyl isobutyl ketone and isopropanol. The polycrystalline $\text{Ni}_{80}\text{Fe}_{20}$ structures were grown by thermal evaporation from $\text{Ni}_{80}\text{Fe}_{20}$ granulate material in a Al_2O_3 crucible at a growth rate of 0.064 nm/s, resulting in a height of about 30 nm after 8 min. Base pressure during evaporation was 1.3×10^{-6} mbar and the substrate was kept at room temperature. Finally, the morphology was checked *ex situ* via atomic force microscopy (AFM). The magnetic domain pattern was examined *in situ* via MOKE microscopy and *ex situ* via magnetic-force microscopy (MFM).

The laser setup explained in Section 2.1.2 is used as the light source for PEEM measurements. Here, frequency-doubling of the NOPA output is used for photon energies of 3.32 and 4.51 eV with pulse lengths of approximately 40 fs. The latter photon energy results in a dominant 1PPE process generating a high photoelectron yield at the microstructures as compared to the substrate, which is shown in Figure 3.7(d). Photoexcitation at 3.32 eV causes an inverted PEEM contrast between the $\text{Ni}_{80}\text{Fe}_{20}$ structure and the GaAs substrate, as shown in Figure 3.10(a). This is due to the dominant excitation of electrons from the valence band of GaAs via a 2PPE process. Figure 3.4 shows the verification of the 2PPE and 1PPE processes by variation of the pump power, revealing a non-linear and a linear increase of the average photoelectron yield, respectively. The measured 1PPE threshold lies at 4.5 eV, which is below the known work function of clean $\text{Ni}_{80}\text{Fe}_{20}$ of 5.0 eV [150, 151]. This is probably a result of residual gas adsorption after growth and during sample transfer. Counterintuitively, the use of undoped GaAs substrate does not cause any charging effects during PEEM measurements. This is either also an effect of adsorbates forming a conductive layer directly at the surface, or, more likely, the result of using high intensity laser pulses causing laser-induced photoconductivity [152, 153].

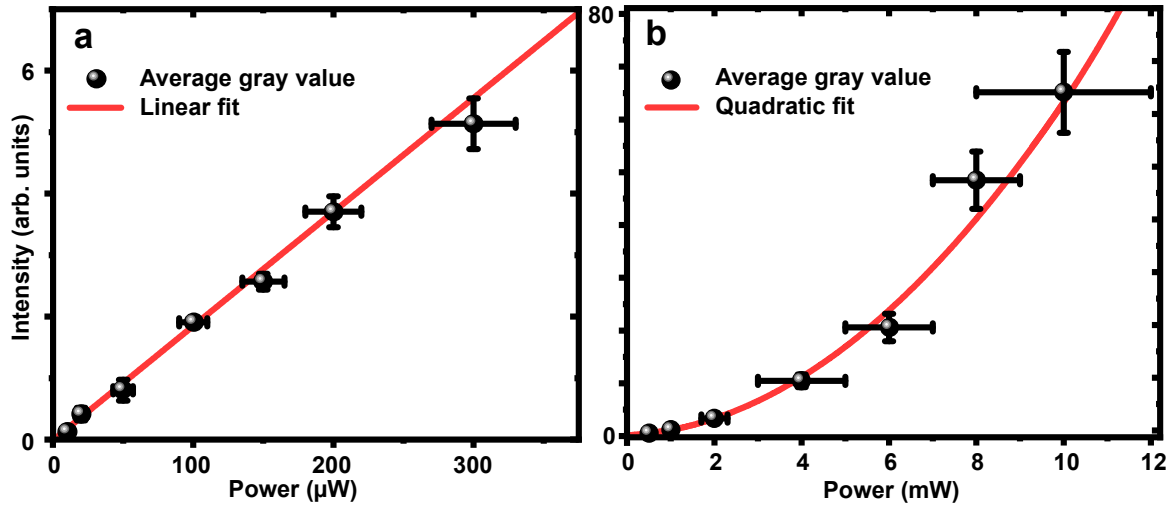


Figure 3.4: Averaged photoelectron yield of PEEM measurements of $\text{Ni}_{80}\text{Fe}_{20}$ microstructures on GaAs versus laser power. Photon energy is 4.51 eV in (a) and 3.32 eV in (b), respectively, revealing a linear and a quadratic scaling behavior characteristic for 1PPE and 2PPE processes.

3.4 Results & Discussion

Since silver is a benchmark system for imaging SPPs in PEEM, we performed an initial test for our experimental setup using silver-coated, microstructured Si samples. The pattern consists of an array of squares with an edge length of $8\ \mu\text{m}$ separated by a gap of $2\ \mu\text{m}$. First, we compare measurements of a silver film on a structured Si(100) substrate with literature values for SPPs derived from bulk or thin films. The PEEM images shown in Figure 3.5(a) for p -polarized light and 3.5(b) for circular polarized light show an oscillating intensity at the edges. We stress that this sample was not made for plasmonic purposes, hence its quality in terms of intensity and coherence of the plasmonic signal is not ideal. Nevertheless, by analyzing the cross section of the oscillations parallel to the edge and averaging over several structures, we obtain a good estimate for the plasmonic and dielectric properties of the Ag surface. Fitting an exponentially damped sine function to the cross section line profile of the observed interference pattern provides an estimate for the SPP propagation length L_{SPP} according to equation 3.9. At a photon energy of 3.32 eV, we find an experimental propagation length of $L_{\text{SPP,Ag}} = (1.2 \pm 0.3)\ \mu\text{m}$, which is in perfect agreement with the expected theoretical value of $L_{\text{SPP,Ag}} \approx 1.21\ \mu\text{m}$ based on known optical constants of Ag thin films [118].

Additionally, we can calculate k_{SPP} from fitting λ_{SPP} according to equation 3.5, which matches the dispersion relation nicely as shown by the two red stars in Figure 3.1(b). Interestingly, we observe a difference in k_{SPP} between s - and p -polarized light. This is an effect typical for arrayed structures exciting the SPP [145]. For s -polarized light, the edges launching the plasmon, i.e. the horizontal edges in Figure

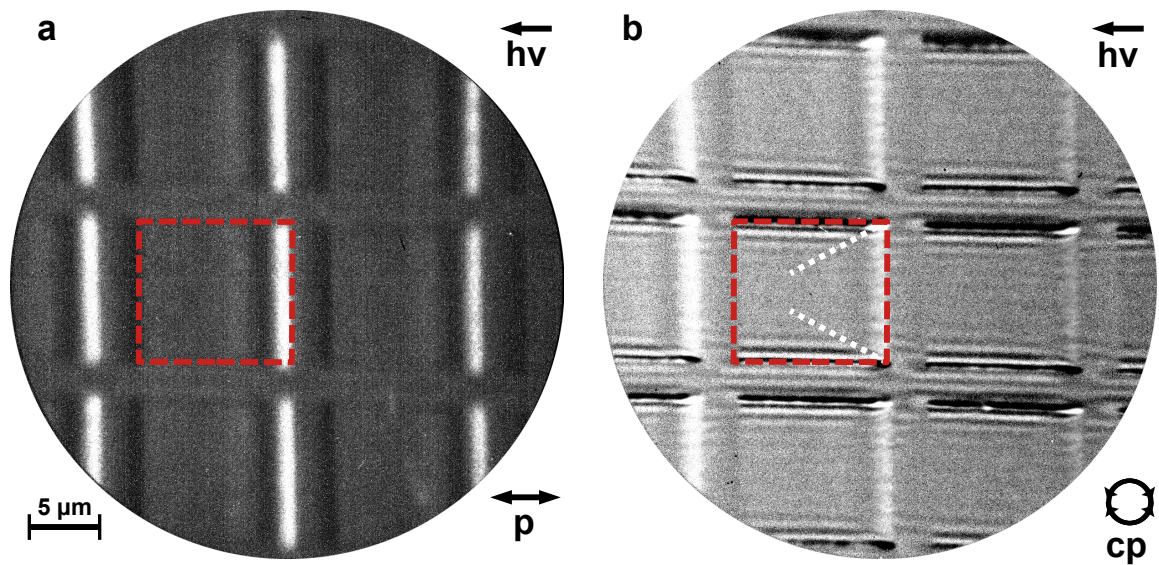


Figure 3.5: (a) PEEM image of an array of Ag squares using p -polarized laser pulses at 3.32 eV (30 fs, 1.23 MHz, 1 mW). The dimensions of the structure are marked by a red-dashed square. (b) CD PEEM image of the same area as in (a), showing fringe fields at the edges parallel to the excitation direction marked in the top-right corner. The white-dashed lines mark the onset of the observed moiré pattern.

3.5, are much closer together and the corresponding SPPs interfere with each other. Contrary, for p -polarized light, the plasmon is clearly damped within the length of the Ag-square, starting from the vertical edges facing the direction of the incoming light.

The excitation geometry is schematically depicted in Figure 3.6(a). The laser pulse excites the microstructure under an angle of incidence θ with respect to the surface normal. At the edge, an SPP is launched, which propagates in a direction (y direction) defined by the phase matching based on the surface refractive index. Interference of the incoming laser plane wave with the propagating plasmon field results in a modulation of the PEEM intensity parallel to the edge, i.e. a moiré pattern, as detected in the experiment (gray lines). The plasmon propagation direction gives rise to a shadowing area of the interference pattern starting at the corner of the microstructure (black dotted line parallel to the y direction).

Switching between lcp and rcp excitation utilizes a selective excitation of SPPs at different edges of a microstructure [137, 138], which causes the aforementioned plasmonic dichroism present in Figure 3.5(b). Furthermore, the use of an asymmetry measurement technique is to experimentally distinguish a plasmonic excitation from other contrast mechanisms in PEEM. The plasmonic spin-Hall effect causes lcp light to predominantly excite photoelectrons on the left edge of the structure in PEEM, whilst rcp enhances photoemission from the right edge, as shown in Figure 3.6(b)

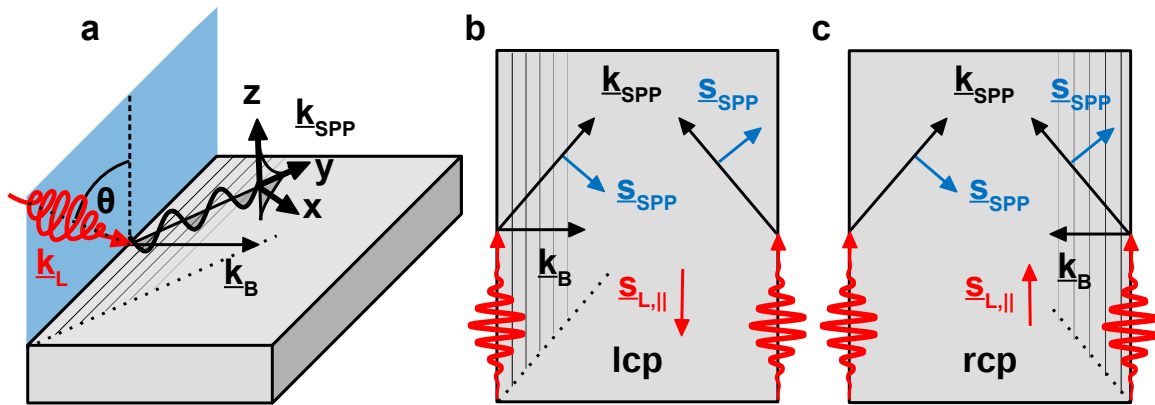


Figure 3.6: (a) Schematics of SPP excitation by a *cp* laser pulse at the edge of a $\text{Ni}_{80}\text{Fe}_{20}$ microstructure. Details are provided in the text. (b) Schematics of the plasmonic spin-Hall effect, where the SAM of the incoming *cp* light couples to the parallel component of the SAM of the SPP, causing an enhanced excitation on the left edge for *lcp* photoexcitation. (c) Opposite case of *rcp* light, where the SPP is excited on the right edge [140].

and (c). Hence, this plasmonic spin-Hall helicity dependence results in a dichroic (plasmonic) interference pattern in the PEEM image, which we facilitate in our CD PEEM approach. In these asymmetry images, the phase of the oscillation depends on the direction of the edge. Consequently, calculating the asymmetry according to equation 2.10 results in a phase shift of π in the subsequent asymmetry PEEM image when comparing the interference patterns at opposite edges.

The good results obtained for Ag corroborates our approach and motivates the investigation of more complex, ferromagnetic materials, namely $\text{Ni}_{80}\text{Fe}_{20}$ microstructures. Figure 3.7(a) shows a MOKE image measured by Liane Brandt with an array of $\text{Ni}_{80}\text{Fe}_{20}$ squares and rectangles, where the magnetic contrast reveals the expected Landau domain pattern [154]. In panel (b) and (c), the surface morphology as well as the shape of the domain pattern is verified via AFM and MFM, respectively. The AFM image demonstrates the overall flatness of the $\text{Ni}_{80}\text{Fe}_{20}$ structures with an average thickness of 30 nm, low roughness and a small decrease of approximately 1 nm in height at the edges, probably originating from the lift-off process. However, this decline at the edge is only present in some of these structures, whereas others are of constant height (e.g. the ones in Figure 3.9). Figure 3.7(d) shows a laser-excited PEEM image of one rectangular $\text{Ni}_{80}\text{Fe}_{20}$ island for photoexcitation with *lcp* light at a photon energy of 4.51 eV. Here, the dominant mechanisms contributing to the PEEM contrast are the topography contrast as well as the work function contrast between substrate and metallic structure. The increased intensity close to the edge is the result of the aforementioned decrease in height apparent in AFM. The CD image derived according to equation 2.10 is depicted in panel (e), revealing an oscillatory

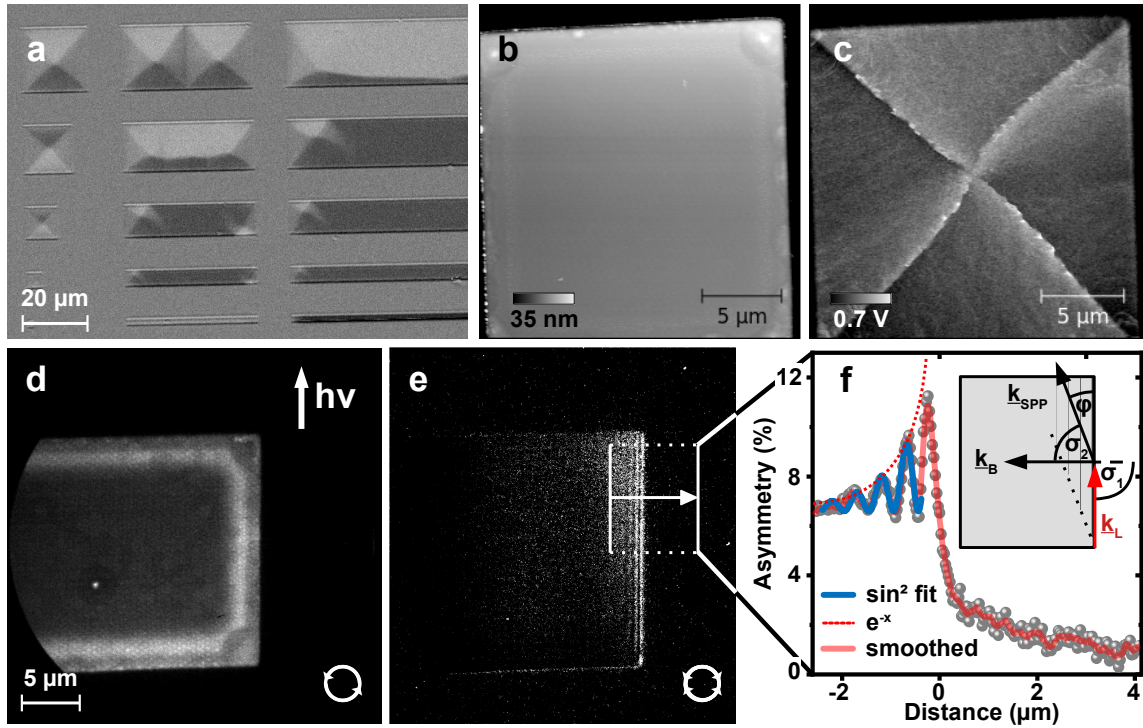


Figure 3.7: (a) MOKE image of $\text{Ni}_{80}\text{Fe}_{20}$ microstructures grown on GaAs(001). Magnetic domains of typical Landau patterns are visible. An AFM (b) and MFM (c) image of the square in the top-left corner in (a) displaying the height and magnetic domain walls, respectively. (d) Laser PEEM image of the rectangular $\text{Ni}_{80}\text{Fe}_{20}$ island in the middle column of (a) for lcp light at 4.51 eV, with the direction of light incidence marked in the upper right. (e) CD PEEM image of the same structure in (d) with the interference pattern at the right edge of the $\text{Ni}_{80}\text{Fe}_{20}$ microstructure. (f) Cross section of the region marked in (e) with an inset showing the wave vectors k_L and k_{SPP} [140].

signal in the vicinity of the right edge. The oscillation is pointed out more clearly in Figure 3.7(f), showing the cross section line profile over the box drawn in Figure 3.7(e). Here, several exponentially damped maxima are apparent which are fitted by a sine function. An inset illustrates the geometry and vectors for the upcoming discussion.

In both Figures 3.7(d) and (e), no magnetic contrast is visible. In theory, MCD for threshold PEEM should be present here (see Chapter 4), but the signal is either too small or absent due to surface contamination. Hence, MOKE and MFM image the effect of *bulk* domains, whereas MCD PEEM via oblique incidence is very surface sensitive (see Section 2.1.1).

According to equation 3.6, the experimentally observed angle of $\phi = 12^\circ \pm 5^\circ$ corresponds to a surface refractive index of $n_{\text{surf}} = 1.02 \pm 0.02$ for $\text{Ni}_{80}\text{Fe}_{20}$ at 3.32 eV. This value agrees well with the tabulated bulk value for $\text{Ni}_{80}\text{Fe}_{20}$ of $n_{\text{surf}} = 1.017$ according to equation 3.7 [126]. Again, fitting an exponentially damped sine function

to the intensity decay of the interference pattern as shown in Figure 3.7(f) gives a propagation length of $L_{\text{SPP},\text{Py}} = (3.4 \pm 1.0) \mu\text{m}$ for $\text{Ni}_{80}\text{Fe}_{20}$ at 3.32 eV when averaging over several structures. The large uncertainty results mainly from the relative error of ϕ . Due to the small refractive index, the angle ϕ is also small, hence the moiré pattern is only detected very close to the edge. We conclude that the experimentally obtained value for $L_{\text{SPP},\text{Py}}$ is in good agreement with the theoretical value of $L_{\text{SPP},\text{Py}} \approx 3.53 \mu\text{m}$ based on the bulk dielectric function of $\text{Ni}_{80}\text{Fe}_{20}$ [126].

We want to give some remarks regarding the gathered data so far. First, by using a laser pulse duration of 30-50 fs, the SPP propagation length is experimentally accessible without the need of a pump-probe delay up to $\approx 13 \mu\text{m}$, which is much longer than the $L_{\text{SPP},\text{Py}}$ observed here. Since the damping is too strong, pump-probe experiments would not be particularly beneficial for imaging the SPP propagation in this material compared to Ag [113]. Second, the exact position of the edge is not well defined in CD PEEM images. For calibration purposes, a standard PEEM image illuminated via the mercury discharge lamp is taken which defines the edge position. But, there are inevitable drifts connected to CD PEEM images during the long acquisition time of 20-60 min. Additionally, the yield at the edge depends on the excitation energy and direction. Close to the edge of microstructures, an asymmetry signal in CD PEEM images is generally observed. This signal can be of plasmonic [145] or refractive [54, 55] origin, or a superposition of both [155]. Figure 3.8 shows an example for this problem, which is present in all following plasmonic measurements. The cross sections (b) and (c) of the opposite edges, marked in the CD PEEM image in Figure 3.8(a), reveal an oscillation similar to the one observed in 3.7(e). Both datasets show an oscillation at opposite edges with an opposite sign, and the height of the first extremum in (b) and (c) is much bigger than the rest of the pattern. When comparing the second minimum in (b), the data are well reproduced by the smoothed line, which is not the case for the second maxima in (c). The background-corrected sine fits shown as blue-solid lines in Figure 3.8(b) and (c) corroborate this analysis. The inclusion of the data of the first extremum results in overestimation (b) and underestimation (c) of the pattern's wavelength. The increased extremum and deviation stem from a helicity-dependent refractive edge effect probably caused by switching the wave plate, which inevitably alters k_{L} slightly. To account for this, the first observed extremum is always masked when fitting the damped sine wave to the yield signal, which improves the quality of the fit and reduces error of the subsequent calculations.

Following the geometry considerations of Figure 3.6, one way to increase the length of the observed moiré pattern λ_{M} is to decrease the angle of incidence σ_2 , which results in an increased ϕ . For this, we used $\text{Ni}_{80}\text{Fe}_{20}$ structures which are grown tilted by $\pm 15^\circ$ with respect to the direction of the incident light. Figures 3.9(a) and

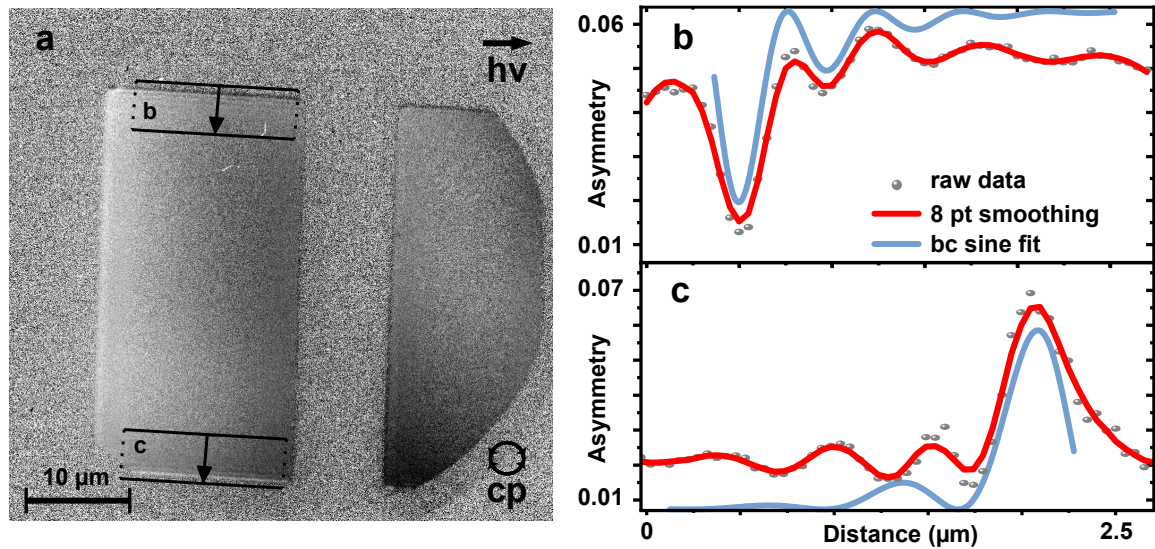


Figure 3.8: (a) CD PEEM image of a Ni₈₀Fe₂₀ rectangle on GaAs. (b) and (c) show line scans of the respective areas marked in (a), revealing an oscillatory change in the asymmetry signal close to the edge. This is retraced by smoothing (red) and fitting the data (blue), the latter resulting in an apparent shorter (b) and longer (c) wavelength when including the data of the first extremum.

(b) show CD PEEM images of these structures, which also inhibit the aforementioned refractive edge effect. Comparison of the dichroic interference patterns of opposite edges is shown by the marked cross sections in Figure 3.9(d). It reveals a longer wavelength λ_M , whilst the total asymmetry decreased. Additionally, the interference is visible only at the left edge for the Ni₈₀Fe₂₀ square rotated by -15° in Figure 3.9(a) and at the right edge for $+15^\circ$ in Figure 3.9(b). This phenomenon is explained by Snell's law, since $\sigma_1 > 90^\circ$ at the edges where no interference is observed. The cross section of the interference patterns on both Ni₈₀Fe₂₀ squares show a clear phase shift of π with an otherwise similar amplitude and damping. This phase shift is explained in the next section. Again, the superposition of refractive and plasmonic effects is apparent in the first extremum.

According to theory, the plasmonic spin-Hall effect is independent of the photon energy exciting the SPP [134–136]. Indeed, we find SAM-dependent excitation of SPPs also at 3.32 eV. Figure 3.10(a) shows a background-corrected PEEM image of a Ni₈₀Fe₂₀ square rotated by 45° with respect to k_L illuminated with *lcp* light. The drastically different contrasts compared to Figure 3.11(d) are evident. By changing the excitation energy from 4.51 eV to 3.32 eV, the PEEM contrast mechanism changes from the 1PPE to the 2PPE process, as shown in Figure 3.4. The 2PPE process allows us to excite SPPs and observe the resulting interference patterns on Ni₈₀Fe₂₀ as well as on the GaAs. Figure 3.10(b) shows a comparison of the cross sections marked

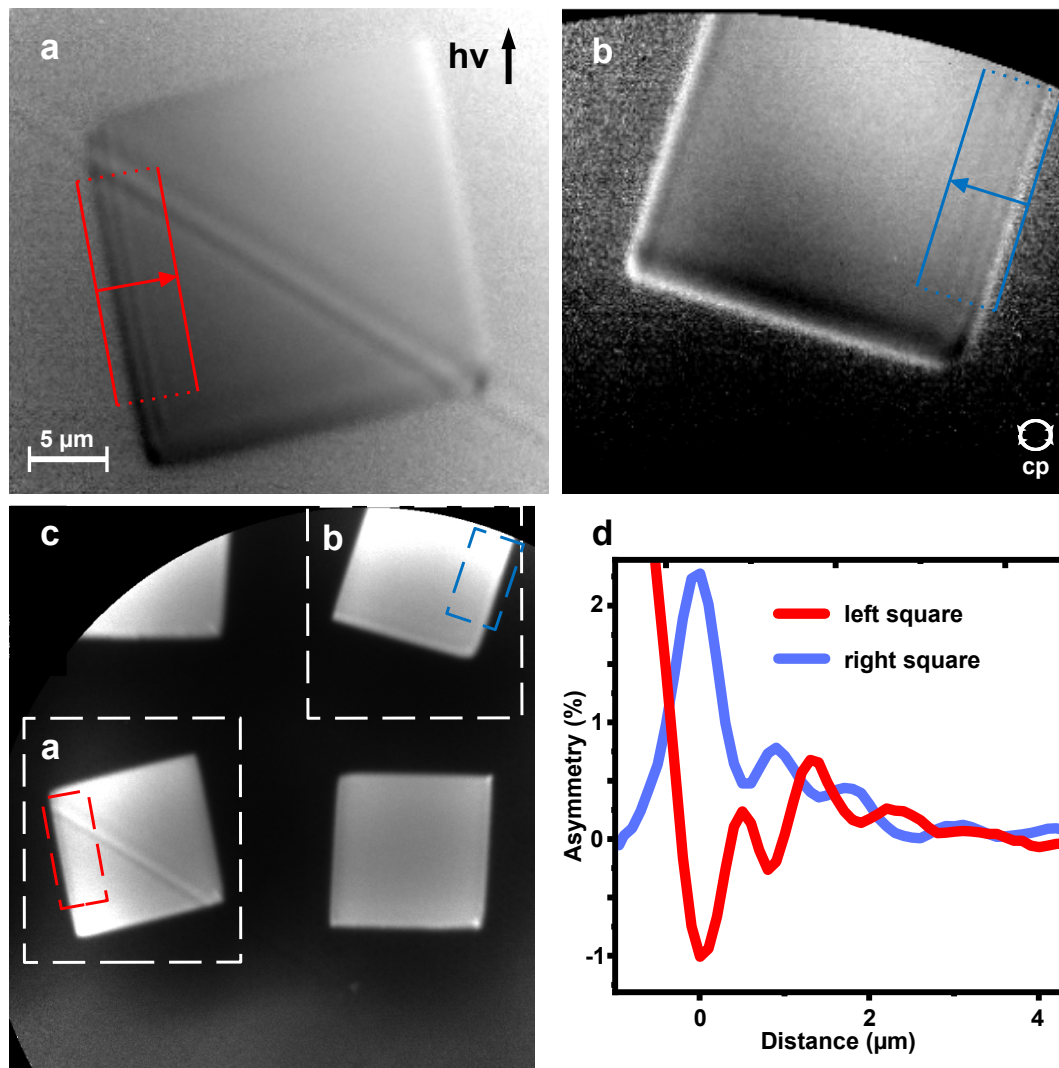


Figure 3.9: (a) & (b) CD PEEM images of $\text{Ni}_{80}\text{Fe}_{20}$ microstructures rotated by $\pm 15^\circ$ from the light incidence direction. Measured at the incident laser photon energy of 4.51 eV, the image shows clear edge-induced interference patterns. (c) Overview PEEM image containing the structures of panel (a) and (b), measured at a photon energy of 5.2 eV with a Hg discharge lamp. (d) Aligned cross section of the moiré patterns marked in (a) and (b), revealing their identical wavelength and a phase shift of π [140].

in (a), revealing a different asymmetry yield when comparing the upper and lower edge. Subtracting one from the other gives the black line, which leaves an oscillatory pattern similar to Figure 3.8 that clearly stems from the lower edge. Hence, the SAM vectors match the characteristics of the plasmonic spin-Hall effect depicted in Figure 3.6.

We now compare the specifics of the observed oscillation on $\text{Ni}_{80}\text{Fe}_{20}$ and GaAs in more detail in order to conclude on its origin, which can be either plasmonic or

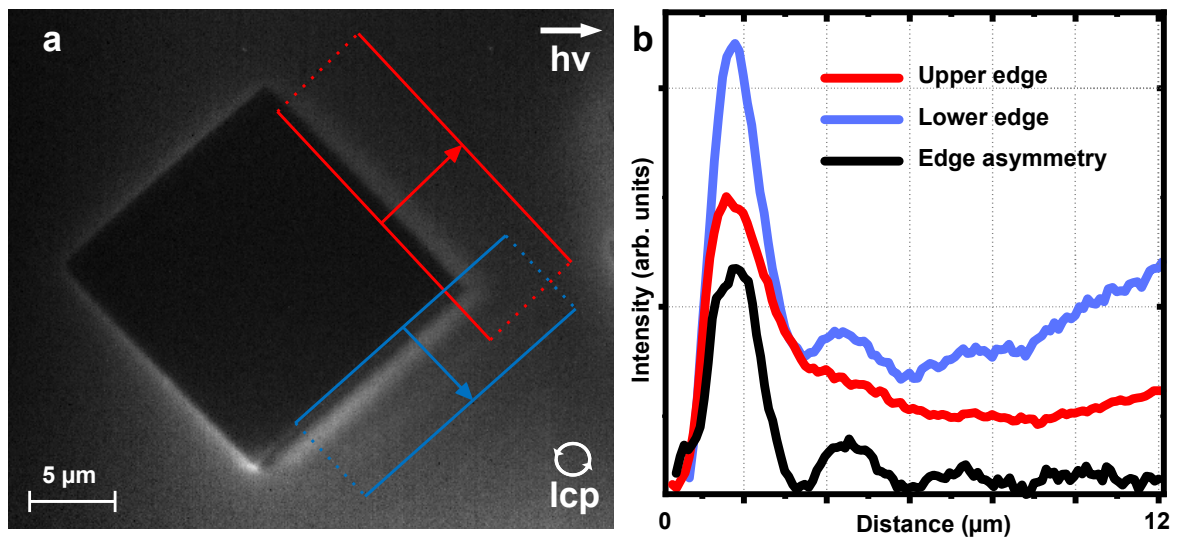


Figure 3.10: (a) PEEM image measured with laser photon energy of 3.21 eV with the direction of light incidence shown on the top-right. (b) Graph showing the cross section of the areas marked in (a) as well as an aligned asymmetry calculated from these, revealing an oscillatory change in the asymmetry signal with constant wavelength and damped amplitude.

diffractive. Figure 3.11(a) shows the CD PEEM image for 3.32 eV excitation on two rectangular $\text{Ni}_{80}\text{Fe}_{20}$ microstructures with the bare GaAs substrate surface in between, where a clear SPP interference pattern is observed. This geometry is the same as in Figure 3.7(e) but with a different excitation wavelength. Figure 3.11(b) shows the cross section from one $\text{Ni}_{80}\text{Fe}_{20}$ microstructure to the other across the GaAs gap. The raw data across the edge itself is shown in Figure 3.12(a), and Figure 3.12(b) shows the background-corrected data aligned to the first maximum. This dataset is accurately fitted by a damped sine function and not by a Bessel function, which hints at a plasmonic origin of the oscillation rather than a diffractive one. The asymmetry signal in Figure 3.11(b) reveals two exponentially damped sinusoidal waves of constant wavelength starting at each edge of the $\text{Ni}_{80}\text{Fe}_{20}$ microstructures. The superposition of both sinusoidal waves in the GaAs region results in an antisymmetric pattern with respect to the gap center as fitted by the solid red line. Note that this antisymmetry of the moiré pattern corresponds directly to the phase shift of π observed in Figure 3.9(d) and the edge selectivity in Figure 3.10, which manifests the plasmonic spin-Hall effect.

Furthermore, the interference pattern on GaAs has a higher amplitude and a longer wavelength than that on $\text{Ni}_{80}\text{Fe}_{20}$, as evident in Figure 3.12(c) by the different peaks in the 2D FFT data and in Figure 3.12(d) by directly comparing the two wavelengths of the moiré pattern. This can be attributed to their different surface refractive indices.

The strong signal in the gap region allows to directly show the origin of the

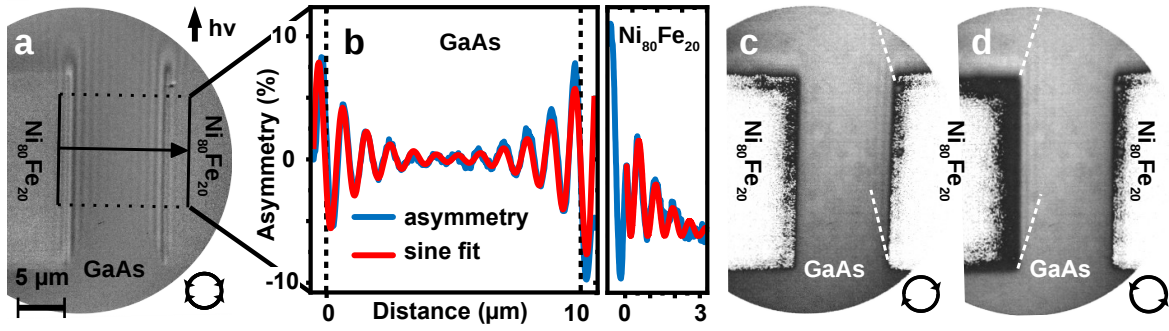


Figure 3.11: (a) CD PEEM image of two Ni₈₀Fe₂₀ microstructures and the GaAs substrate region in between measured with a photon energy of 3.32 eV. The direction of light incidence is marked in the upper right. (b) CD line scan of the marked gap area in (a) and fit by the superposition of two damped sinusoidal waves with constant wavelength (red). The positions of the edges are marked in (b) by vertical dashed lines. (c) & (d) PEEM images for *rcp* and *lcp* light after background subtraction, respectively [140].

dichroism by analyzing the raw PEEM images for each light polarization. Individual, background-corrected PEEM images for *rcp* and *lcp* light are depicted in Figure 3.11(c) and (d), respectively. As marked by the white dashed lines, Figure 3.11(c) shows the interference pattern and SPP excitation mainly at the right edge, whereas the SPP in Figure 3.11(d) is observed at the left edge. This edge-selective SPP excitation is characteristic for the plasmonic spin-Hall effect. Both images combined according to equation 2.10 constitute the CD image in Figure 3.11(a). Hence, the plasmonic spin-Hall effect explains the observed phase shift of π in the dichroic images.

To additionally support that the observed phase shift of π in CD PEEM is a result of the plasmonic spin-Hall effect, we compare images obtained with linearly and circularly polarized light. In the following, *linear dichroism* means switching between *s*- and *p*-polarized light. Figure 3.13(a) shows a CD PEEM image of the GaAs gap with cross sections of the marked areas in Figure 3.13(c). These line scans again reveal the aforementioned phase shift of π . Figure 3.13(b) shows a linear dichroic image of the same region and the corresponding line scans in Figure 3.13(d). In the latter, the same wavelength of the interference patterns as in Figure 3.13(a) is observed but without any significant phase shift. This observation is consistent with the theoretical considerations explained above as well as previous experiments on silver [139]. Due to the fact that *p*-polarized light has no wave vector component perpendicular to the edge of the structure, the interference in the linear dichroic signal originates dominantly from *s* polarization. Hence, a dichroic signal remains without a phase shift when comparing both edges by calculating the asymmetry according to equation 2.10 by replacing I_{lcp} and I_{rcp} with I_s and I_p , respectively. Additionally, it is beneficial to multiply the photoelectron yield of *s*-polarized light with a scaling factor to account for the different total yield for *s* and *p* polarization in

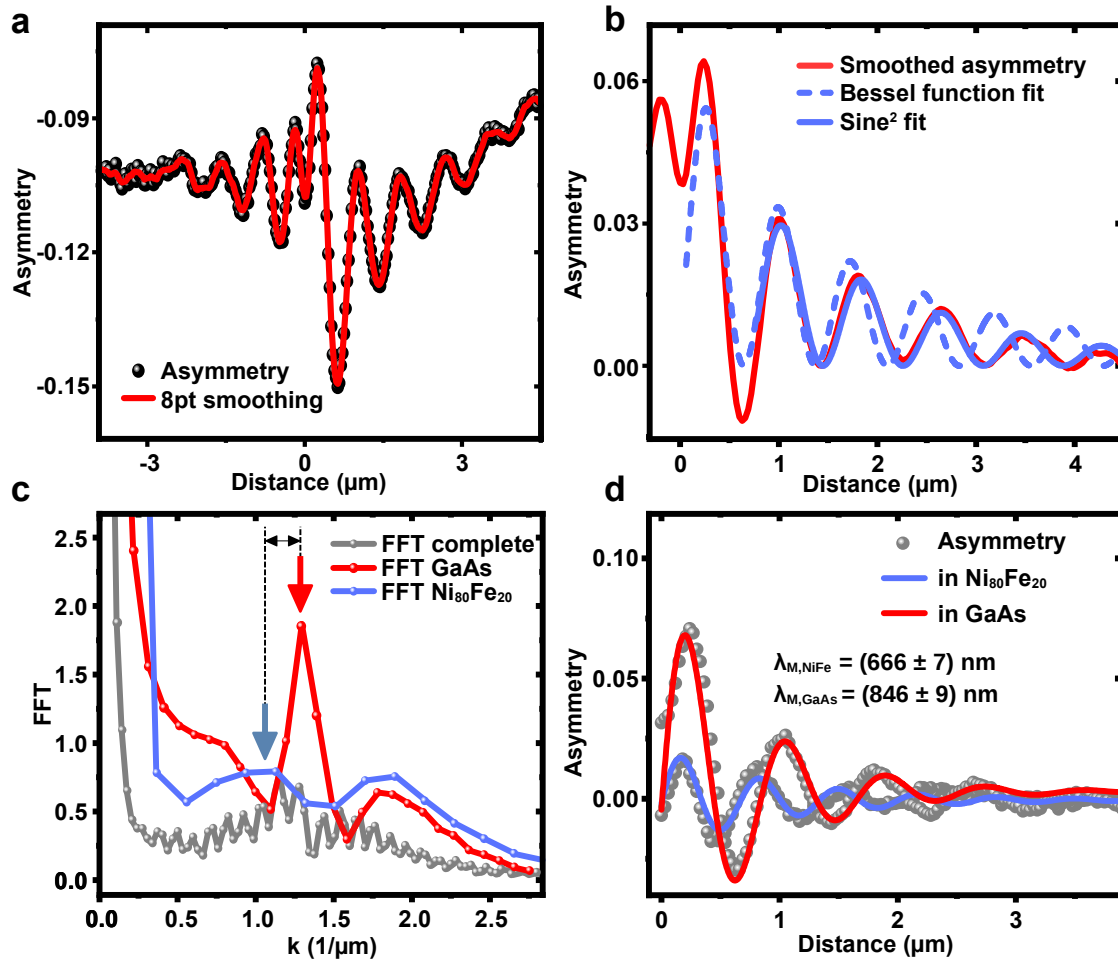


Figure 3.12: (a) Raw data of the line scan across the edge of the $\text{Ni}_{80}\text{Fe}_{20}$ structure of the CD PEEM image in Figure 3.11(a). (b) Background-subtracted data from (a) with fits for damped sinusoidal oscillations. The asymmetry oscillates with a constant wavelength, fitting an exponentially damped sine curve rather than a Bessel function. (c) 2D FFT analysis of the CD PEEM image shown in 3.11(a). Grey-, red- and blue-solid lines mark the FFT analysis of the whole image, of only the GaAs gap region and of only the $\text{Ni}_{80}\text{Fe}_{20}$ structure, respectively, revealing different wave numbers for both materials. (d) Aligned, background-subtracted cross-section data of (a) comparing the oscillation on GaAs and $\text{Ni}_{80}\text{Fe}_{20}$, revealing a different wavelength.

oblique incidence experiments due to the different electric field component of the laser light perpendicular to the surface $k_{L,\perp}$. This scaling factor is defined by the ratio of the average yields in the FoV of each polarization.

As a matter of fact, a phase shift of π should also be measurable for a non-collinear plasmonic excitation with s -polarized light at opposite perpendicular edges, due to the phase shift in the dipole excitation at the step edge [112]. However, this does not appear to be the case, neither in PEEM experiments in the literature [139, 147] nor in our experiments.

The puzzling result omitted so far is the observed moiré patterns on GaAs. These

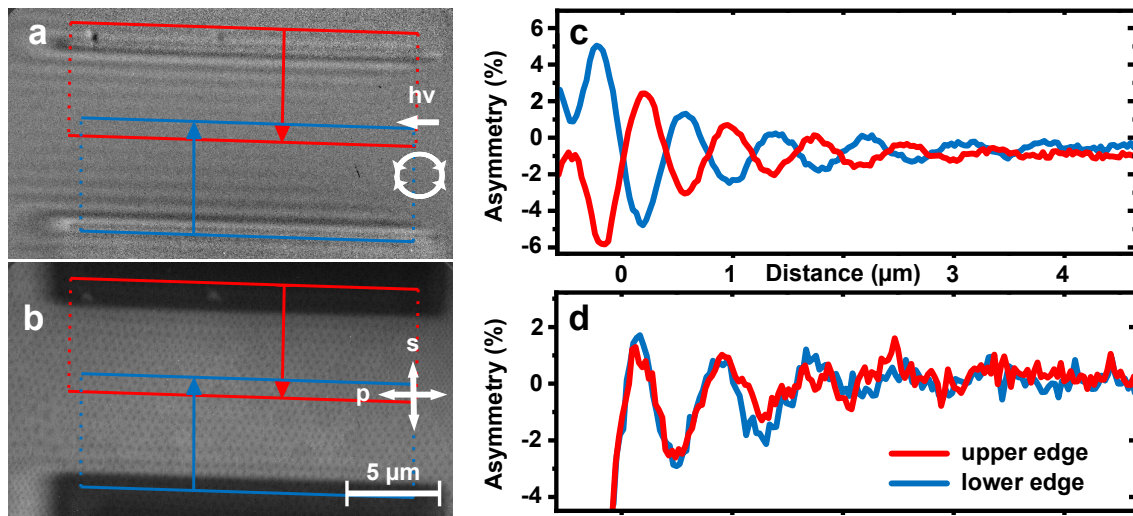


Figure 3.13: CD versus LD laser PEEM images of the region between two $\text{Ni}_{80}\text{Fe}_{20}$ microstructures measured at the incident photon energy of 3.32 eV in (a) and (b), respectively. The direction of light incidence is from right to left. Dichroic line scans are depicted in (c) and (d) starting from both edges for cp and lp light, respectively. For the CD in (c), a phase shift of π is observed when comparing the dichroic signals of the upper and lower edges. This phase shift is absent for LD in (d) [140].

are visible in all performed 2PPE measurements. There is also a clear energy and material dependence when comparing the oscillation on $\text{Ni}_{80}\text{Fe}_{20}$ and GaAs, as depicted in Figure 3.12. Since GaAs is a direct band gap semiconductor ($\text{Re}(\epsilon_{\text{surf}}) < 1$) [156, 157], excitation of SPPs in the GaAs ground state is not possible. Besides, there is a variety of dielectric properties available in literature due to the great influence of doping and impurities in this material. For undoped GaAs, the band gap of 1.44 eV at 300 K [158] is smaller than the excitation energy used in both 1PPE and 2PPE experiments. Thereby, it is well known that upon ultrafast excitation an electron-hole plasma is formed due to the high population of the conduction band within a short time frame (< 1 ps) [153, 159]. Within this transient state, a plasmonic excitation can occur, which typically couples to a longitudinal optical phonon mode [153, 160]. However, this phononic coupling is only probed in the frequency range of several THz [161], i.e. for excitation with infrared light, which means a phonon excitation can be excluded in our case. Nevertheless, the intensity in our experiments easily extends above $100 \mu\text{J}/\text{cm}^2$ for 2PPE excitation, which should create a transient quasi-metallic state. Similar observations were already debated in literature, but no real conclusion emerged [51, 155, 162]. If this is indeed a phenomenon based on photodoping, the resulting wavelength of the plasmonic oscillation, i.e. the observed moiré pattern, should be dependent on the population of the conduction band, i.e. on the pump pulse power. An upcoming experiment will therefore choose different pump power

and check for changes in the CD PEEM images. Another possibility is the excitation of an SPP at the $\text{Ni}_{80}\text{Fe}_{20}/\text{GaAs}$ interface, which then propagates through the GaAs substrate within the transient photodoped state and could cause such interference patterns, too. This can also be excluded, since the skin depth of 3.32 eV in $\text{Ni}_{80}\text{Fe}_{20}$ is of the order of 10 nm [126]. Hence, the intensity after 30 nm should not result in any significant contribution from the $\text{Ni}_{80}\text{Fe}_{20}/\text{GaAs}$ interface.

3.5 Conclusion

In this chapter, we analyzed the circular and linear dichroism in threshold PEEM images of $\text{Ni}_{80}\text{Fe}_{20}$ microstructures on GaAs. The observed interference patterns surrounding the edge of these structures reveal characteristics which exclude pure diffraction phenomena and are clearly described by the plasmonic spin-Hall effect. Detailed analysis of the experimentally acquired moiré patterns provides an estimation for the surface refractive index and the SPP propagation length, which both prove to be in good agreement with values derived from literature bulk values. Moreover, a characteristic phase shift of π is observed in the CD PEEM images for the SPPs launched at opposite edges, which is a direct consequence of the plasmonic spin-Hall effect and hence not present for excitation via linear polarized light.

We conclude that the observed interference patterns result from excitation of SPPs on $\text{Ni}_{80}\text{Fe}_{20}$, which are directly detectable via plasmonic dichroism in PEEM.

This plasmonic dichroism technique can therefore be used to quantify the surface refractive index. Our results can be further extended to many magnetic materials for the simultaneous study of plasmonic and magnetic phenomena. Since we do not observe any magnetic signal in CD PEEM for the $\text{Ni}_{80}\text{Fe}_{20}$ microstructures currently used, we cannot conclude on the sensitivity of the plasmonic spin-Hall effect to the magnetization direction. However, results on magnetoplasmonic multilayers demonstrate strong magnetization-sensitive effects in the non-linear regime [163, 164]. Naturally, trying to find a direct influence of the magnetization on the detected SPP or vice versa would be an interesting extension of the results presented so far. For this, we propose using epitaxially grown microstructures with higher surface quality than the sputtered samples used here. Since, in principle, every metal is plasmonic of some sort, other ferro-, ferri- or even antiferromagnetic metals could be investigated by our current approach, which would allow to explore the interesting interplay between magnetic and plasmonic properties on nanometer and femtosecond spatial-temporal scales via CD PEEM imaging.

Chapter 4

Ferromagnetic Dichroism in threshold PEEM

This chapter covers the use of near-threshold PEEM as a tool for imaging ferromagnetic domains. After a brief literature review, the basics of ferromagnetism and ferromagnetic domains at surfaces are introduced. The group theory approach is explained and applied for ferromagnetic Ni thin films and Fe single crystals, for which experimental results and theoretical calculations are presented and discussed. An outlook on upcoming time-resolved thin film experiments concludes this chapter.

4.1 Introduction

Near-threshold PEEM as a tool for investigating magnetic surfaces is still an uncommon technique in the community. In most textbooks it is not even mentioned as a viable possibility [165–167]. The reason may be that common alternatives, namely XPEEM, spin-filtered PEEM and MOKE microscopy, cover a broad parameter space and can be used for the investigation of many different material classes. Especially MOKE has the benefit of a comparably simple setup and, in most cases, a simple sample preparation prior to the measurement. Nevertheless, concerning surface science, near-threshold PEEM has undeniable advantages over these alternative techniques. It combines the high spatial resolution of XPEEM with the convenience of a tabletop in-lab setup. In addition, it is a much more surface sensitive technique, due to use of slow electrons. With an appropriate laser setup, the theoretical spatial and temporal resolution is unrivaled when it comes to investigating magnetic domains in the lab [168, 169]. In contrast, spin-resolved PEEM, which can be considered the counterpart to the valence-band dichroism approach presented here, needs a more sophisticated setup, higher acquisition times, as well as additional mandatory energy filtering [170]. This renders the technique unserviceable for ultrafast experiments.

The first experimental evidence of linear magnetic dichroism in near-threshold PEEM was found by Marx *et al.* in 2000 [171]. They chose to investigate a 100 nm

polycrystalline Fe film on silicon, revealing a small asymmetry of 0.37%. Although consistent with theory and a nice proof of concept, the resulting asymmetry pictures are not very impressive and also subsequent publications have not convinced the field to popularize this technique [172]. After that, many spectroscopic studies followed, investigating the existence of circular and linear dichroism in several ferromagnetic materials [173–177]. Predominantly Nakagawa *et al.* built on the first experimental work of Marx. They pushed the technique to the next level by choosing Ni films adsorbed with Cs as their system of interest. These samples showed large asymmetries up to 12% in circular dichroism PEEM [155, 178, 179]. This is also the first time that pulsed laser light was used for dichroism imaging. Due to the limited photon energy of commonly available optical laser setups, Cs is still needed in photoemission experiments to reduce the surface work function [180, 181]. *Cw* lasers were also used for static imaging of other materials, such as nanodomains at the LaAlO₃/SrTiO₃ interface [90, 182, 183]. Notably, domains at the FePt surface were investigated utilizing a pulsed deep-UV laser with a photon energy of 7 eV [184]. The obvious next step in developing this technique is the combination with a high-order harmonic generation (HHG) chamber, which was tested recently [185].

Despite the remarkable progress in the past 20 years, magnetic dichroism imaging in near-threshold PEEM remains a niche technique. It is still to be seen, whether it is possible to successfully use it to measure ultrafast magnetic dynamics at a better spatial-temporal resolution than MOKE. For example, at the time of writing, there is still no record of successful all-optical switching of a magnetic domain in near-threshold PEEM.

The aforementioned magnetic sensitivity is only achieved under very specific circumstances, concerning the experimental setup itself as well as the sample of interest. Regarding the setup, UHV conditions are needed. As is shown in Section 4.2.4, the excitation geometry must be carefully chosen in regard to the magnetic state of the surface. Ideally, the setup should allow for sample heating and cooling in order to cross the Curie or Néel temperature. Furthermore, for changing the magnetization-dependent contrast, switching the magnetization is experimentally favored above changing the polarization of the illuminating light. Especially for linear dichroism via grating incidence, the difference of the electric field component perpendicular to the surface (k_{\perp}) between s and p polarization leads to drastically different photoelectron yields, hence, decreasing the quality of asymmetry images when switching the polarization rather than the magnetization direction. In contrast to MOKE, the combination of an *in situ* magnet with a photoelectron microscope is at least challenging, if not impossible, depending on the specific setup.

This emphasizes that some compromises are inevitable in order to get satisfactory

results. The magnetic and electric properties of the sample of interest are critical to have a chance to measure any magnetic dichroism in near-threshold PEEM: First, the electronic ground state must be spin polarized and ideally, there should be a sufficiently large Stoner splitting present in the thin-film band structure close to the Fermi level. Second, the wave function should be subject to spin-orbit coupling (SOC). Third, the film should be well ordered at the surface. Additionally, the geometry, i.e. the direction of the magnetization vector M in relation to the polarization vector P , must be known, stable and properly chosen according to the theory explained in Section 4.2.4. Especially for time-resolved experiments, which rely on a stroboscopic recording of the data, the magnetic, electric and thermal stability and reversibility of the ferromagnetic state is crucial.

Hence, the following section gives a theoretical introduction to magnetic dichroism in near-threshold PEEM, followed by a section describing the experimental implementation of these concepts. Since general aspects are already given in Section 2.1 and 2.2, the focus is put on the details of these specific measurements. In Section 4.4, some exemplary experimental results for Ni/Cu(100) are shown and discussed, providing the proof of concept of the experiment. These findings are then extended by looking at *ip* domains of the Fe(100) single crystal surface. Throughout these sections, OMNI calculations support the respective discussions.

4.2 Theory

Building on the theory of general photoemission introduced in Section 2.1.1, a short theoretical description of ferromagnetism and ferromagnetic domains is given in the following. Based on this, a strategy for the optimal imaging of these domains by means of near-threshold photoemission is developed. For a deeper theoretical background, the reader may consult the books about magnetism by Stöhr and Siegmann [167] and Hubert and Schäfer [166]. Here, we introduce ferromagnetism including the quantum-mechanical backbone needed to understand the valence-band dichroism discussed in Section 4.2.4. Still, for all mechanisms, we use the semi-classical, intuitively understandable single-particle picture, omitting the fully relativistic many-body description. The latter is briefly addressed in Appendix B. We also skip more exotic interactions like RKKY (Ruderman-Kittel-Kasuya-Yosida [186–188]), since they do not play a role in the upcoming discussions.

4.2.1 Ferromagnetism

In a ferromagnet, the spatial spin orientation is determined by the orientation of the intrinsic magnetization $M(\mathbf{r})$, which may change throughout the sample. The physical origin of the collective parallel (ferromagnetic) or anti-parallel (antiferromagnetic) alignment of magnetic moments is the exchange interaction, expressed by the respective Hamiltonian H_{ex} . This can be seen as the intrinsic *magnetic* contribution acting on the spin. A *non-magnetic* contribution stems from SOC, represented by H_{SO} , coupling the electron spin to the orbital part of the wave function, i.e. the real space in form of the crystal lattice. Thus, the crystal structure introduces anisotropies. A third interaction couples the electron spin to an external magnetic field, which is known as the Zeeman interaction, represented by H_{B} .

In the following textbook example, a single electron moves in an electrostatic potential $V(\mathbf{r})$. Hence, a Hamiltonian H acts on its wave function $|\Phi(\mathbf{r})\rangle$ in the following way:

$$H|\Phi(\mathbf{r})\rangle = E_{n,k}|\Phi(\mathbf{r})\rangle = E_{n,k}|n, D, \mathbf{k}, s\rangle \quad . \quad (4.1)$$

Here, $E_{n,k}$ are Bloch states and $|n, D, \mathbf{k}, s\rangle$ is a set of eigenfunctions represented by the respective quantum numbers, with n being the principal quantum number, D the irreducible representations of the symmetry group of the crystal and s the electron's spin. Including the spin leads to the classical time-independent description of the single-electron system via the Pauli equation [49, 189]:

$$H|\Phi\rangle = (H_0 + H_{\text{D}} + H_{\text{B}} + H_{\text{SO}} + H_{\text{ex}})|\Phi\rangle = E|\Phi\rangle \quad . \quad (4.2)$$

H_0 is the Hamiltonian of the well-known, time-independent Schrödinger equation, describing the hypothetical *spin-free* situation, but introducing the vector potential of the magnetic field \mathbf{A} acting on the moving charge. Hence, it can be split into a kinetic part T and the potential $V(\mathbf{r})$:

$$H_0 = T + V(\mathbf{r}) = \frac{1}{2m} (\hat{\mathbf{p}} - e\mathbf{A})^2 + eV(\mathbf{r}) \quad . \quad (4.3)$$

Here, e refers to the electron charge, m is the electron mass and $\hat{\mathbf{p}}$ is the momentum operator. H_{D} is the so-called Darwin term, which is a relativistic energy correction term and has no classical interpretation. The Hamiltonian of the magnetic field \mathbf{B} acting on the electron is described by

$$H_{\text{B}} = e\mu_{\text{B}}\hat{\sigma} \cdot \mathbf{B} \quad , \quad (4.4)$$

connecting the Pauli spin operator $\hat{\sigma}$ with \mathbf{B} , which breaks time-reversal symmetry

and causes a splitting of previously degenerate bands known as the Zeeman effect. μ_B is the Bohr magneton defined by $\mu_B = \frac{e\hbar}{2m}$. The interplay between the lattice and the spin is described by the spin-orbit Hamiltonian:

$$H_{\text{SO}} = -\frac{\mu_B}{2m} \hat{\sigma} \cdot (\mathbf{E} \times \hat{\mathbf{p}}) \quad . \quad (4.5)$$

\mathbf{E} is an electric field acting on the moving electron. It also lowers the symmetry of the system by introducing an electrostatic crystal potential $\mathbf{E} = \nabla V(\mathbf{r})$. Again, by lowering the symmetry, band degeneracies are lifted. The resulting spin-orbit split bands contain a superposition of both spin flavors each. Last, H_{ex} describes the aforementioned exchange interaction, which is often written in the intuitive Heisenberg way:

$$H_{\text{ex}} = -2J_{\text{ab}} \langle \mathbf{s}_a \cdot \mathbf{s}_b \rangle \quad , \quad (4.6)$$

where J_{ab} is the Heisenberg exchange constant connecting the two spins \mathbf{s}_a and \mathbf{s}_b , resulting in a parallel alignment for $J_{\text{ab}} > 0$, and antiparallel alignment for $J_{\text{ab}} < 0$. However, in the picture of a single electron moving in a potential, equation 4.6 is not appropriate. An easy description derived from the fully relativistic Dirac formalism was developed by Stoner-Wohlfarth [190], expressing the many-electron problem by a set of single-electron Kohn-Sham equations, which simply gives:

$$H_{\text{ex}} = \pm eV_{\text{ex}}(\mathbf{r}) \quad . \quad (4.7)$$

Here, $V_{\text{ex}}(\mathbf{r})$ is the exchange and correlation potential. The \pm signs indicate the impact of the exchange interaction on majority $|\uparrow\rangle$ or minority $|\downarrow\rangle$ spins, which makes the Hamiltonian spin-dependent.

Considering all explained interactions present in a well-ordered crystal and a positive J_{ab} results in an overall ferromagnetic orientation of the electron spins. At the surface, the spatial symmetry is lowered resulting in an additional contribution to the anisotropy. Up to now, we only considered *local* effects acting on an electron. When dealing with macroscopic systems, also *non-local* effects play a role. These are a direct consequence of any system's structural finiteness. Non-locality means that the magnetization in a given point of the sample is influenced by the magnetization in every other point, and vice versa. Introducing a surface gives rise to an additional stray-field energy, and the presence of different crystallographic order can cause the hard axis of the magnetization to orient differently, which gives rise to a magnetostrictive self-energy. These effects result in the formation of magnetic domains, described in the famous domain theory by Landau-Lifshitz [154] and Kittel [191].

4.2.2 Domain theory

In principle, the exchange interaction should produce a homogenous magnetization of a sample below the Curie temperature. It is apparent that this is not the case by measuring the magnetization of a ferromagnet in absence of external magnetic fields. The observed magnetization is generally lower than the saturation magnetization. Impurities, surfaces, edges or other boundaries create anisotropy contributions, which can cause the magnetization to vary throughout the sample. However, exchange interaction still forces the magnetization to be locally saturated, which entails the formation of magnetic domains. In other words, they are the result of the inherent finite nature of any magnetic system and its minimization of the total magnetic energy.

The domain state of the system in equilibrium is determined by considering all relevant magnetic energy terms. There are several names for these terms used in literature, which can cause confusion since some very similar terms even mean very different things. First, we already introduced the exchange energy H_{ex} favouring parallel or antiparallel alignment of neighboring spins. This shall not be confused with exchange interface coupling or exchange anisotropy, which is present at the interface of a ferromagnet and an antiferromagnet giving rise to exchange bias [192]. Second, there exists a zoo of anisotropy energies. Caused by SOC, they are sometimes called magnetocrystalline anisotropies. They can be further distinguished between *crystal* anisotropies, covering the impact of the undisturbed, ideal crystal, and *induced* anisotropies, covering the impact of defects. These SOC-related effects include, depending on the symmetry of the crystal, cubic anisotropy K_c , uniaxial and orthorhombic anisotropy K_u and K_o , and surface and interface anisotropy K_s and K_i caused by the symmetry breaking, which are important when dealing with thin films. Third, we have the magnetostatic or stray-field energy, which is reduced by minimizing the magnetic field outside the sample, often leading to closed loop formations in microstructures (see for example Figure 3.7(c)). Confusingly, this contribution is sometimes called shape anisotropy, although it is related to dipole effects rather than SOC. The creation of magnetic domains generally decreases the stray-field energy, but increases the other terms. Last, the relevance of the exchange interaction means that the presence of differently aligned domains next to each other also increases energy, since the magnetization has to continuously rotate from one state to the other. Hence, a domain-wall energy is introduced to account for this canting of magnetic moments. Hereby, Néel- and Bloch-type domain walls are generally distinguished, which describe a rotation of the moments perpendicular or parallel to the domain wall, respectively. Due to stray-field energy, Néel-type walls are often found at surfaces, while Bloch-type walls are mostly present within the

bulk.

In this work, we are only concerned with thin films and bulk crystals of conventional ferromagnetic metals like Fe, Ni and alloys of the two. These are cubic crystals with generally low anisotropies. The specifics of each system are discussed later. We also do not apply any external magnetic fields, hence, we only investigate the equilibrium state of the film after growth. Predicting the exact domain size and shape requires advanced simulation approaches incorporating the energy considerations explained above. In principle, two methods are widely established for this task, namely micromagnetic simulations (like mumax3 [193]) and atomistic spin simulations (like VAMPIRE [194]). The first are ideal to calculate non-local, mesoscopic effects like magnons, spin-currents and magnetic domains by simulating interactions between arbitrarily large magnetic moments, whilst the latter struggle with large systems, but give very good results predicting local effects like demagnetization, Curie temperature or the local magnetic order by calculating the interaction between single atoms, i.e. their spins. Without these numerical simulations, it is not easy to predict the exact domain patterns aside from the general alignment of \mathbf{M} and the approximate domain size.

4.2.3 Kerr-like magnetic dichroism

As already mentioned, the first experimental observation of magnetic domains in near-threshold PEEM on an iron thin-film surface was published by Marx *et al.* [171]. In this paper, the authors also proposed a Kerr-like mechanism as an explanation for the observed linear dichroism, which was also supported by Schönhense and Schneider [50, 195]. This theory combines the magneto-optical Kerr rotation picture [196] with the near-threshold photoemission models in free-electron Drude metals resulting in an anisotropic volume photoelectric effect already developed in the 1970s [197, 198]. According to these groups, the model provides quantitative estimations for the expected asymmetry in agreement with their measurements.

The basic idea of this Kerr-like dichroism is schematically depicted in Figure 4.1(a) and (b), showing the situation for opposite in-plane (*ip*) magnetization, respectively. Linear, *p*-polarized light impinges on the surface under oblique angle of incidence and is refracted due to the different refractive index ϵ of the bulk. The refracted-light trajectory is marked by the dashed line. Due to the magnetization \mathbf{M} of the sample, an additional refractive component increases or decreases the angle of refraction ϑ by a Kerr angle ϑ_K . This is introduced by the displacement vector $\mathbf{D} = \epsilon\epsilon_0\mathbf{E}$, where ϵ includes off-diagonal components caused by \mathbf{M} . The displacement shifts the probed probability distribution of the electrons, i.e. the probed orbitals marked by the grey circles. The physical origin of this shift is the Lorentz force. The observed

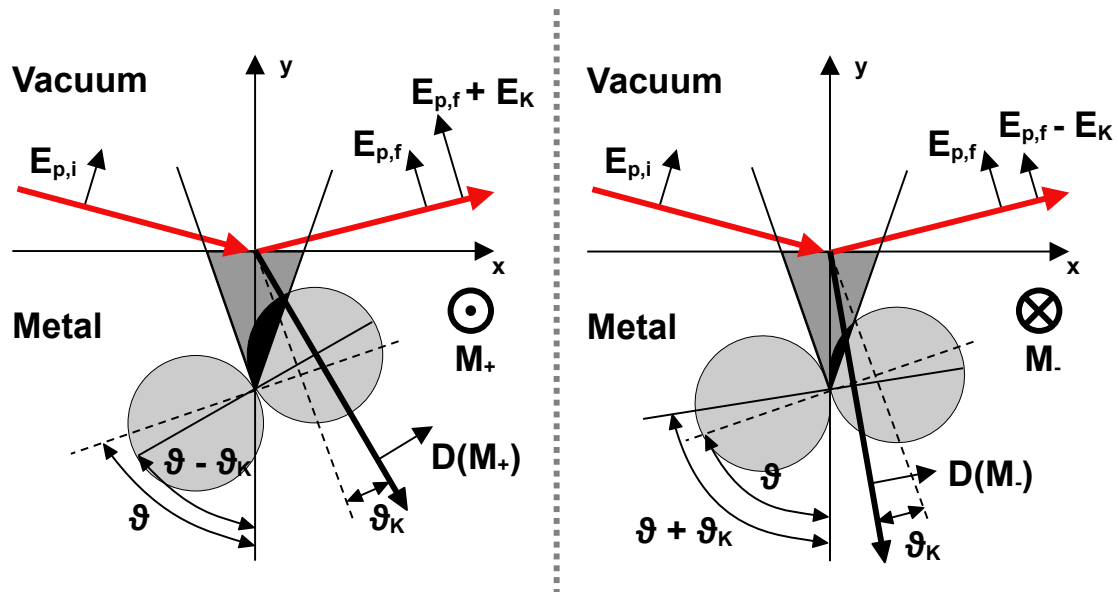


Figure 4.1: Schematic illustrating the Kerr-like magnetic dichroism effect. Adapted from Marx and Schönense [171, 195].

intensity in PEEM results from the overlap between the electron distribution and the observation cone, i.e. the escape angles of the photoelectrons observable in the microscope, which is $\pm 10^\circ$ from the surface normal [171]. This overlap changes due to the opposite displacement caused by antiparallel magnetic domains, hence, an asymmetry between both orientations of M can be observed.

In case of Marx *et al.*, this model seems to correctly reproduce the experimental conditions and observations [171, 172]. However, it is not very useful as a predictive model, since it does not allow for a qualitative or quantitative prediction for other setups or materials. First, the model completely ignores the crystallographic order of the surface. As shown in Section 2.1.1, the photoemission yield depends on the relativistic band structure via dipole selection rules, introducing the importance of the lattice and the overall experiment geometry. In their work, they only focus on polycrystalline materials, without specifying the impact of different ordering. Second, the relation between P and M is only discussed in this highly specific case, where $P \perp M$ and a Lorentz mechanism can be used. Other geometries like circular polarization or normal incidence are not discussed and cannot be derived in a straightforward way from this model. Third, the shape of the probability distribution is not properly explained. In Figure 4.1 it looks like a p orbital, whereas in Fe, Co and Ni, d orbitals are probed by near-threshold photoemission.

In conclusion, the Kerr-effect-like model may give a good quantitative estimate of the expected magnetic asymmetry in PEEM for specific polycrystalline samples, but it does not have any predictive capabilities due to the somewhat arbitrary analogon to the MOKE.

4.2.4 Magnetic valence-band dichroism

The theory of valence-band dichroism was predominately developed in the 90s and early 2000s by Feder, Henk, Kuch, Schneider and Venus [49, 199–203] and supported by pioneering experiments of Tamura, Schmiedekamp and Hild [42, 174–176, 204]. It is derived from calculating the relativistic band structure for a specific crystalline system in combination with the photoemission model described by equation 2.4, which allows to calculate the resulting photoelectron yield for different symmetric cases of P and M . The ingenuity of this approach is its power of predicting qualitative results for very different experimental setups by reducing the elusive, quantum-mechanical problem to a simplified mathematical, group-theoretical problem. This is why it is sometimes referred to as the group theory approach. As already mentioned, the help of appropriate calculations is needed to obtain quantitative results. Nevertheless, the fact that we can reduce the intricate physics at hand to a group theory problem is a very astonishing example of *the unreasonable effectiveness of math in science* [205].

In this group theory approach, a qualitative answer to the question of the existence of magnetic dichroism in a material boils down to answering the question: Is there a symmetry operation on the point group of the crystal and the associate vectors k_A, q_A, P_A and M_A , which unambiguously transfers the system into k_B, q_B, P_B and M_B ? If the answer to said question is yes, then there is no magnetic dichroism when comparing both configurations. If the answer is no, then there is magnetic dichroism [49].

Again, this rule says nothing about the size of the asymmetry. This implies that, theoretically, magnetic dichroism might cause an asymmetry, but it may be too small in order to detect it. We apply this symmetry argument to a simple scenario as depicted in Figure 4.2. It shows the experimental geometry in the Femto-PEEM chamber when dealing with *ip* magnetization and a fourfold symmetric crystal. Actually, this case becomes relevant in Section 4.5 where we discuss *ip* domains of Fe(001) single crystals. By equivalent considerations, other geometries can be ruled in or out.

Figure 4.2(a) shows the magnetization \mathbf{M} pointing along the high-symmetry [100] direction, which we define as the x direction, and lcp light σ_+ lets the polarization \mathbf{P} point in $-\mathbf{q}$ direction. The light impinges on the surface with an arbitrary altitudinal angle $0^\circ < \theta < 90^\circ$ ($\theta = 65^\circ$ for the Femto-PEEM), and the incidence plane is kept parallel to the [100] direction, i.e. the azimuthal angle $\phi = 0^\circ$. For simplicity's sake, we ignore the escape direction \mathbf{k} of the photoelectron and just set it normal to the surface plane. The respective point group of the crystal in the magnetic case is the C_{2v} group, which includes the following symmetry operations: E , the identity, σ_{xz} and σ_{yz} , the reflections at the xz and yz plane, and C_2 , the 180° rotation around the z axis. It is important to remember that \mathbf{k} and \mathbf{q} (and \mathbf{P} for the lp case) are polar vectors, whereas \mathbf{M} and σ (i.e. \mathbf{P} for the cp case) are axial vectors, which means that the latter reverse under parallel reflection. Hence, σ_{xz} and σ_{yz} flip \mathbf{M} , but for oblique angle of incidence, only σ_{xz} flips \mathbf{P} , whilst σ_{yz} leaves \mathbf{P} invariant, but changes \mathbf{q} . Therefore, changing the excitation from lcp to rcp flips \mathbf{P} , which is a change of the system from configuration A to configuration B. This change cannot be transformed via symmetry operations into one another, without changing another vector of the system. Consequently, according to the group theory approach, there must be MCD for \mathbf{M} parallel to the incidence plane. Figure 4.2(a) summarizes these explanations in a symmetry table. They are also visualized in a schematic, where σ_{xz} changes the direction of both \mathbf{M} and \mathbf{P} . Contrary, Figure 4.2(b) shows a different configuration, where \mathbf{M} points along the crystal [010] direction (y direction), hence $\mathbf{M} \perp \mathbf{q}$. The other vectors are unchanged as compared to panel (a), so switching from lcp to rcp again is the same as mirroring the system at the xz plane via σ_{xz} . This operation now only switches \mathbf{P} but leaves \mathbf{M} unchanged (both are axial vectors!). Consequently, switching between lcp and rcp light does not result in MCD.

Now, the band structure of the system determines the size of the asymmetry. This implies some important consequences. First, if there is magnetic dichroism detected at a core level, i.e. in XPEEM, than there is magnetic dichroism in threshold PEEM, too, since the symmetry arguments do not change with energy [200]. However, the band structure may reveal no available states for a certain energy. Second, if spin polarization exists in a non-magnetic material, the same experiment performed in a magnetic material will contain magnetic dichroism, given that all experimental parameters and symmetry properties are identical. In other words, whenever SOC creates a spin polarization parallel or antiparallel to the magnetization direction, magnetic dichroism occurs, since, again, the underlying symmetry argument does not change [199].

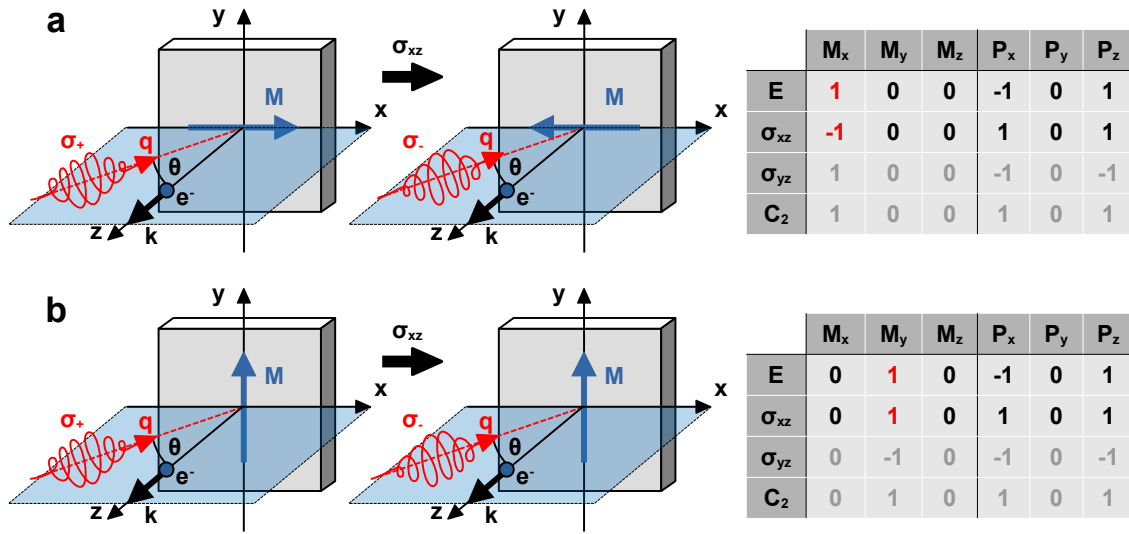


Figure 4.2: Schematic summary of the group theory argument for a cubic crystal and ip magnetization. **(a)** Experimental configuration for $M \parallel [100]$ and lcp light under oblique incidence. The schematic on the **left** shows the result of a σ_{xz} reflection. The table on the **right** summarizes all possible symmetry operations for the C_{2v} point group and the resulting M and P , with the switch from lcp to rcp causing MCD (marked in red). **(b)** Same logic for $M \perp q$ does not result in MCD, since σ_{xz} switches P without changing M (marked in red).

4.3 Experimental details

The proof-of-principle experiments for visualizing magnetic dichroism in threshold PEEM were performed with the Hg lamp (see Section 2.1.2) and the dichroism setup (see Section 2.2). Our material system of choice is Ni/Cu(100), which is already well understood and heavily studied in the literature. It is expected to show large oop domains as well as high asymmetry in threshold photoemission of up to 10% for 12 ML thin-films [155, 179, 180, 206, 207]. The magnetization of Ni(100) surfaces crosses a spin-reorientation transition (SRT) from ip to oop at around 8-10 ML [208, 209], which depends highly on adsorbates and surface roughness [210]. Compared to the fcc bulk structure, Ni films grow pseudomorphically on Cu(100) due to a lattice mismatch of $a_{Ni} = 3.56 \text{ \AA}$ versus $a_{Cu} = 3.61 \text{ \AA}$, causing a tetragonal distortion which builds up until 11 ML, after which it starts to relax [206, 211, 212]. This results in the famous behavior of switching from ip to oop magnetization at 8-10 ML and then switching back from oop to ip at 37-50 ML. This SRT is often described by the interplay of different contributions to the second-order magnetization-anisotropy energy K_2 , where

$$K_{2v} + \frac{K_{2s} + K_{2i}}{d} > 2\pi M_s^2 \quad (4.8)$$

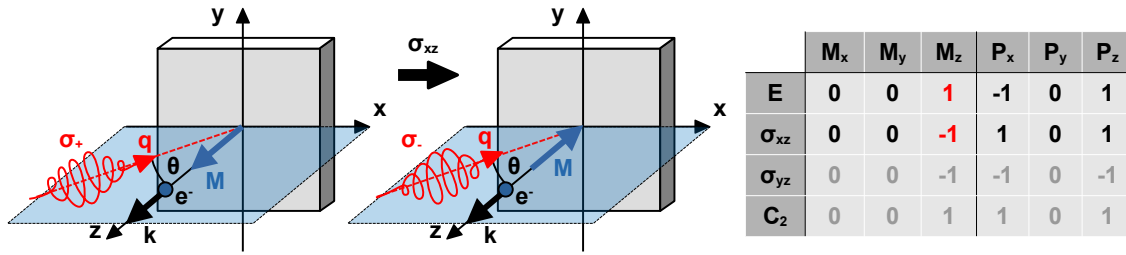


Figure 4.3: Schematic summary of the group theory argument for a cubic crystal and *oop* magnetization. Experimental configuration for $M \parallel k$ and *lcp* light under oblique incidence. The schematic on the **left** shows the result of a σ_{xz} reflection, and the table on the **right** summarizes all possible symmetry operations for the C_{2v} point group and the resulting M and P , with the switch from *lcp* to *rcp* leading to MCD (marked in red).

results in *oop* magnetization. Here, M_s is the saturation magnetization, d is the layer thickness, K_{2v} is the positive volume anisotropy and K_{2s} and K_{2i} are the thickness-independent surface and interface anisotropies [209, 210]. For Ni, K_{2v} becomes thickness dependent due to the relaxing strain. Hence, K_{2v} decreases with increasing d , which causes the second SRT from *oop* to *ip*. This SRT property is contrary to other ferromagnets like Fe or Co [213].

Starting from a cubic crystal, *oop* magnetization reduces the symmetry further. Consequently, MCD should always be present in oblique and normal incidence setups according to the group theory approach explained in the previous section. The case for oblique incidence is shown in Figure 4.3, analogue to the discussion in Figure 4.2.

To optimally use the spatial resolution offered by our PEEM setup, we epitaxially grew wedges of Ni on Cu(100) single crystals. The Cu crystals were cleaned in UHV by cycles of 5 min Ar sputtering at 1 keV and subsequent annealing to 830 K for 30 min. The cleanliness and crystallographic order was checked via XPS, AES and LEED, after which we evaporated 20 ML Ni at a base pressure of 3×10^{-9} mbar from a Ni-rod via MBE with the substrate held at RT. The film thickness was monitored via a QMB, calibrated against the damping of the substrate peaks in XPS. The wedge was either fabricated by using a shadow plate or by moving the circular crystal off-center relative to the center of the focused evaporation spot. While the latter method creates an ill-defined thickness profile, the shadow plate in front of the sample creates a well-defined wedge. These samples were grown by the PhD candidate Friederike Wüthrl in our group. The plate is mounted to the manipulator at a distance of 5 mm from the surface, blocking half of the circular crystal when looking directly normal to it. By rotating the manipulator by $\pm 13^\circ$ back and forth during evaporation, a continuous wedge forms, covering thicknesses ranging from 0-20 ML.

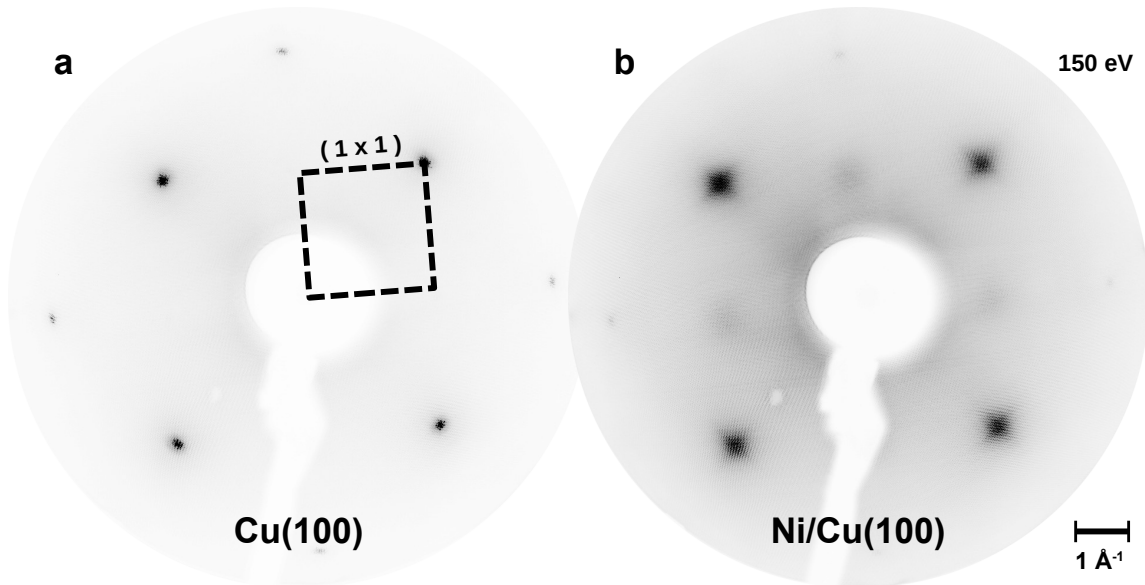


Figure 4.4: (a) LEED measurements of a clean Cu(100) surface at $E_{\text{kin}} = 150$ eV and 0.25 s acquisition time. (b) Same measurement after evaporation of nominally 12 ML Ni (0.8 s acquisition time).

The surface structure of the Ni film was checked afterwards by LEED. The corresponding measurement for a clean Cu(100) surface at 150 eV electron kinetic energy is shown in Figure 4.4(a). Figure 4.4(b) depicts the LEED pattern of the same sample after evaporation of nominally 12 ML Ni. The first reveals sharp diffraction spots and the (1x1) surface structure. After evaporation, the spot width increases while the peak intensity strongly decreases, with the background intensity relatively increased. This observation is typically explained by the formation of a Ni(001) film that is not properly ordered. The partial order causes deviations from the perfectly ordered Cu(100) crystal, as expected for room-temperature evaporation [212].

For the detection of magnetic *ip* domains, we chose an Fe(100) single crystal. At room temperature and ambient pressure, Fe grows in a bcc structure, but undergoes a phase transition to fcc above 1183 K [214]. Figure 4.5 shows the AFM, MFM and PEEM characterization of the Fe(100) crystal used in this work. The AFM image in Figure 4.5(a) reveals well-ordered Fe terraces and 4.5(b) depicts the respective MFM information. The 180° and 90° Bloch-type walls are clearly distinguishable by the contrast in MFM. Additionally, the direction of the grain structure visible in the MFM images within an *ip* domain resembles the direction of M , which is marked by the arrows.

The 180° walls tend to be slightly skewed and not perfectly straight. They are also influenced by surface defects, which is apparent in Figure 4.5(c). Previous publications on Fe single crystals suggested the transition from Bloch-type walls in the bulk to Néel-type walls at the surface, which reduces the stray field. Upon this

transition, for thick films, the wall width remains constant at around (210 ± 40) nm [215]. Since MFM is only sensitive to *oop* domains, we detect the bulk magnetization in Figure 4.5(b) and (c). Alternatively, the magnetic MFM tip might influence the Néel-type walls, forcing them *oop*. However, we can rule out a strong influence from the tip, since it contradicts the observation of different magnetization directions for different domain walls in Figure 4.5(b).

Our bcc crystal was grown with manganese, which is apparent by the large black hole in the AFM image in Figure 4.5(a). Upon introduction into UHV, the sample was cleaned by cycles of sputtering and flash annealing. The challenging part for the preparation of clean Fe(100) surfaces is the removal of large amounts of carbon and nitrogen, the latter dissolved in the bulk [216, 217]. By flash annealing, a nitrogen free zone forms close to the surface. Nitrogen from the bulk quickly refills this zone after prolonged annealing or at higher temperatures. The surface magnetization does not significantly change by these preparation steps [215], forming several tens of micrometer *ip* domains oriented along the high-symmetry directions. Afterwards, the cleanliness and crystallographic order of the surface was checked via LEED, revealing bright spots, hence, a monocrystalline structure. However, some Mn impurities remained, which are apparent as dark holes in the PEEM image in Figure 4.5(d). Between these holes, large terraces of clean, well-ordered Fe are present.

4.4 Results & Discussion

4.4.1 Out-of-plane domains on Ni/Cu(001)

Proof-of-principle experiments

We demonstrate the imaging of MCD via near-threshold PEEM with a 20 ML thin film on Cu(100). Figures 4.6(a) and (b) show the background-corrected PEEM images obtained for *lcp* and *rcp* UV light, respectively. The FoV is 80 μm . The dominant features in both images are a pit in the center, dark lines on the left and an island structure in the top right. For the latter, a contrast reversal is observed upon varying the helicity of the light source. This varying contrast is attributed to ferromagnetic domains. Since these are background-corrected images, the slight ferromagnetic contrast is not visible during live imaging in PEEM. Figure 4.6(c) shows a CD PEEM image, calculated from panel (a) and (b) according to equation 2.10. In this dichroism image, all contrast mechanisms independent of the helicity of the light cancel out, whereupon only the ferromagnetic contribution is left. As a consequence, the large defect in the center of (a) and (b) is not present in (c), and the overall ferromagnetic

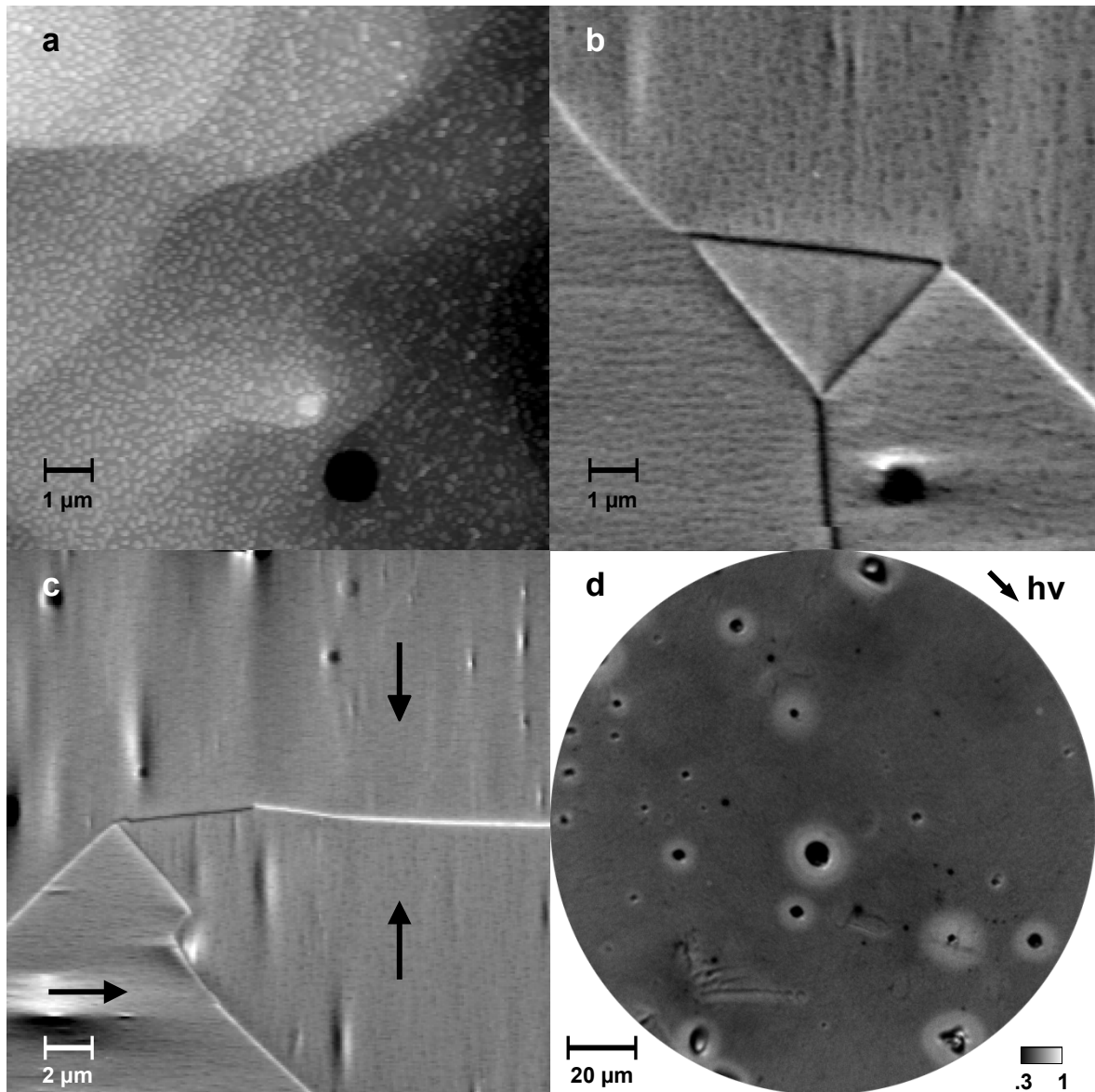


Figure 4.5: (a) AFM image of an Fe(100) single crystal. (b) Respective MFM image, revealing *oop* magnetized areas. Since M lies *ip*, MFM only detects the Bloch-type domain walls. (c) Zoomed-out MFM image again revealing domain walls. Arrows mark the appropriate direction of M . (d) Background-corrected PEEM image of the Fe(100) single crystal after cycles of sputtering and annealing.

contrast enhances. Several dark domains of irregular shape are now clearly visible, with an average domain size of $\approx 50 \mu\text{m}$. The observed asymmetry in Figure 4.6(c) is $\approx 3\%$ at $E_B = 0.3 \text{ eV}$. The edges of the domains are preferably oriented along a direction which is 45° from the horizontal, from bottom-left to top-right. Additionally, almost every dark domain is connected to a surface defect. After heating the sample above T_C , the domain pattern vanished, but the asymmetry is still measurable. Additionally, the number of observable defects decreased, which means that a well-ordered film favors a quasi single-domain state.

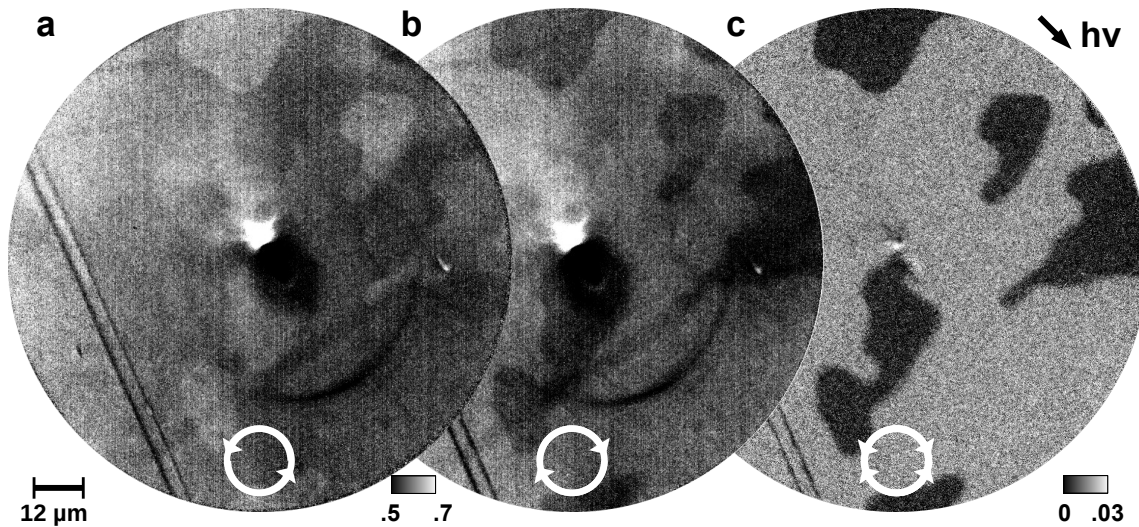


Figure 4.6: (a) & (b) Oblique incidence PEEM images of 20 ML Ni/Cu(100) at 5.2 eV for *lcp* and *rcp* light, respectively. (c) CD PEEM image at $E_B = 0.3$ eV resulting from (a) and (b) according to equation 2.10, revealing a clear ferromagnetic domain contrast.

We repeat the experiment on the same sample with NI excitation. Figure 4.7(a) and (b) show the NI PEEM images for *lcp* and *rcp* light, respectively. Here, bright islands are located in the center of the images, as well as bright areas in between this defect structure. The latter changes the contrast upon switching the helicity. Additionally, the right part of the images appears brighter than the rest. This is due to the shadow of the NI mirror being overcorrected during background subtraction. The CD PEEM image shown in Figure 4.7(c) only includes the helicity-dependent, ferromagnetic contrast. In this image, we observe a slightly increased asymmetry of $\approx 4\%$. This increased asymmetry is caused by the decreased angle of incidence, where $A = A_0 \cos \theta$, with A_0 being the maximum achievable asymmetry. This fits the previously observed asymmetry of 3% in case of oblique incidence.

Generally speaking, NI PEEM images inhibit almost no topography contrast, since the light is not blocked by structures perturbing the flat surface. The contrast of the islands observed in Figure 4.7(a) and (b) stem from a different work function, i.e. a different material. Disadvantageously, the additional NI mirror results in an ill-defined polarization state after reflection in case of incoming *cp* light. The actual polarization after reflection can be estimated by the Fresnel equations [218] and the optical parameters for Rh taken from literature [219]. The intensity and phase after reflection is different for *s*- and *p*-polarized light, resulting in elliptical polarization. This may be one reason for the smaller asymmetry contrast as compared to the 10% reported in literature [155].

Bearing in mind the work function of bulk Ni, these are the first near-threshold

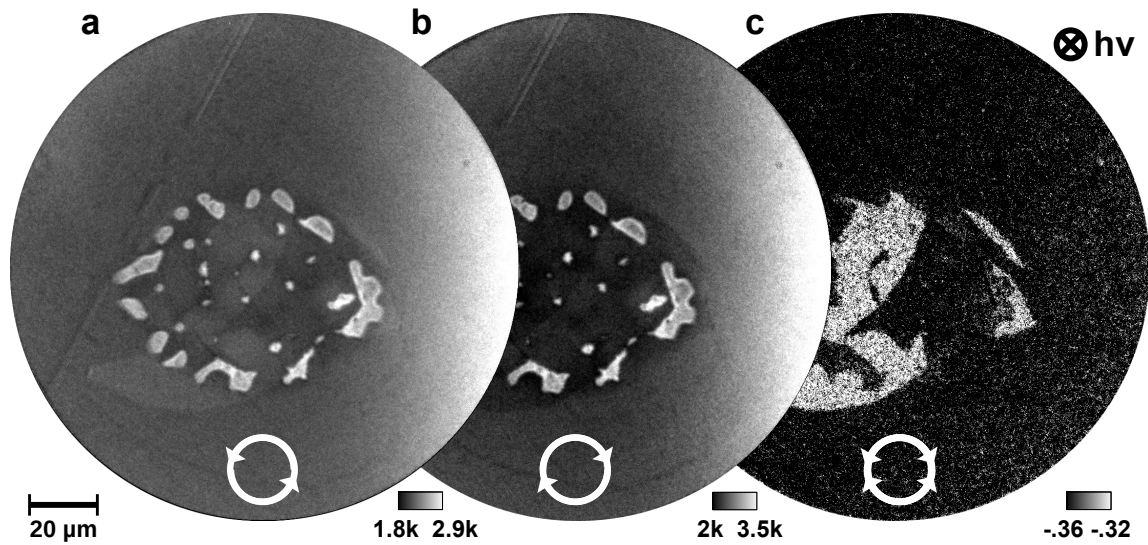


Figure 4.7: (a) & (b) NI PEEM images of 20 ML Ni/Cu(100) at 5.2 eV for *lcp* and *rcp* light, respectively. (c) CD PEEM image resulting from (a) and (b) according to equation 2.10.

MCD images of a *pure* Ni film on Cu(100). In all studies so far, the work function of a Ni film was reduced by depositing small amounts of Cs to adapt it to the excitation energy [155, 177, 178, 180]. In the setup presented here, we can either adjust the laser wavelength to the threshold of the sample, or use the mercury lamp with 5.2 eV in combination with the imaging energy filter (IEF). Hence, we do not actively adapt the work function with Cs.

By exciting electrons near the threshold, the ferromagnetic contrast of the asymmetry images is not significantly distorted by the secondary electron background. This phenomenon is shown in Figure 4.8. The red solid line marks the trend of the differential photoelectron yield with increasing E_B . The total width of the spectra marks the width of the total accessible electron energy range. A larger scanning range from 0 to 1 eV revealed a width of ≈ 0.7 eV. Using equation 2.1, we estimate $W \approx 4.5$ eV (considering a photon energy of 5.2 eV), which is smaller than the expected 4.9 eV reported in literature [220]. This hints to contamination of the Ni surface with adsorbates, presumably CO [221]. In fact, we observe a change in the yield- versus-energy curve during the first few hours after deposition. After 24 h though, the yield and asymmetry are constant for months, making it a very stable system. In return, these adsorbates influence the magnetization at the surface by changing the position of SRT to lower thicknesses [210, 222]. The energy-resolved MCD asymmetries are shown as grey dots in Figure 4.8, with a polynomial fit in blue retracing the general correlation. Additionally, some MCD PEEM images represented by these dots are shown at the top. Already at $E_B = 0$ eV, the magnetic contrast starts to emerge.

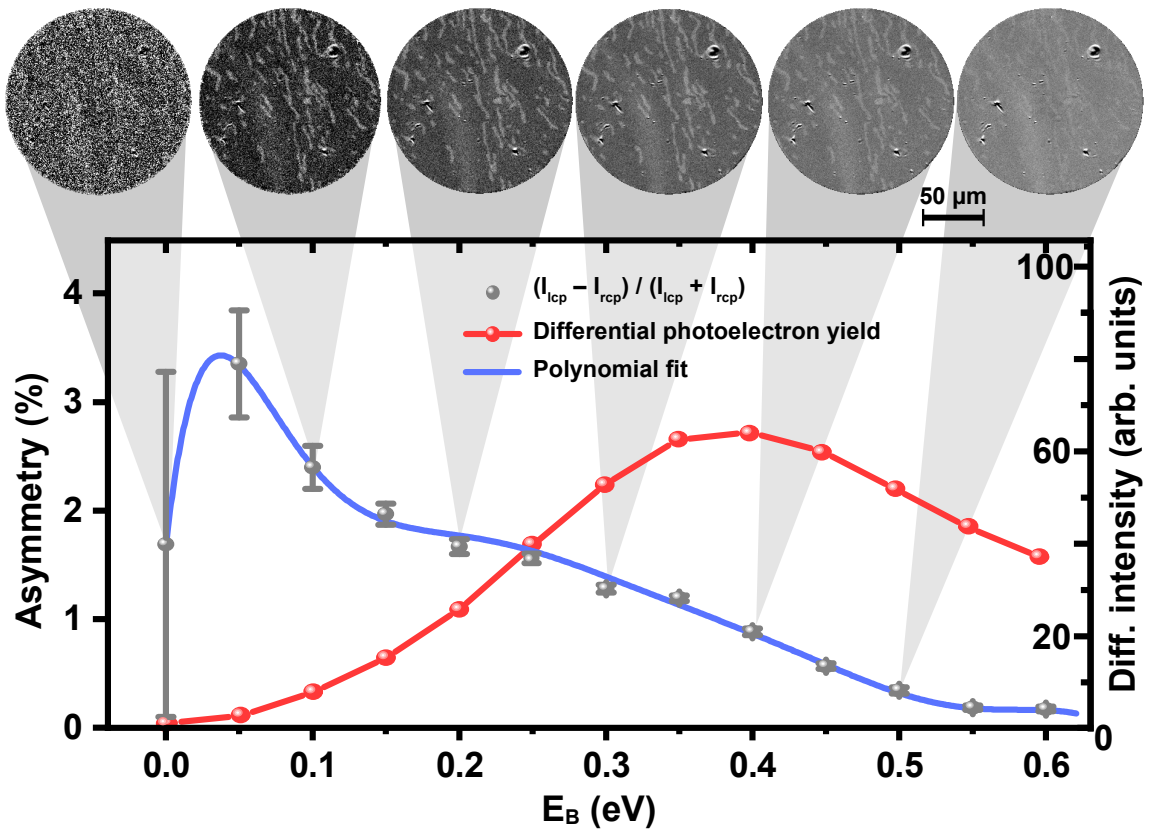


Figure 4.8: Plot of the differential photoelectron yield (red) and the asymmetry (blue) versus the energy cut-off of the high-pass filter. MCD PEEM images corresponding to the marked data points are shown at the top, revealing a stripe domain pattern with high contrast near the Fermi level, which vanishes with increased E_B .

In theory, the highest asymmetry for Ni is detectable directly at the threshold, due to the large stoner splitting caused by exchange, the high spin polarization caused by SOC and the low broadening of the energy distribution caused by secondary electrons. However, the total photoelectron yield at the threshold is very small, hence the high uncertainty. Therefore, we find the best figure of merit ($I \cdot A^2$) at $E_B = 0.2 - 0.3$ eV. At $E_B > 0.5$ eV, the secondary electron background becomes so dominant that the magnetic contrast disappears. Consequently, we are not able to detect any magnetic contrast without appropriate energy filtering or tunable photon energy.

One advantage of this technique over others such as MOKE is its superior resolution. This is demonstrated in Figure 4.9 for a 12 ML Ni film on Cu(100). At this thickness, the MCD PEEM images reveal a typical stripe domain phase, with stripe widths of 2-5 μm , which varies drastically with the film thickness (see next subsection 4.4.1). Such a structure is particularly well-suited for the determination of

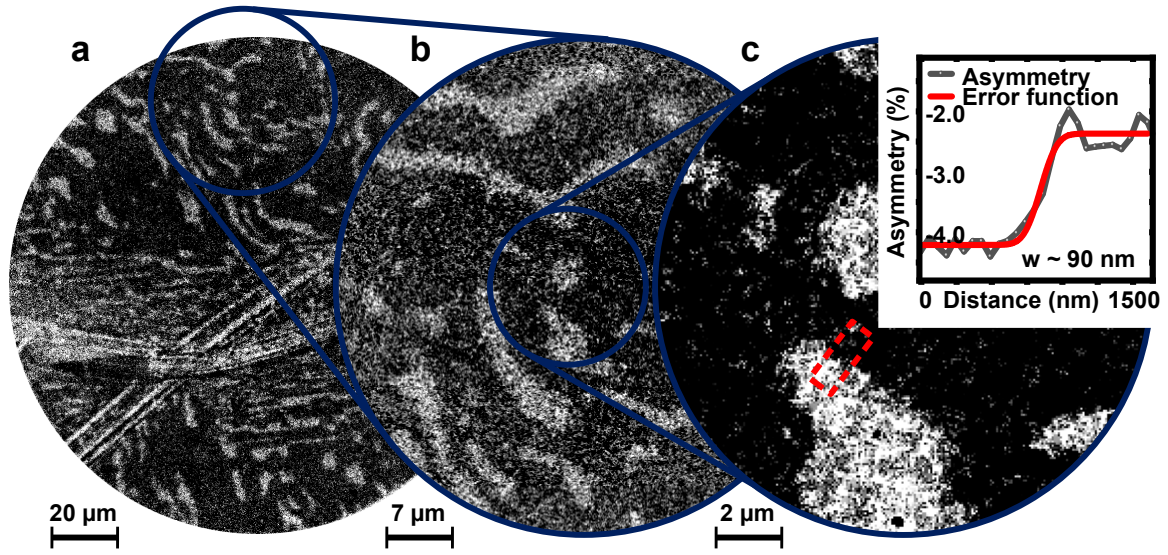


Figure 4.9: (a) MCD PEEM image showing magnetic domains of 12 ML Ni on Cu(100). (b) and (c) are close-up images of the marked areas. From the cross section marked by the red dashed box in (c), a magnetic domain wall width of about 90 nm is extracted by the fit in the inset.

the *magnetic* resolution limit in threshold PEEM and is used in the following. Hence, in Figure 4.9 we continuously decrease the FoV from (a) to (c), whereupon magnetic information is revealed below the resolution limit of MOKE. This is proven by measuring across a domain wall in Figure 4.9(c) and fitting equation 2.8 to the cross-section profile marked by the red dashed box. We determine an upper boundary of 90 nm for the domain wall width. Up to now, we cannot finally conclude, whether this is the ultimate resolution limit for magnetic *oop* contrast or the intrinsic width of the domain wall itself. Although, comparison to literature data hints towards the resolution limit, since widths below 90 nm have been reported in transmission electron microscopy experiments [223]. The domain wall width can be estimated by the exchange stiffness A and the anisotropy constant K . According to Lilley, the definition of the domain wall width δ in nm is as follows [224]:

$$\delta = \pi \sqrt{\frac{A}{K}} . \quad (4.9)$$

A is often approximated with $1 \cdot 10^{-11} \frac{\text{J}}{\text{m}}$, although it is slightly decreased in the case of Ni [225, 226]. Again, K depends highly on the distortion of the lattice, which results in a mismatch and, therefore, a thickness-dependent anisotropy. Values of $0 < K_v < 500 \mu\text{eV}/\text{atom}$ are reported in literature [227], which gives an approximate domain wall width of $(70 \pm 30) \text{ nm}$ [226].

With this, very small stripe domains or even skyrmion-like domain bubbles can be

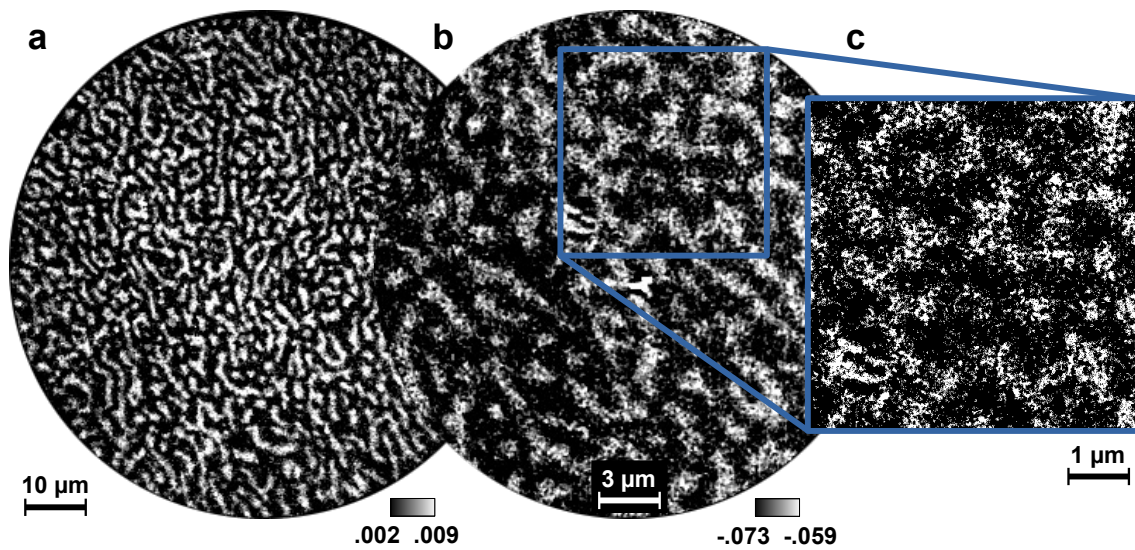


Figure 4.10: (a) CD PEEM image of a 12 ML thick Ni film on a Cu(100) substrate. (b) & (c) Zoomed-in areas marked respectively, reaching down to an FoV of only 5.5 μm in (c) revealing a granular fine structure within the *oop* domains.

investigated [181, 228]. An example for such a phase including magnetic structures smaller than 1 μm is shown in Figure 4.10. In this series of MCD PEEM measurements, the FoV is decreased stepwise from 85 μm to 5.5 μm , revealing an average domain width below 1 μm . Besides these small domains, the highest magnification in Figure 4.10(c) shows an additional granular fine structure within these domains. This fine structure could stem from even smaller *oop* bubbles within a domain, which are already known to appear in this material from MFM measurements [229]. These examples demonstrate the advantage over MOKE in terms of the resolution limit.

Domain size and film thickness

We started the investigation of Ni wedges expecting a transition from *oop* to *ip* domains with decreasing domain size when approaching the SRT, similar to wedge experiments of Fe/Ni layers [181, 228]. In fact, in some of the thin film samples with constant height and thicknesses close to the SRT, we observed a stripe domain phase, as shown previously. But, for high-quality wedges grown with a shadow plate, we observe the opposite. Figure 4.11 shows a series of MCD PEEM images mapping the wedge by shifting the sample along the slope of the wedge in steps of $\approx 500 \mu\text{m}$. The wedge positions are characterized by geometric calculations as well as XPS measurements at different thicknesses. However, since the detection spot size of XPS is at least 1 mm, both methods give only very approximate hints of the exact thickness at a given position.

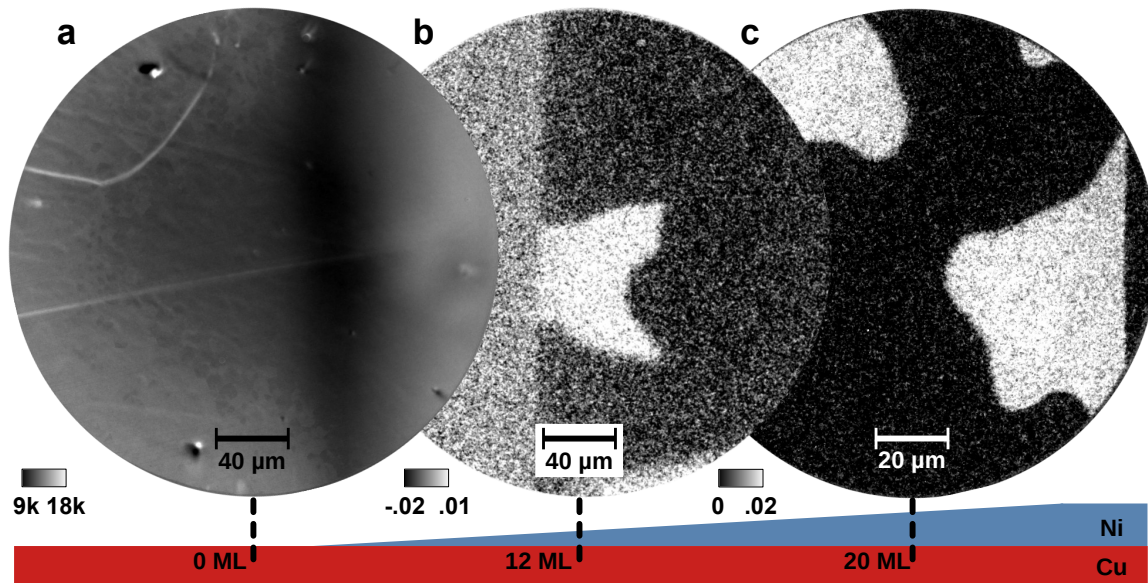


Figure 4.11: (a) Background corrected PEEM image of the Ni(100) wedge on Cu(100) at the transition from the bare Cu substrate to the Ni film, apparent by the bright horizontal scratch vanishing from left to right. (b) CD PEEM image of the same wedge at ≈ 12 ML, with a sharp transition in the asymmetry contrast. (c) CD PEEM image at ≈ 20 ML. At the bottom, the approximate measurement position on the wedge is schematically shown.

In Figure 4.11(a), a standard PEEM image shows the work function contrast of the transition between the bare Cu substrate (left) and the Ni film (right). Here, the onset of the Ni film is apparent by the vanishing contrast of the scratches and defects on the Cu substrate. In the MCD PEEM image in Figure 4.11(b), a sharp transition from grey to black-and-white marks the SRT, located at ≈ 12 ML. Veering away from the SRT actually decreases the domain size, as depicted in Figure 4.11(c), where the number of bright domains per area increases. In general, we observe irregularly shaped domains and no stripe patterns.

Similar to the thin-film samples, the asymmetry images of the wedge reveal a quasi single-domain state, i.e. areas of constant asymmetry, after annealing it above the Curie temperature. This hints to a dependence of the observed domain size to the film quality and structural order. Normally, surface defects result in a random configuration of up and down domains during layer growth, minimizing the magnetostatic energy. After annealing above T_C and subsequent cooling to RT, the system finds a new equilibrium, and the increased structural order corresponds to larger magnetic domains. Reports on this dependence are somewhat indecisive, ranging from continuously smaller stripe domains when approaching the SRT [230], to a drastic increase in stripe domain size [231], to larger irregular patterns [229], to smaller patterns [232]. Whilst the contribution of the crystalline anisotropy caused by the tetragonal distortion is the dominant factor for the overall change from *ip*

to *oop* domains, the actual domain structure and size seems to be only marginally influenced by film thickness. Especially for polycrystalline Ni films, the domain structure and size is more dependent on strain, substrate surface roughness, and applied and remanent magnetic fields during growth.

In case of thin films, the problem of predicting the domain size is caused by the very small energy differences between different domain configurations like irregular or stripe patterns [233]. Theory predicts an increase of domain size when the film thickness approaches the SRT [231, 234]. Hence, in our experiment, very small thickness differences of a few ML do not drastically change the domain size, since we already measure near the SRT. This is supported by the observed quasi single-domain state after annealing the film. To observe a clear thickness dependence, we will increase the slope of the wedge in an upcoming experiment, since the increased thickness gradient should result in a sharper domain-size gradient easier to observe in PEEM.

Binding-energy-dependent asymmetry

The theoretical considerations in Section 4.2.4 predicted the general existence of MCD in ferromagnetic Ni, which we experimentally verified in the last section. For a quantitative discussion, we now include band structure considerations based on published data for Ni [199, 206, 235] as well as relativistic calculations using the OMNI package (see Appendix B). Both rely on a fully relativistic one-step layer-KKR photoemission model [236].

These allow to estimate the binding-energy-dependent asymmetry in a given system. The general trend for $3d$ transition metals is shown in Figure 4.12(a). Here, we assume a highly symmetric case of Ni, $T = 0$ K and perfectly polarized light. The important d bands are marked at the bottom by the Schönflies notation as $\Delta_6^5+/-$ and $\Delta_7^5+/-$. This band splitting is the result of the exchange interaction and SOC, marked by Δ_{EX} and Δ_{SO} , respectively. These interactions lower the symmetry of the system, reducing the number of irreducible representations. Again, the + and - do not exclusively stand for majority or minority bands, since the spin is not a good quantum number in presence of SOC, which means that the spin-character of a band changes along k . By probing the system with s_L parallel to M , with s_L being the SAM vector of the incoming light, only Δ_6^5- and Δ_7^5+ bands contribute to the photoemission current according to relativistic dipole selection rules, which is shown by the solid vertical lines in Figure 4.12(a). For s_L antiparallel to M , only Δ_6^5+ and Δ_7^5- contribute (dashed lines), which results in the asymmetry shown at the top of Figure 4.12(a) when applying equation 2.9. Now, the relativistic band structure of Ni(100) in the Γ -X direction is considered in Figure 4.12(b). The bands contributing

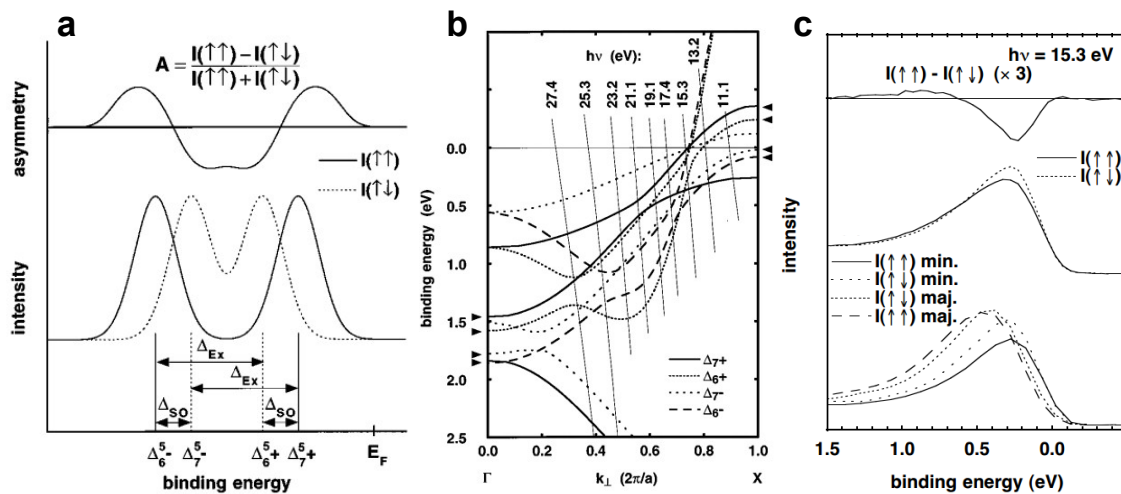


Figure 4.12: (a) Expected general shape of the asymmetry signal versus binding energy for a 3d transition metal in case of total symmetric configuration. The bands in the (100) direction which are important for near-threshold photoemission are marked at the x-axis. The effects of spin-orbit (Δ_{SO}) and exchange (Δ_{Ex}) splitting are marked accordingly. The solid and dotted lines show the parallel and antiparallel orientation of magnetization and light polarization, respectively [235]. (b) Band structure of bulk Ni(100) in Γ -X direction. The dotted lines mark the probed bands for the respective photon energy [206]. (c) Same graph as in (a) with actual experimental data from (b), with the contribution of the light helicities in the middle and the resulting difference of the two signals at the top [49].

to the asymmetry in (a) are flagged by black arrows on both sides of the graph. Additionally, the impact of the given photon energy is illustrated. The probed bands are marked by the crossing point of the initial-state band and the final-state band of Δ_6^1 symmetry shifted downwards by the respective photon energy (solid, vertical lines). Therefore, the chosen excitation energy is important, since it determines the final state of the photoemission process. We see that smaller excitation energies shift these crossing points closer to the X-point, where we observe an occupation of the lower exchange-split bands only. This impacts the actually calculated asymmetry, which is shown at the top of Figure 4.12(c) at 15.3 eV. Here, only the first peak of the general shape predicted in (a) is present, after which the asymmetry reduces, inverts at $E_B \approx 0.6$ eV and vanishes within 1.5 eV below E_F .

Since our photon energy is significantly smaller, we expect the crossing point to shift even closer to or beyond the X-point, which should result in a sharp asymmetry peak close to the threshold and an inverted contrast between $0 < E_B < 0.5$ eV. This is the result of a dispersion of the first asymmetry peak, which consequently shifts the point of inverted contrast closer to E_F for smaller photon energies.

We probe the binding-energy-dependent asymmetry with our MCD setup utilizing the IEF. Figure 4.13(a) shows an MCD near-threshold PEEM image of a nominally 12 ML Ni film on Cu(001) in the stripe-/bubble-domain phase at $E_B = 0.3$ eV. An energy scan performed at maximum energy resolution is shown in panel (b). Red and blue solid lines represent the smoothed, integrated asymmetry versus energy data for the bright and dark domains. These domains are marked by corresponding boxes in (a). Subtracting one from the other leaves the total integrated contrast of the picture shown in grey. The black solid line shows the differential contribution per binding-energy range, which is equivalent to the theoretical asymmetry values of Figure 4.12. The contrast inverts at $E_B = (0.32 \pm 0.03)$ eV, which is in line with our previous assessment obtained from comparisons to literature band-structure calculations [237]. Furthermore, the total asymmetry values are lower and the peak is broadened. Naturally, these comparisons need a careful interpretation, since our experiment does not fulfill all preconditions of the calculations. First, the Ni film is polycrystalline. Second, the experiment is not operated at 0 K. Third, the circular polarization is not perfectly preserved. Fourth, the angle of incidence is not perfectly symmetric, neither in oblique nor normal incidence. These differences cause a reduction of the maximum detected asymmetry in our experiments, varying from 1-4 % depending on surface quality and polarization stability. Other groups reported up to 12 % in spectroscopy experiments [155, 238] and theory predicts even higher values of 20 % for small excitation energies [235]. And fifth, the final state in our experiment is different from the one shown in the calculations, since our excitation energy is even lower. Hence, we probe a slightly different area of the band structure.

Despite these limitations, our setup proves to give viable experimental data comparable to already existing measurements and theoretical calculations in the literature. We expand on binding-energy-dependent measurements, by choosing even lower excitation energies, and the observed characteristics are in line with theory.

4.4.2 In-plane domains of Fe(001)

Inspired by the pioneering experiments of Marx *et al.* [171, 172], we use threshold PEEM for the investigation of the Fe(100) surface. Similar to Ni, no reduction of the surface work function is necessary. The experiment is designed considering the group theory ansatz explained in Section 4.2.4. We use the clean Fe(001) single crystal shown in Section 4.3 rather than a polycrystalline thin film. By realizing the two setups shown in Figure 4.14, these symmetry considerations help to maximize the asymmetry, i.e. the ferromagnetic contrast. Whilst the configuration in (b) with

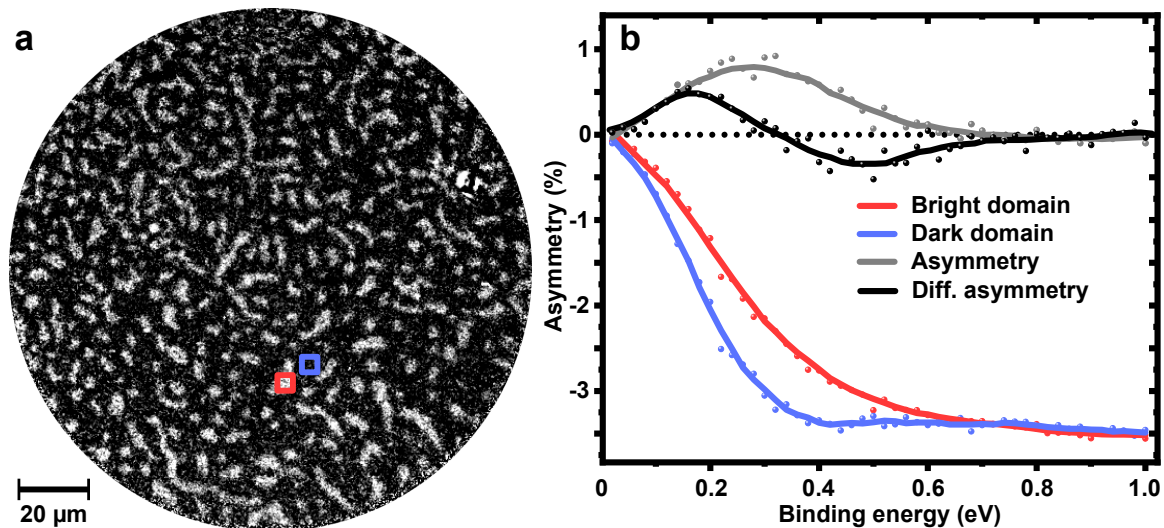


Figure 4.13: (a) CD PEEM image of a 12 ML Ni(100) film. (b) Plot of the asymmetry values of a domain appearing bright and dark (marked in (a)), with the gray values at the top showing the difference between the two. The black line/dots mark the differential asymmetry signal calculated from the grey data with an energy window of 0.1 eV. Dots and lines show raw and smoothed data, respectively.

light incident in a low-symmetry direction should result in a different asymmetry value for every magnetization direction, the rotated configuration in panel (c) should cause a contrast between the collinear, opposite ip magnetization directions, when M is parallel to the ip component of q . The first is the standard geometry when measuring MCD with the Hg lamp in the Femto-PEEM chamber, the latter resembles the situation after rotating the crystal by 60° with respect to the horizontal direction of the sample holder. This way, the [001] direction is parallel to the incidence plane. The MFM measurements in Figure 4.5 revealed the orientation of the ip domains along the high-symmetry [001] directions due to the crystalline bulk anisotropy. Hence, the symmetry considerations from Figure 4.2 apply. The off-angle configuration of Figure 4.14(b) reduces the symmetry for oblique incidence, but should theoretically cause MCD, too. Furthermore, all four available ip magnetization directions should be distinguishable in this configuration, since the projection of M on the incidence plane is different for all possible easy axes. However, the MCD might be too small to allow for this differentiation. Thereby, Figure 4.14(c) shows the high-symmetry case, where it should be possible to distinguish between the two collinear magnetization directions, but not between the two perpendicular ones.

Figure 4.15 shows the experimental comparison of the two setups. In panel (a), a standard PEEM image shows the known morphology discussed in Figure 4.5. At the same position, we performed MCD PEEM measurements on the unrotated and aligned crystal, as shown in Figure 4.15(b) and (c), respectively. Whilst the off-angle setup results in no measurable asymmetry, the setup shown in Figure 4.14(c) reveals

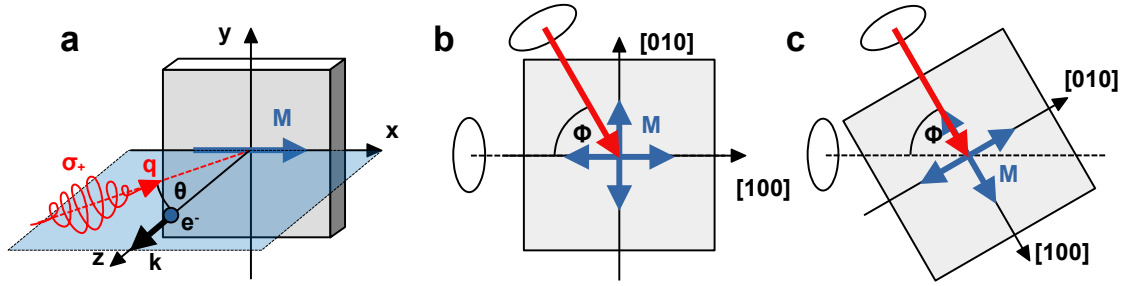


Figure 4.14: (a) Isometric schematic of the experimental setup. (b) Actual top-view on the sample when measured in the Femto-PEEM chamber via the Hg lamp. (c) Same configuration with the crystal rotated by 60° , aligning the incidence plane with the $[100]$ direction.

large ip domains. These are apparent by different gray levels shown in the inset of the cross section in Figure 4.15(c).

The largest contrast between anti-parallel ip domains collinear to the incidence plane is $\approx 1.5\%$.

This measurement proves that the theoretical predictions considered above are correct. It is important to point out the differences between previous measurements in literature and our approach presented here. The improved asymmetry contrast is the result of the optimized excitation geometry according to the group theory ansatz as well as the high quality of the single crystal and its surface preparation.

Another intricate detail of the MCD image in Figure 4.15(c) is the fact that the grey level of the perpendicular domains is not homogenous. The inhomogeneity is also apparent by the shift towards higher asymmetry values of the mid-level area of the cross section data shown in the inset. This is the result of the rotation of the crystal, which was checked via LEED. The alignment of the diffraction spots revealed $\phi = 70^\circ \pm 5^\circ$, which is significantly off from the intended $\phi = 60^\circ$. Hence, opposite magnetic domains in the $[010]$ direction result in slightly different MCD. However, this should cause an even larger maximum asymmetry contrast once q and M are aligned properly.

Figure 4.16(a) now shows near-threshold MCD PEEM images of the same crystal with the excitation angle and polarization vectors properly aligned. The presumed ip directions are marked accordingly. The domain wall orientation of 90° walls is always along the crystal's high-symmetry direction or in the $[110]$ direction, with an observable prevalence for the latter. Due to the proper alignment, only one grey value is observed for the magnetization in perpendicular direction. Since MCD PEEM is highly surface sensitive, we expect to only measure the Néel-type walls at the surface. The domain wall width of ≈ 200 nm observed in MFM is also within our magnetic resolution limit as shown in Figure 4.9. Figure 4.16(b) shows an MCD PEEM

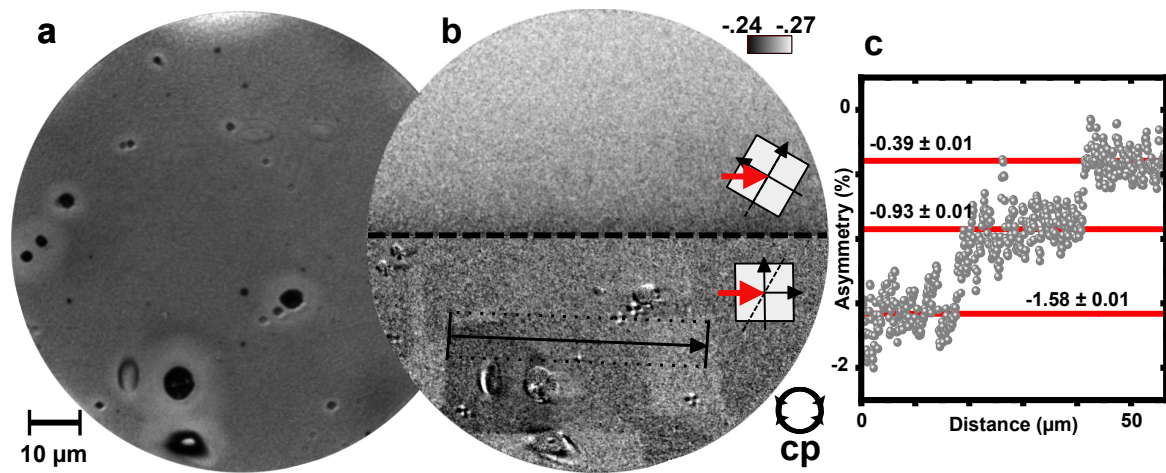


Figure 4.15: (a) Standard PEEM image of an Fe(001) single crystal surface with configuration shown in Figure 4.14(c). (b) MCD PEEM image with the off-angle setup described in Figure 4.14(b) at the top revealing no measurable asymmetry. At the bottom, an MCD PEEM image of the high-symmetry configuration described in Figure 4.14(c) is shown, revealing large *ip* magnetic domains with clear domain walls along the crystals high-symmetry directions. (c) Cross section data of the line scan marked by the black arrow in panel (b). The asymmetry levels for different domains are fitted by red solid lines.

image with decreased FoV, at which different types of Néel-wall rotations should be distinguishable. However, we could not detect a difference between different domain walls in threshold PEEM. The overall surface quality might already be too low after several hours long acquisition times needed for high-resolution measurements. Hence, at these surfaces, the magnetic resolution is too low for the investigation of the rotation within the domain wall itself. For high-resolution experiments, stable, oxygen-saturated Fe(001)-(1x1)-O surfaces might be better suited.

Contrarily to our previous investigation of Ni thin films, the measured asymmetry is almost constant over a large E_B range close to the threshold. Figure 4.17 shows the asymmetry difference between bright and dark domains in the range from 0.1 to 1 eV below E_F , as well as the scan of the differential photoelectron yield as a function of binding energy. The latter increases from 0 eV to its maximum at 0.6 eV and drops to zero at 1 eV. From this, we determine a surface work function of $W \approx 4.2$ eV, which is lower than the expected 4.64 eV for a clean Fe(001) surface [239, 240]. This is probably caused by oxygen adsorption of the highly reactive surface [241, 242]. Compared to the *oop* domains on the Ni surface shown in Figure 4.13, the asymmetry increases rapidly within the first 0.2 eV, after which it stays almost constant. It slightly decreases from 1.5% to 1.1%, with the best figure of merit at $E_B \approx 0.6$ eV. We want to stress the difference to the Ni thin-film data in Figure 4.8, where the asymmetry vanishes within 0.6 eV, rendering a magnetic contrast without an energy filter impossible. This difference is either a direct result of the difference in the

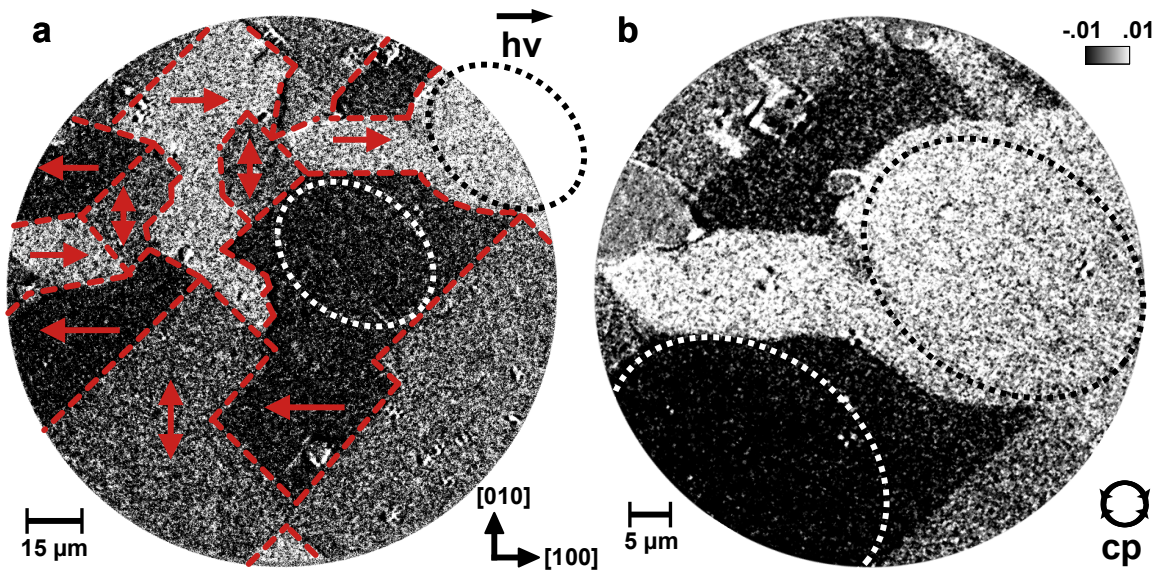


Figure 4.16: (a) MCD PEEM image of an Fe(001) single crystal at $E_B = 0.7$ eV, with the different M of each ip domain marked by red arrows and the domain walls marked by dashed lines. (b) MCD PEEM image of the same area but decreased FoV. The dotted circles mark the area of the dark and bright domain used for the k-space images in Figure 4.18 and 4.19.

Fe(001) band structure or a consequence of the bulk layers. Electrons with higher E_B /lower E_{kin} stem from deeper layers, which are equally magnetized in the case of Fe. Contrary, in Ni thin films, surface and interface effects play a crucial role, whereupon the secondary-electron background buries the MCD contrast.

Band-structure measurements and discussion

The large domains and high surface quality allow for MCD k-space imaging at areas with opposite M . Regarding the intensity in Figure 4.16, we refer to these as dark and bright domains. We use a real space FoV of $\approx 80 \mu\text{m}$ and close the field aperture until predominantly only one domain is visible. Afterwards, we switch to k-space mode and perform energy scans utilizing the IEF. An exemplary measurement on a dark domain is shown in Figure 4.18. Here, background-corrected, differential k-space images for $E_B = 0.1$ and 0.3 eV are compared for lcp and rcp excitation, respectively. Additionally, we compared our measurements with the expected k-space images from OMNI calculations tailored to our specific experimental setup (see Appendix B for details). These theoretical results are shown in Figure 4.18 below every experimental dataset. At 0.1 eV, the difference image resembles a windmill shape with lobes in the $[110]$ directions, similar to typical depictions of a d_{xy} orbital. Interestingly, the asymmetry along the lobes inverts between 0.2 and 0.3 eV, after which it continuously drops to zero at 0.7 eV (not shown in Figure 4.18). These

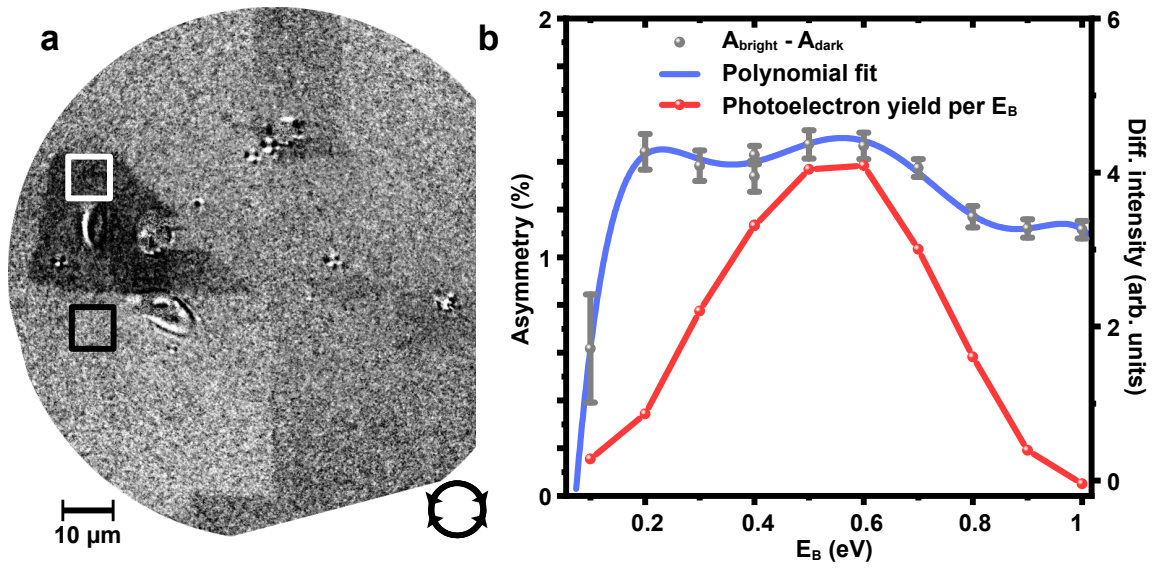


Figure 4.17: (a) MCD PEEM image of an Fe(001) crystal surface at 0.4 eV. (b) Plot of the asymmetry difference of a bright and dark domain (black and white squares in (a), respectively) with respect to the binding energy E_B (grey dots, with a polynomial fit of the data as a solid blue line). The differential photoelectron yield per binding energy is shown in red, which represents the contribution at each energy window from the total photoelectron yield.

characteristics are all qualitatively confirmed by our calculations. The qualitative agreement between measurements and theoretical calculations is also apparent when looking at the intensity in the k-space PEEM images directly at the $\bar{\Gamma}$ point. There, the intensity is almost zero for $E_B = 0.1$ eV. On the contrary, at $E_B = 0.3$ eV the intensity maximum is located at $\bar{\Gamma}$.

Additionally, the k-dependent asymmetry reveals that the k-integrated asymmetry is much lower than the k-resolved maximum. In the previous section, we report a real-space asymmetry of $\approx 1.5\%$, whilst the maximum asymmetry in k space is $\approx 13\%$ in the [110] direction. This is shown by the off-center, vertical cross sections marked on the right in Figure 4.18. At the $\bar{\Gamma}$ point, the trend of the photoelectron yield as a function of the binding energy is similar to the averaged signal in Figure 4.17. Therefore, the examples in Figure 4.18 nicely illustrate the non-trivial experimental effort to access high-asymmetry regions in the energy-momentum phase space, if only conventional ARPES setups along one high-symmetry momentum direction would be applied.

The spatial proximity of different magnetic domains allows for a direct comparison between dichroism caused by helicity switching and dichroism caused by switching of the magnetization direction. We refer to the nomenclature of Henk *et al.*, which is derived from spin-polarized LEED experiments, coining these polarization asymmetry (A_{pol}), magnetization asymmetry (A_{mag}), and its residual part,

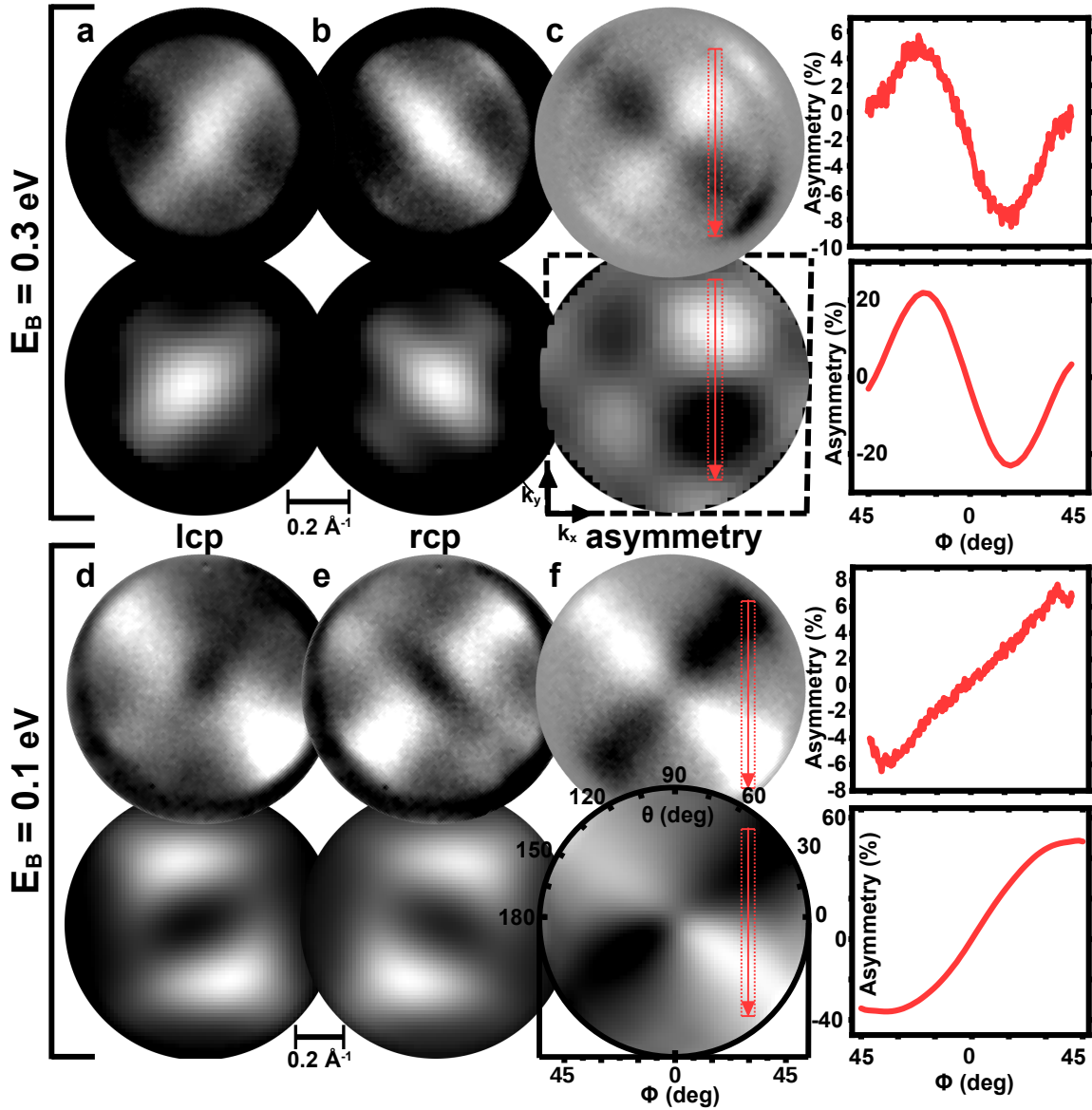


Figure 4.18: Comparison between background-corrected, differential k-space PEEM images of the dark domain marked in Figure 4.16 (first and third row) and corresponding OMNI calculations (second and fourth row). On the left, the respective binding energy is shown. The PEEM images are arranged in three columns, showing images for *lcp*, *rcp* and the resulting asymmetry, from left to right. An area is marked in the asymmetry images, and the corresponding cross section is plotted on the right.

the exchange asymmetry A_{ex}) [207, 243]. This analysis provides interesting insights into the peculiarities of threshold PEEM in general, as well as the specific iron $3d$ bands. In both theory and experiment, we now have access to the full set of possible orientations ($\pm s_L$ and $\pm M$). Hence, we can deconvolute the *intrinsic* contribution to the asymmetry caused by spin-orbit interaction and the *magnetic* contribution caused by exchange interaction.

In Figure 4.19, we compare different k-space asymmetry images at $E_B = 0.1$ eV.

Whilst panel (a)-(c) show asymmetry images when switching between *lcp* and *rcp*, panel (d)-(f) show asymmetry images when switching between a dark and bright domain, i.e. $-M$ and $+M$, respectively. We refer to these two experimentally distinctly different asymmetries as A_{pol} and A_{mag} . Comparing A_{pol} images in (a) and (b) on a dark and bright domain, respectively, reveals a very similar momentum pattern with comparable asymmetry values as shown in Figure 4.18. Figure 4.19(c) is the difference between (a) and (b), showing a characteristic asymmetry of about 4.5 % that is centered at the $\bar{\Gamma}$ -point and oriented in the [100] direction. Although the asymmetry k-space images on both domains look very similar with the naked eye, there is a clear shift of the signals in the [100] direction. This is the contribution of the exchange interaction, i.e. A_{ex} . Again, all theoretical calculations shown below each measurement resemble the experimental data nicely.

Interestingly, the images in Figure 4.19(d) and (e) depicting A_{mag} look completely different compared to the A_{pol} -images in (a) and (b). The magnetic asymmetry for *lcp* light resembles the difference image in panel (c), with an asymmetry contrast centered at the $\bar{\Gamma}$ -point in the [100] direction. But, the center of inversion is shifted when comparing panel (d) and (e), i.e. *lcp* and *rcp* light, and the line connecting the points of maximum asymmetry is tilted with respect to the [100] direction. The corresponding calculations emphasize these specifics in more detail. Here, the tilt of the handles is clearly apparent. Comparing the intensities in Figure 4.19(d) and (e) reveals an inversion of the contrast, i.e. the sign of the asymmetry values is flipped. When calculating the difference in (f), the same pattern as in panel (c) emerges, signifying again the exchange contribution.

In Figures 4.18 and 4.19, extremely large asymmetry values are present in both the calculations and measurements, when considering off-axis configurations. According to our calculations, the asymmetries can exceed 50 % in some specific cases, which we do not observe in our experiment. In the cross section at $E_{\text{B}} = 0.1$ eV in Figure 4.18, a polarization asymmetry of 15 % is found, whilst the largest exchange anisotropy is 6 %. In all measurements, the observed asymmetries are always lower than the calculated ones by a factor of 2 to 6. The limitations of calculations are briefly discussed in Section 4.4.1 and Appendix B.

In order to rule out the possibility that the observed asymmetry patterns are caused by our setup, we perform multiple measurements at different domains with different configurations of the wave plates. We also measure several energy scans similar to Figure 4.18. Indeed, we always see the same sign flip of the contrast at 0.2-0.3 eV in the images shown in Figure 4.18(c) and (f). Hence, considering the apparent agreement with our theoretical calculations, we conclude that the observed k-space contrast in the magnetic and the exchange asymmetry are both of ferromagnetic

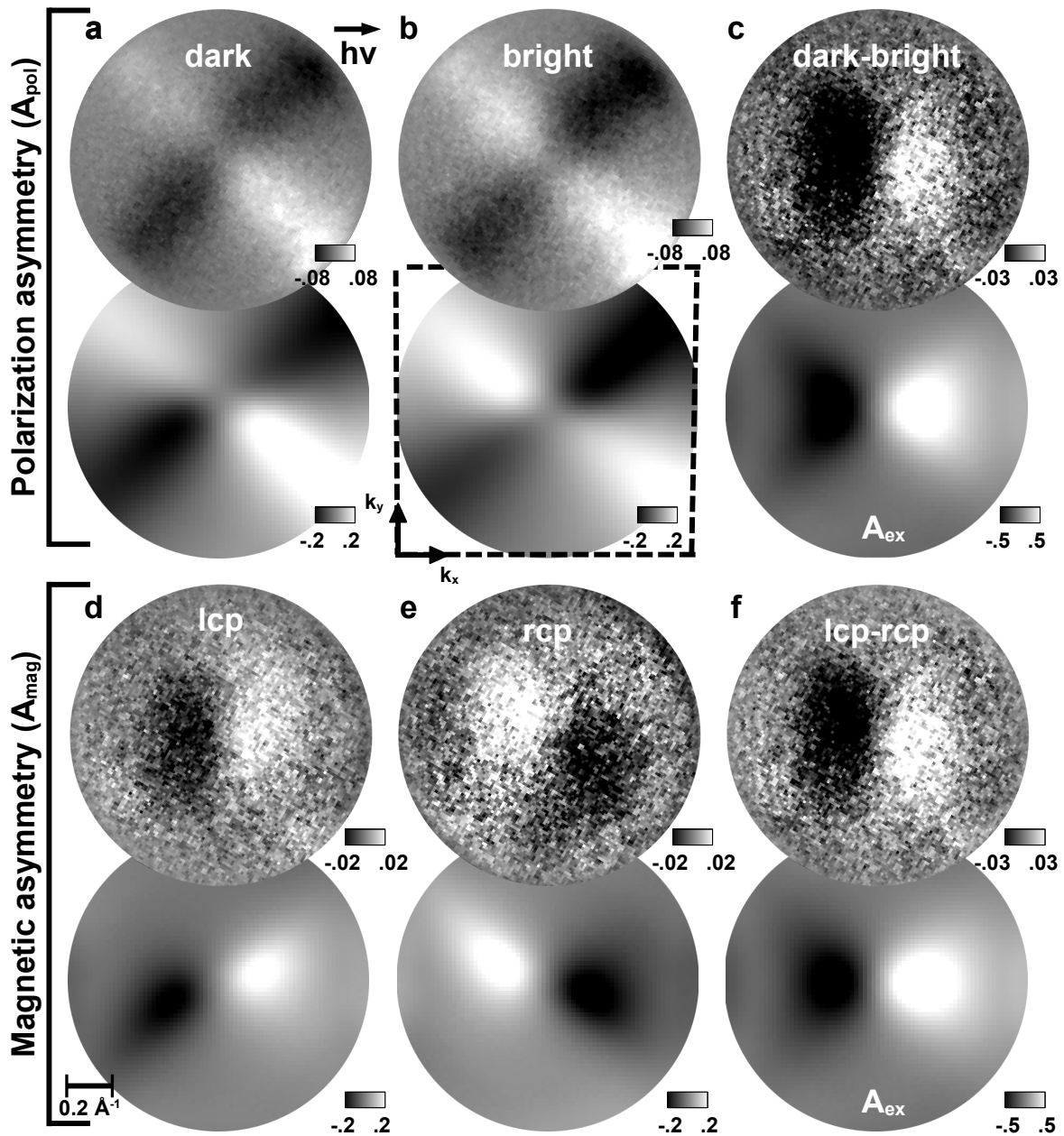


Figure 4.19: Comparison between asymmetry k-space PEEM measurements (first and third row) at $E_B = 0.1$ eV and corresponding OMNI calculations (second and fourth row). On the left, the kind of asymmetry is specified. *Polarization asymmetry* means switching between *lcp* and *rcp* light, either on a dark (first column) or bright (second column) domain, which are marked in Figure 4.16. *Magnetic asymmetry* means switching between the dark and bright domain ($\pm M$) and keeping the polarization constant (*lcp* and *rcp*, shown in first and second column, respectively). The third column on the right shows the difference between the asymmetry images in the first and second column, revealing the contribution of exchange interaction.

origin, i.e. a difference between the photoemission processes in the band structure of ferromagnetic domains.

The respective bulk band structure in [100] direction, i.e. from the $\bar{\Gamma}$ point to the \bar{H}

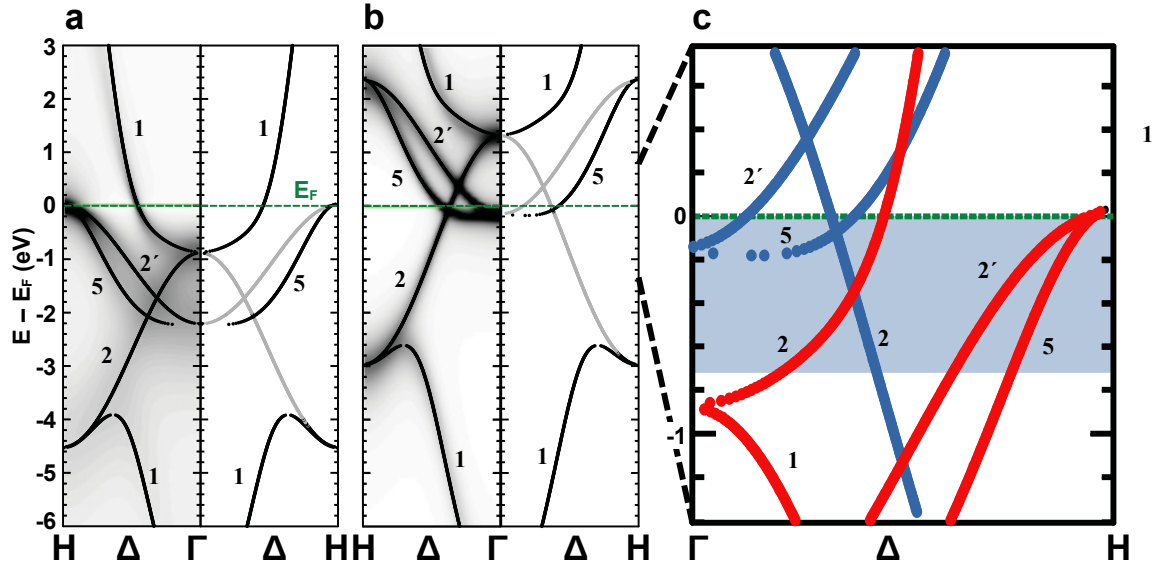


Figure 4.20: (a) & (b) Valence electron density of states (black-shaded background) of the majority and minority spins in Fe(001), respectively, along the Δ direction, with the corresponding bulk band structure overlaid as black-solid lines. The spatial symmetry of the individual bands is marked accordingly. On the right side of each graph, only the bands contributing to the photoemission yield according to dipole selection rules are marked. (c) Same band structure zoomed-in on the energy range probed by the experiment (blue-shaded area). Here, both spin states are shown together as red- (majority) and blue-solid (minority) points. All data taken from reference [244].

point along Δ , is depicted in Figure 4.20. The data are taken from the reference [244]. Here, the valence band structure for majority and minority spins is shown, and the spatial symmetry group of the respective band is marked accordingly. Directly below the Fermi level, minority spin states of Δ_5 symmetry dominate. For the first two layers, a portion of these states is shifted above the Fermi level, forming a prominent minority spin surface state [244–246]. This surface state is highly localized. Below 0.2 eV majority spin states of all symmetry types (Δ_1 , Δ_2 , Δ'_2 and Δ_5) are present. But, according to dipole selection rule [44, 45] only bands of Δ_1 and Δ_5 symmetry dominate photoemission. The transition from minority to majority character when crossing the Fermi level towards higher binding energies qualitatively fits the sign reversal in the magnetic and exchange asymmetry observed between 0.1 and 0.3 eV. To get a conclusive discussion, fully-relativistic band structure calculations for the [100], [010] and [110] direction will be performed in the future using the OMNI package.

4.5 Conclusion & Outlook

This chapter revealed the general capabilities of the new Femto-PEEM chamber in regard to measuring magnetic *ip* and *oop* domains on two different systems, namely Ni/Cu(001) and a Fe(001) single crystal. We designed these experiments to maximize the (magnetic) asymmetry in near-threshold PEEM by following the group theory ansatz based on relativistic layer-KKR photoemission theory. As a result, asymmetries of 4 % in Ni thin films and 1.5 % in Fe single crystals were observed in MCD PEEM in real space. Additionally, a resolution limit for magnetic domains of 90 nm was achieved. The data for the investigated Ni surface nicely fit the theory and literature values. We extended these proof-of-principle measurements to Fe(001), where we observe sizable asymmetries which are one to two orders-of-magnitude larger than previously reported for near-threshold PEEM. Energy scans in real space reveal an almost constant magnetic asymmetry over the full detectable energy range, whereas the *oop* asymmetry in Ni peaks very closely to the photoemission threshold, after which it quickly vanishes.

Furthermore, energy scans in k space revealed extremely large asymmetries above 10 % in off-axis configurations. With these k-space images, we managed to deconvolute the contributions of exchange and spin-orbit interaction to the observed dichroism. All experimental results are supported by our relativistic photoemission calculations as well as band structure data from the literature. The gathered knowledge of the system and the photoemission therein will now be used to increase the observed asymmetries in real space by placing a small contrast aperture in the back-focal plane where we observe the highest asymmetry in k space. Theoretically, this will drastically decrease the overall yield, but the magnetic asymmetry in real space will increase significantly.

Next, we will use these results to optimize the imaging process and expand beyond static imaging by preparing a first sample for testing the upcoming time-resolved laser measurements. In these future experiments, we will pump the surface from the back side and probe it from the front, hence reducing space charge effects and being able to investigate transport processes through the sample or intermediate layers. For this, we want to grow thin films and wedges of Fe on MgO(001). Preliminary experiments and results can be found in Appendix A.

Chapter 5

Antiferromagnetic Dichroism in PEEM

This chapter covers the investigation of NiO as an example for measuring antiferromagnetic domains via linear and circular dichroism in near-threshold PEEM. This topic will be introduced by a short literature review, after which results obtained from polished NiO(100) single crystals are presented and discussed. An outlook to upcoming experiments and calculations concludes the chapter.

5.1 Introduction

Antiferromagnets were one of the earliest material classes measured with static threshold and XPEEM [247, 248]. These materials exhibit an exceptionally high magnetic stability and ultrafast switching times, which is why they sparked the interest of the research community. A coherent and reliable optical control of the spin states of an antiferromagnet would be a huge leap for possible future information technology devices. In the following, we will focus on NiO as the drosophila of antiferromagnetic oxides.

NiO(100) is a so-called charge-transfer insulator. The d bands are split into an occupied lower Hubbard band and an unoccupied upper Hubbard band due to the strong electron-electron repulsion typical for correlated transition-metal oxides. NiO grows in a rock-salt structure with the Ni and O located at two fcc sublattices, as illustrated in Figure 5.1(a). Therefore, the two elements form alternating close-packed layers of purely Ni and O along the $\{111\}$ direction. Each Ni contributes a magnetic moment of $2 \mu_B$ forming ferromagnetic (111) planes. NiO is a collinear antiferromagnet, meaning these alternating ferromagnetic sublattices are oriented antiparallel to each other. For symmetry reasons, four different (111) planes are available. Thus, four different directions of the antiferromagnetic moment are distinguishable. These are the so-called T(twin)-domains. Within each individual plane, the respective spins can be aligned along three different easy axes, resulting in a total of 12 different S(spin-rotation)domains [249, 250]. The two different AF domain types are depicted

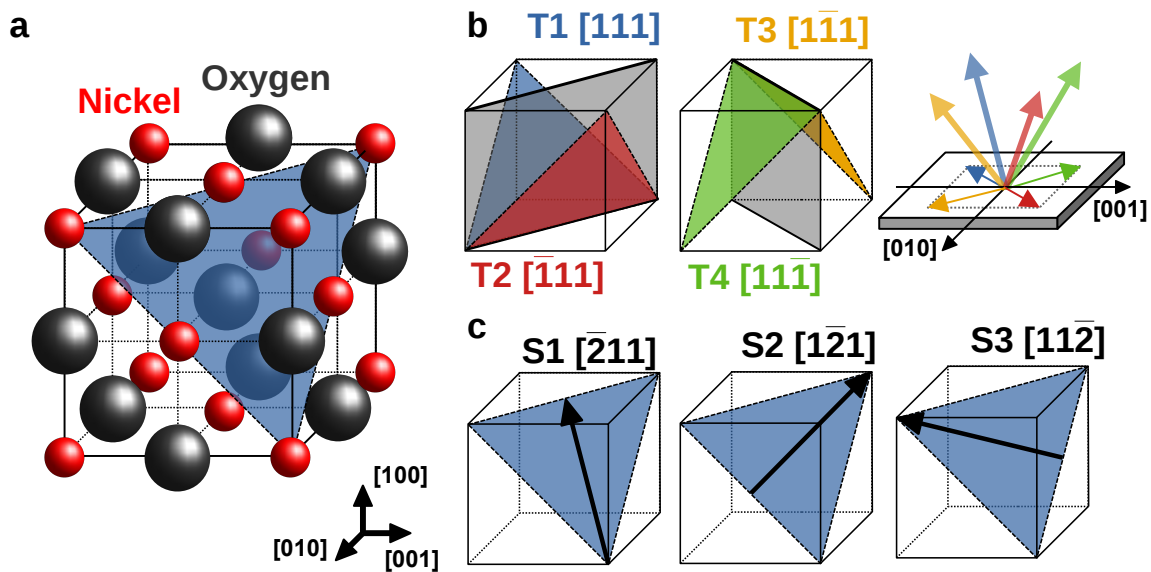


Figure 5.1: (a) Schematic of the NiO bulk crystal, with the ferromagnetic plane shown in light-blue, and the Ni and O atoms as red and black spheres, respectively. (b) Schematic revealing the four different T domains, depicted by differently coloured $[111]$ planes. The corresponding Néel vectors are projected onto the (100) surface plane. (c) Schematic showing the three possible spin orientation directions, i.e. S domains, of the T1 domain. There are three S domains per T domain, which gives 12 S domains in total [95].

in Figure 5.1(b) and (c), respectively. According to the group theory approach introduced in Section 4.2.4, MCD PEEM should be sensitive to the in-plane projection of the Néel vector when investigating the (100) surface. The fact that we consider an AF order does not change the underlying symmetry argument. Here, the projection of the T1 and T2 domains point perpendicular to the T3 and T4 domains, hence these should result in a different photoelectron yield. However, the added degrees of freedom due to the three S domains may prevent a sharp contrast to appear in MCD PEEM.

Whether or not it is possible to image the T or S domains via threshold PEEM has been discussed somewhat controversially in the literature in the early 2000s. Weber *et al.* were the first to report that they successfully imaged T domains via linear dichroism in UV PEEM using a mercury discharge lamp [251] and later even the respective T domain walls [252]. They switched between *s*- and *p*-polarized light, which left a linear dichroic asymmetry of 9% in the shape of a stripe pattern similar to patterns of T domains known from XMLD measurements [250]. However, in 2007, van Veghel *et al.* tried to reproduce these results and found no linear dichroic asymmetry stemming from the AF domains [253]. They alternatively propose that the contrast observed in LD PEEM is a result of oxygen deficiencies in the NiO surface structure and crystallographic distortions, which coincide with the AF domains. This has already been proposed in earlier XMLD measurements [254]. Additionally, their

model calculations predict an AF contrast smaller than 0.9%. They also heated the sample above the Néel temperature T_N , whereupon the observed contrast remained visible. After that, no attempts of imaging T or S domains via threshold PEEM have been published. Interestingly, none of these groups used the group theory ansatz to design their experiment to image the AF domains. They rather used an optical framework, where antiferromagnetic order is coupled to the crystallographic structure via magnetism-induced lattice contraction effects. This gives rise to a second harmonic generation signal, which is commonly used to image T domains in NiO via optical linear polarization microscopy [255, 256]. Although these lattice effects have been thought to be detectable in near threshold PEEM, it is an inherently indirect way of detecting the AF order.

To circumvent the difficulties arising from imaging the clean NiO surface, many groups add ferromagnetic layers or wedges and investigate changes in the ferromagnetic domain structure caused by exchange bias [95, 257, 258]. Besides NiO, antiferromagnetic domains in multiferroic materials like LaFeO_3 , BiFeO_3 , $\text{La}_{0.7}\text{Sr}_{0.3}\text{MnO}_3$ and $\text{La}_{0.7}\text{Sr}_{0.3}\text{FeO}_3$ [259–263], as well as Mn_2Au [264] have been successfully measured via XMLD.

Going back to the group theory approach used for imaging ferromagnetic domains, the same logic applies: It should be possible to image AF T domains of NiO(100) surface via MLD and MCD in near-threshold PEEM, but it is difficult to distinguish the AF contribution to the asymmetry from structural and crystallographic effects. The estimates for this contribution are drastically different in literature, hence, no conclusive answer on how to directly image AF domains in near-threshold PEEM has emerged yet.

5.2 Experimental details

For the PEEM experiments, we use a polished NiO(100) single crystal. Its surface structure is different from cleaved NiO samples, which are also commonly used in the field. Cleaved samples benefit from small changes in the density of oxygen vacancies per terrace, but the average terrace width is small. The latter is strongly increased for polished samples. However, this comes at the cost of scratches resulting from the polishing process. When comparing PEEM measurements between publications, this difference has to be kept in mind.

The single crystal was annealed to 570 K for one hour. We refrained from sputtering the sample in order to preserve the surface morphology and prevent the

introduction of further oxygen vacancies [251, 253]. Since NiO is an insulator, a low concentration of oxygen vacancies promotes surface conductivity, which is a prerequisite for PEEM measurements. On the other hand, areas of high vacancy concentration introduce an additional work function contrast. However, these effects are independent of the P , which is why they should not cause an asymmetry contribution upon switching the polarization [253]. In our case, no sputtering was needed in order to increase the conductivity. Finally, a high surface quality was verified via LEED, which showed clear diffraction spots and no significant charging.

5.3 Results & Discussion

Reproducing the measurements from Weber *et al.*, Figure 5.2(a) and (b) show the background-corrected PEEM measurements for p and s -polarized light respectively. Again, the azimuthal angle $\Phi = 60^\circ$ is set with respect to the [100] direction, which is 15° off from the ideal parallel projection of the T domain Néel vector, as illustrated in Figure 5.1(b). For s -polarized light, the surface appears scratched, with sharp straight lines appearing in black or white and having different angles, which are distributed randomly. For p -polarized light, these scratches are not dominant, but broad patches of different photoelectron yields are visible. In all measurements, charging of the sample was not an issue, which indicates a high amount of oxygen vacancies at the surface. Hence, the contrast variations in Figure 5.2(b) may be related to work function differences induced by varying concentration of these oxygen vacancies, as they look very similar to the contrast observed by van Veghel *et al.* [253]. Due to the larger perpendicular polarization component for p -polarized light, deeper layers of the surface are probed, hence, the work function differences become dominant. In the case of s -polarized light, higher surface sensitivity increases the effect of crystallographic defects which are probably caused by the polishing process. Figure 5.2(c) shows the LD image obtained from calculating the asymmetry of figures (a) and (b) according to equation 2.10. Here, the large patches presumably caused by the oxygen vacancies vanish and only the sharp scratches remain. These seem to be predominantly oriented along crystallographic high symmetry directions and resemble the crystallographic defect structure often reported from XMLD measurements [254].

Counterintuitively, the measured photoelectron yield reduces when switching from s - to p -polarized light. Generally, the opposite is the case since the component of the polarization P perpendicular to the surface governs the photoelectron yield in case of oblique angle of incidence. The reason for this peculiar behavior becomes apparent when performing an energy scan as depicted in Figure 5.3(a). Here, the photoelectron yield per binding energy E_B is plotted for p - and s -polarized light in

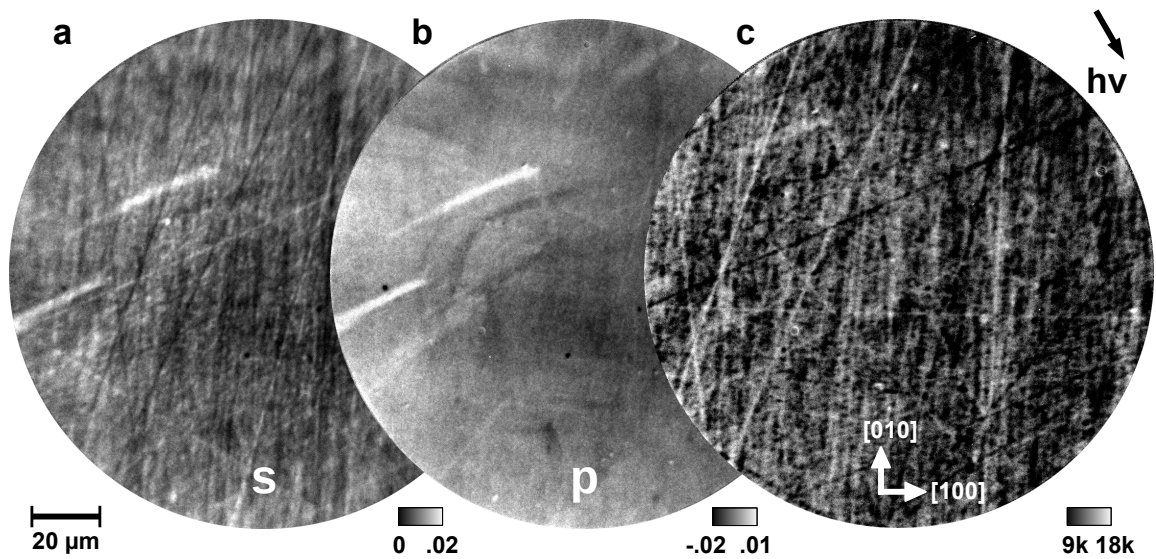


Figure 5.2: (a) & (b) PEEM images at 5.2 eV and the energy filter set to $E_B = 1.5$ eV with *s*- and *p*-polarized light, respectively. (c) LD PEEM image resulting from (a) and (b).

blue and green, respectively. As expected, the yield for *s*-polarized light is smaller than for *p*-polarized light, but the band is shifted towards higher E_B by ≈ 0.5 eV in the case of *p* polarization. Thus, the total yield is lower when performing an energy filtered PEEM measurement. This effect can also be seen in Figure 5.3(b), where the normalized total yield per E_B is plotted. Hence, we conclude that we detect a shift of the valence band in an energy-resolved photoemission experiment. This phenomenon is known from other photoemission experiments on insulators and semiconductors, which can be attributed to a band bending at the surface or an interface upon illumination with a high-intensity light source such as a mercury discharge lamp [265, 266].

In semiconductors, vacancies cause *p* or *n* doping. At the surface or the interface of such a doped material, the electron bands tend to bend up or down, which shifts the overall detected band position. The shift in apparent binding energy in our experiment can be attributed to such a band bending. In NiO, the abundance or deficit of oxygen in the surface layers work as an effective *n* or *p* doping, respectively. This shifts the valence and conduction bands either downwards or upwards. Upon intense illumination, this surface charge is screened, which flattens the band and shifts the apparent binding energies. This band bending and flattening effect is depicted schematically in Figure 5.4. Here, the band alignment at the surface for *n* doping with low and high illumination is shown in (a) and (b), respectively, as well as the subsequent kinetic and binding energy diagrams. Due to the close proximity of the Fermi level to the valence band, a significant excess of oxygen can lead to a quasi-metallic state. A shift to lower E_{kin} corresponds to a shift to higher E_B .

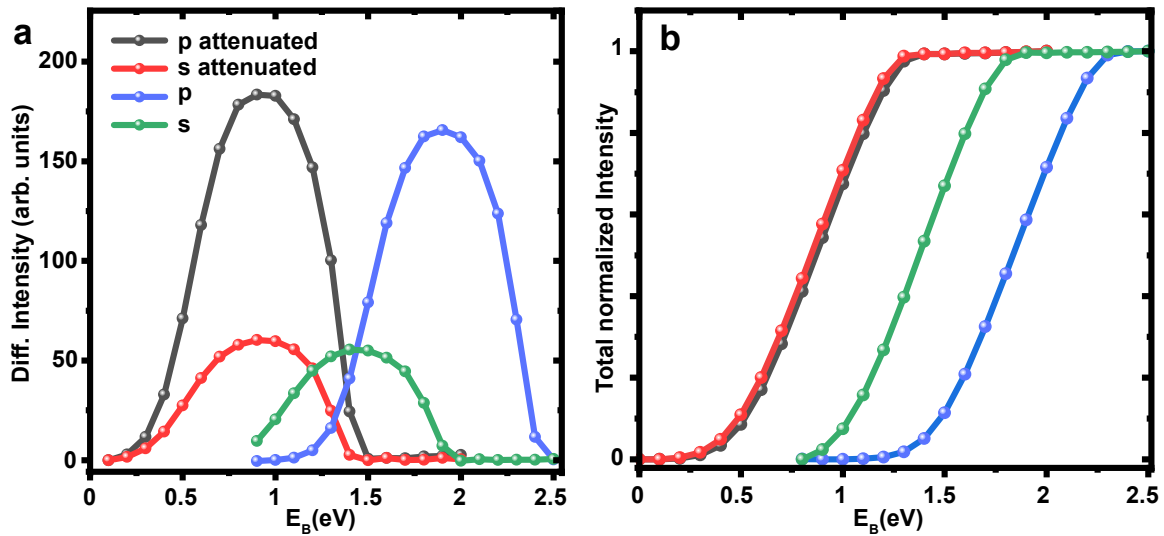


Figure 5.3: (a) Photoelectron yield per binding energy for s - and p -polarized light at 5.2 eV as well as the same scans performed with an attenuation filter. (b) Total normalized photoelectron yield of the measurements shown in (a).

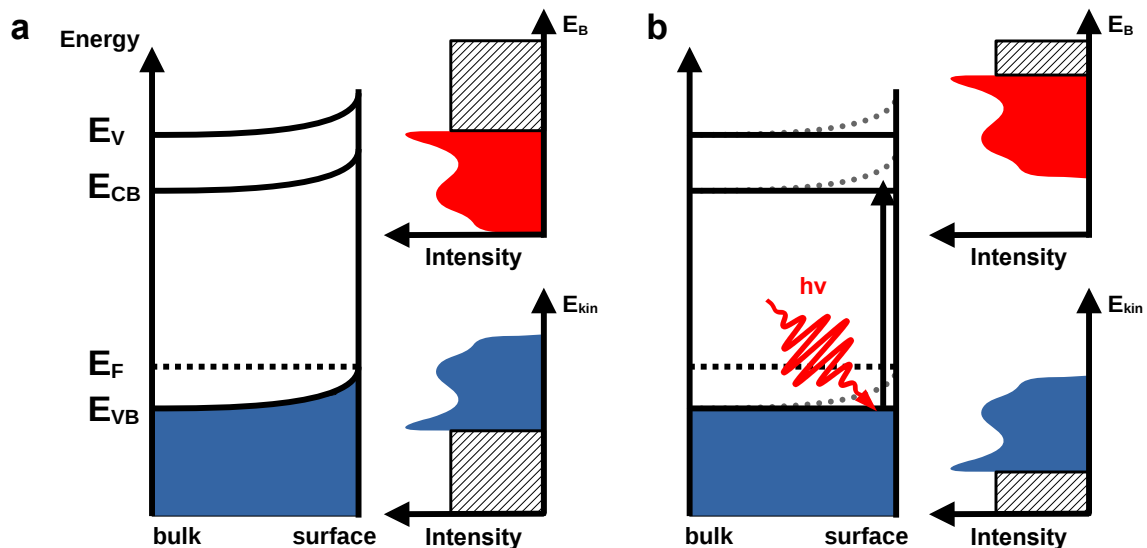


Figure 5.4: (a) Schematic illustrating the light induced band bending. (b) Corresponding impact on the energy distribution of the emitted photoelectrons. The black hatched boxes are explained in Figure 2.1.

Depending on the intensity of the UV source and the presence of a so-called surface photovoltage, the detected E_B shifts with respect to the work function of the detector (see Figure 2.1). The surface photovoltage is caused by the separation of holes and electrons in the presence of a strong electromagnetic field of a surface space charge layer [267, 268]. Consequently, reducing the intensity of illumination should reduce the screening, hence reducing the detected shift of the valence bands. Indeed, this is shown in Figure 5.3 in black and red, where the Hg source is attenuated to 1/10

of the intensity with a neutral density filter, which results in $\approx 170 \text{ cd/mm}^2$. Now, $E_B = 0$ again coincides with the onset of the energy scan and there is no significant shift between s - and p -polarized light which proves the hypothesis of a bend bending effect. In case of intense illumination or increased penetration due to P perpendicular to the surface, the band bending is screened, which decreases the detected E_{kin} and increases the apparent E_B .

The observed band bending in Figure 5.3 is 0.5 and 0.9 eV in case of s - and p -polarized light, respectively. This is slightly larger than reports from polycrystalline NiO powders suggest [269]. This may be explained by the different vacancy concentration.

Calculating the asymmetry with attenuated p - and s -polarized light similar to Figure 5.2 leaves no residual contrast ($< 0.1\%$) for the chosen geometry. Hence, when avoiding the band bending effect shifting the valence bands, no linear dichroism can be detected. This effect is generally not discussed in the publications mentioned above, possibly due to the lack of an energy filter setup. Since the band bending is a function of the oxygen deficiencies, the resulting contrast can also be attributed to an effective work function difference. Similar to reports in the literature, extensive sputtering and subsequent annealing changes the oxygen concentration at the surface, which changes the dominance of the work function contrast in standard PEEM images, as well as the magnitude of the observed band bending.

In any case, we can conclude that the asymmetry measured in standard threshold PEEM is not of antiferromagnetic origin.

5.4 Conclusion & Outlook

In conclusion, we discussed and showed first LD PEEM measurements of NiO to investigate the AF order. Our observations are consistently explained by crystallographic and surface voltage effects. There may be a coincidence with AF domains, but to conclude on that, further experiments are needed. First, the surface quality will be optimized by extensive heating in oxygen atmosphere. This should result in a stoichiometric surface and is the standard sample treatment for SHG measurements [256]. Furthermore, thin NiO single crystals ($d = 100 \mu\text{m}$) will be used in the future. Their T-domain structure will be confirmed by optical polarization microscopy measurements prior to the threshold PEEM experiments. We will also perform laser

experiments on these samples, which allow for a continuous control of the illumination intensity. This data should give a better control of the aforementioned surface photovoltage shift.

Unfortunately, there is still a lack of reliable theoretical calculations regarding photoemission in NiO. Here, the general difficulty is the correct description of strongly correlated transition metal oxides. This strong correlation originates from the very narrow d bands. In case of our relativistic OMNI calculation approach, no satisfying electron potentials exist, which have to be obtained from density functional theory. Despite these theoretical problems, once we obtain a real AF contrast in near-threshold PEEM, we will combine the knowledge about the ultrafast dynamics in NiO discovered in our group [26], to image the coherent THz oscillations of the photo-induced in-gap state in momentum and real-space. This would pave the way to the explorations of many-body physics in other correlated (AF) oxides via near-threshold PEEM and ultrafast optical excitation.

Chapter 6

Summary & Outlook

The goal of this work was the development of a new UHV PEEM setup for the investigation and control of the electron and spin system of magnetic surfaces via optical excitation. We investigated magnetic single crystals, thin films and nanostructures on nanometer-femtosecond scales with a newly-designed experimental setup. We combined state-of-the-art PEEM with circular and linear dichroism imaging and normal incidence excitation in conjunction with a tunable femtosecond fiber laser system. Thereby, we reported on two dichroism imaging techniques, namely magnetic circular dichroism and the recently discovered plasmonic dichroism. The first was used to image magnetic in-plane and out-of-plane domains of ferromagnetic surfaces. The second was successfully used to image propagating SPPs on a ferromagnetic material in threshold photoemission for the first time. The recently discovered plasmonic spin-Hall effect results in CD in threshold laser PEEM, which we used to identify propagating SPPs on polycrystalline $\text{Ni}_{80}\text{Fe}_{20}$ microstructures. With this, we imaged clear edge-induced SPPs with sub-micrometer wavelength and propagation length of about $3.5\ \mu\text{m}$, providing valuable insights into the dielectric properties of the surface. This finding extends experimental investigation of SPPs to materials with high plasma frequency and large damping.

Furthermore, we used the group theory ansatz in valence band dichroism to optimize investigating ferromagnetic domains of Fe and Ni surfaces in real and momentum space. The dichroic images have a spatial resolution and amplitude which are orders-of-magnitude better than previously reported in near-threshold PEEM, exceeding the resolution of conventional optical techniques like MOKE. We compared energy-resolved asymmetry scans and momentum space images with fully relativistic one-step layer-KKR photoemission calculations, which showed a remarkable accordance. This allowed us to deconvolute the spin-orbit and exchange contribution to the observed asymmetry k-space images. These results pave the way for further investigation of the electron and spin system of several ferromagnetic compounds by means of time-resolved threshold PEEM. For example, the high spatial resolution will be used to investigate the room-temperature skyrmion bubble state in

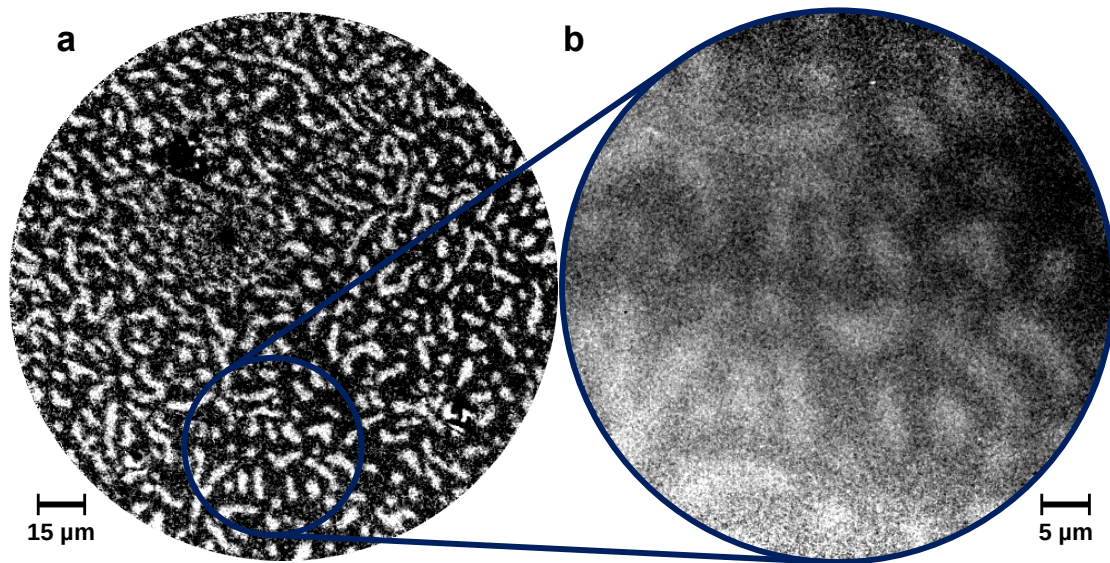


Figure 6.1: (a) MCD PEEM image of a 12 ML Ni(100) film illuminated with a *cw* light source. (b) Zoomed-in MCD PEEM image illuminated with 30 fs laser pulses at 4.53 eV.

thin CoFeB wedges already investigated via MOKE [270].

In the future, our setup will be used for time-resolved PEEM measurements. This is a highly non-trivial task, since it requires a stable, magnetic configuration, which can be stroboscopically excited and imaged via pump-probe measurements. We measured preliminary laser PEEM experiments, in which we successfully observed static ferromagnetic domains in Ni films on Cu(100). Figure 6.1 shows a comparison between an MCD PEEM image measured with the Hg lamp (a) and a zoomed-in area illuminated with 30 fs laser pulses at 4.53 eV (b). Due to space charge effects, the spatial resolution decreases significantly [71]. Decreasing the laser power below 1 nJ should prohibit this effect, but increases the acquisition time. Here, the acquisition time already exceed 30 min per laser helicity, given that the laser intensity and position are stable. The implementation of the back-side pump setup, which is explained in section 4.5, will help to decrease space charge effects in a way that we can operate the time-resolved experiments at higher flux. Pinned domain walls at iron surfaces are potential candidates for stroboscopic measurements, since they seem to be very stable even after heating above T_C . Additionally, investigations of GdFeCo or Co/Pt samples are planned, which are known for their all-optical switching capabilities [15, 271, 272]. Here, layers or microstructures could be deterministically and periodically reset to the initial magnetic state in order to observe the time-dependent switching behavior in real and momentum space.

Finally, the know-how of our group regarding HHG will eventually be used to combine the excess power of the fiber laser with a suitable HHG chamber. This, together with the time-resolution capabilities, will open up new horizons for in-lab

investigations of various material classes and their physical phenomena.

Non-physical epilogue

Since we started this thesis with a non-physical introduction grounding our field of research in the overarching challenges of society, we might as well end with a non-physical comment on that. Yet, despite all the scientific progress we as physicists might achieve in this field, we can only hope to discover the tools for solving the problems mentioned in the introduction. And even if we are successful in leading the way to new, highly efficient, low-cost and sustainable spintronic devices, history tells us that this will not be a solution. Scientific and technological progress in information technology has not led to less energy consumption or less pollution, it has led to bigger TV screens, heavier cars and faster Bitcoin farms, a rebound effect that is known as the efficiency paradox (or Jevon's paradox [273]).

This does not mean that all scientific endeavor is inherently pointless and that we should not pursue to overcome these technical and scientific challenges, the contrary is true. Even more extreme, our field of basic research should not have to justify its usefulness at all, the pursuit for knowledge is in itself a sufficient reason for our endeavors. But, we actually do have to justify our purpose before society, since we as scientists have accepted a symbiotic agreement with it, getting freedom, education, financial security and social status in exchange for contributing to solve societal problems, giving advice and council, and increasing humanity's understanding of the world. That is why in every funding proposal, we tend to justify our research by promising a contribution to solve these problems, which fundamentally cannot be solved by technological or scientific advancement. By these promises, we run the risk of fooling people into believing there might be a technological solution, which hinders already viable social-political change. So with these thoughts, I want to leave the reader with the sincerest hope that more scientists not only focus on scientific breakthroughs in their field, but also take active part in the exchange with society to steer a fundamental shift in the perception of what is meant by technological progress for the sustainable benefit of all humanity.

Appendix A

Preparation of Fe/MgO wedges

As an extension of the measurements presented in Chapter 4, we will look at Fe thin films on MgO(100) single crystals. This system has a number of benefits with respect to our Femto-PEEM chamber. We will use the previous results on Fe single crystals to prepare samples for testing the upcoming time-resolved laser measurements. Therein, we want to pump the surface from the back-side and probe it from the front, hence reducing space charge and being able to investigate transport processes through the sample or intermediate layers. For this, we want to grow wedges of Fe on MgO(001). The latter is an insulating substrate with a band gap of > 6 eV [274] (the exact value is highly dependent on bulk defects). Hence, even pulses from our laser setup with the highest energy (see Section 2.1.2) will not interact with the substrate and only excite the metal at the front.

Therefore, we already investigated the growth of Fe thin films on MgO(001) single crystals whilst using a sample holder with free backside access. However, this preparation turned out to be more complicated than expected. To eliminate carbon- and OH-contamination on the MgO(001) surface, one can not use classical sputter and annealing cycles, since the temperatures required for healing the sputter trenches tend to break the crystal. We also use polished single crystals, which significantly differ from cleaved samples used in literature [275]. Hence, we had to establish *in situ* MgO growth on top of commercial MgO(001) samples, which buries adsorbates and still results in well-ordered surfaces. With increasing quality of the MgO(001) surface, the number of available pinning centers such as surface defects and adsorbates went down, which function as nucleation sites for the Fe layer.

Figure A.1 shows the effect of the absence of pinning centers on the growth of ultrathin Fe layers. It leads to a pronounced Fe-MgO dewetting processes for growth recipes reported in literature [276–278]. Figure A.1(a) shows a scanning-tunneling microscopy image of 4.2 nm Fe deposited via MBE on an MgO/MgO(100) substrate. Instead of a closed layer, we observe islands below 100 nm in lateral size. The edges are oriented along high symmetry directions. An inverse pattern can be observed for higher Fe coverage. This is shown in the AFM images in Figure

A.1(b) and (c). After evaporation of nominally 19.4 nm Fe, the material tends to form a closed layer or net-like structures depending on the annealing temperature. Hence, we deal with a trade-off between high temperatures needed for high structural order, and high temperatures leading to increased dewetting of the Fe layer. Figure A.1(d) shows an MFM measurement of a closed Fe layer, revealing a faint magnetic contrast. This structure is not ideal for magnetic dichroism imaging in PEEM, since the magnetization direction seems to turn continuously within the resolution limit.

To overcome these problems, we develop a growth recipe for high-quality epitaxial Fe(001) films and wedges on MgO(001) controlled by LEED, ARPES and XPS. To

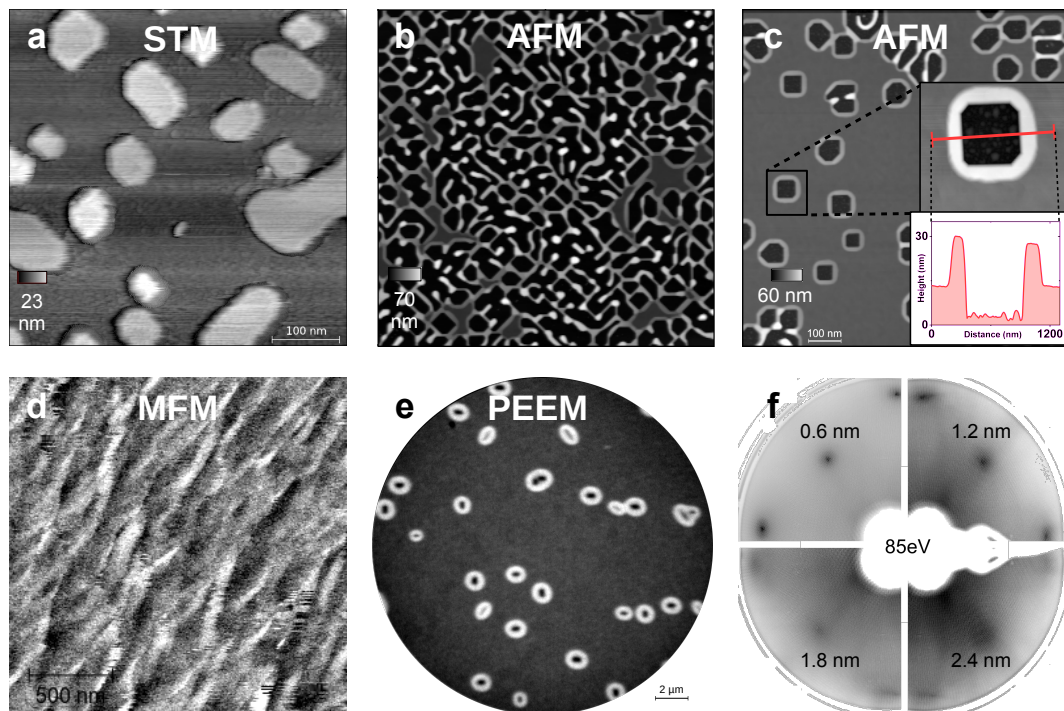


Figure A.1: Growth characterization of Fe(001) films on polished MgO(001) substrates: (a) STM image (0.5 V, 1 nA) of a 4.2 nm Fe layer which dewetted the MgO substrate while evaporating at 400 K, forming flat Fe islands with edges along the crystal symmetry directions (measurement done by Ronny Zemmann). (b) and (c) show AFM images for 19.4 nm thick Fe films grown at 190 K. Subsequent slow annealing to 800 K and 670 K, respectively, results in characteristic dewetting nets and holes, which are again aligned along the crystallographic high-symmetry directions. The inset shows a measurement of one of the holes with decreased FoV, where the respective cross section is marked in red. (d) MFM image of the closed parts of the Fe film in (c) revealing a cloudy magnetic domain structure with only weak magnetic oop contrast. (e) Standard PEEM image of a Fe/MgO wedge at a local thickness of 7 nm prepared for backside-pump experiments. (f) LEED patterns for four epitaxial Fe films on MgO/MgO(001) after evaporation at 300 K, with the Fe thicknesses indicated in each of the quarters (measurements done by Mathias Augstein).

reduce the dewetting, we evaporate Fe at 77 K and subsequently anneal the sample slowly to 300 K. To avoid charging in PEEM, a 1 nm thick Fe film is evaporated on top after annealing. Currently, we use the same setup already introduced for Ni to create a well-defined Fe wedge (see Section 4.3). A proof-of-principle measurement is shown in Figure A.1(e), where we reduced the size and density of the dewetting holes, while having no problems caused by space charge effects. LEED measurements such as those presented in Figure A.1(f) confirm the quality of the wedge, which, up to now, decreases rapidly with increasing Fe thickness. These optimized thin-film wedges are the basis for future time-resolved experiments.

Appendix B

omni package for calculating photoemission

The OMNI package is a numerical calculation toolkit developed and maintained by Dr. Jürgen Henk employing a fully relativistic one-step layer-KKR photoemission model [27, 28]. It is used in several occasions in this thesis to calculate the expected photoemission intensity for a given experimental setup. However, the package is much more powerful and the calculation possibilities include the fully-relativistic (complex) band structure, photoemission currents, density of states, Bloch-wave transmission or spectral density.

We want to briefly comment on the usage of the code from the eyes of an experimentalist. We take the OMNI package provided by Dr. Jürgen Henk and feed it with an input file defining the specifics of the experiment. The input file used for the results of the Fe calculations discussed in Chapter 4 is given at the end of this appendix.

In the framework of the calculation, the photoemission process is simulated as a time-reversed LEED state. This means that the calculation starts with an electron impinging on the surface of the material, which then results in a photon being emitted with a specific energy and momentum. Hence, at first, the electron has to transmit the surface potential, which we set as a Henk-Schattke barrier [279]. The material, Fe in our case, consists of several layers, represented by different elements per material slab, each featuring different electron potentials. These potentials are taken from density functional theory calculations and were also provided by Dr. Jürgen Henk. Within each layer, the position of the atoms is specified with respect to the previous layer. The interaction of the impinging electron is then consecutively calculated down to the bottom layer.

For our calculation, we set the temperature of the system to 0 K, and we desisted from implementing structural disorder. The dielectric function of Fe is specified by experimental values from Werner *et al.* [280]. For the plots in Chapter 4, we chose an energy averaging window of 0.1 eV, which is consistent with our experiment.

The k-space maps were subsequently smoothed. Polarization, magnetization and structural symmetry directions were implemented according to our experiment.

```

1  Omni2k (C++ version)
2  ARPES
3  Fe(001) — E_F = -4.6327 eV
4  + Job specifications ++++++
5  + Global parameters ++++++
6  2 3 30 15.00 1.00 -1 0 0 0.01 0 0 spec, lmax, nlay, eg, xrel, dbl, dis, xmin
7  + Energy parameters ++++++
8  0 0.01 0.7 0.02 energy range
9  5.2 omega
10 + Electric-field parameters (only for photoemission) ++++
11 (-4.1556, 4.4449) epsilon
12 65.0 65.0 1.0 0.0 0.0 0.2 0 theta, phi
13 (1.00000, 0.00000) (0.00000, 1.00000) as, ap
14 + Incident electron polarization (only for SPLEED) ++++++
15 0.0000 1.0000 0.0000 polarization
16 + Temperature ++++++
17 0.0000 temperature
18 + Symmetry parameters (only for bands and LDOS) ++++++
19 2 1 angular representation, frame
20 0.0000000000 initial z-rotation
21 0.0000000000 0.0000000000 1.0000000000 local angular-momentum axis
22 0.0000000000 0.0000000000 1.0000000000 local spin axis
23 0 1
24 0 1 0 1 0 1
25 0 1 0 1 0 1 0 1 0 1
26 0 1 0 1 0 1 0 1 0 1 0 1
27 + Crystal set-up ++++++
28 + Global parameters ++++++
29 5.41 lattice constant (Bohr)
30 1.00000000 0.0000000000 0.0000000000 1.0000000000 base vectors
31 + Element definitions ++++++
32 8 number of elements
33 + Element 0
34 Fe Fe.omni 1.0 1 Fe.omni 1.0 1 1.00
35 + Element 1
36 Fe_1 Fe_1.omni 1.0 1 Fe_1.omni 1.0 1 1.00
37 + Element 2
38 Fe_2 Fe_2.omni 1.0 1 Fe_2.omni 1.0 1 1.00
39 + Element 3
40 Fe_3 Fe_3.omni 1.0 1 Fe_3.omni 1.0 1 1.00
41 + Element 4
42 Fe_4 Fe_4.omni 1.0 1 Fe_4.omni 1.0 1 1.00
43 + Element 5
44 Fe_5 Fe_5.omni 1.0 1 Fe_5.omni 1.0 1 1.00
45 + Element 6
46 Fe_6 Fe_6.omni 1.0 1 Fe_6.omni 1.0 1 1.00
47 + Element 7
48 Fex0 Fex0.omni 1.0 1 Fex0.omni 1.0 1 1.00
49 + Layer definitions ++++++
50 8 8 1 0 number of slabs and slices, nbulk
51 + Surface barrier definition ++++++
52 3 0.7574 0.4054 0.1733 barrier (upper)
53 3 0.7574 0.4054 0.1733 barrier (lower)
54 + Slab 0
55 1 14.19796067 natom, v0
56 Fex0 name
57 0.0000000000 0.0000000000 0.0000000000 position
58 -1.0000000000 0.0000000000 0.0000000000 magnetization direction
59 1 0.5000000000 repetition, thickness
60 0.5000000000 0.5000000000 0.5000000000 displacement
61 0.0000 2.000 1.0000 -0.0200 2.000 1.0000 optical potential (upper)
62 0.0000 2.000 1.0000 -0.0200 2.000 0.0000 optical potential (lower)
63 + Slab 1
64 1 14.19796067
65 Fe_6
66 0.0000000000 0.0000000000 0.0000000000
67 -1.0000000000 0.0000000000 0.0000000000
68 1 0.5000000000
69 0.5000000000 0.5000000000 0.5000000000
70 0.0000 2.000 1.0000 -0.0200 2.000 1.0000
71 0.0000 2.000 1.0000 -0.0200 2.000 0.0000

```

```
72 + Slab 2
73 1 14.19796067
74 Fe_5
75 0.0000000000 0.0000000000 0.0000000000
76 -1.0000000000 0.0000000000 0.0000000000
77 1 0.5000000000
78 0.5000000000 0.5000000000 0.5000000000
79 0.0000 2.000 1.0000 -0.0200 2.000 1.0000
80 0.0000 2.000 1.0000 -0.0200 2.000 0.0000
81 + Slab 3
82 1 14.19796067
83 Fe_4
84 0.0000000000 0.0000000000 0.0000000000
85 -1.0000000000 0.0000000000 0.0000000000
86 1 0.5000000000
87 0.5000000000 0.5000000000 0.5000000000
88 0.0000 2.000 1.0000 -0.0200 2.000 1.0000
89 0.0000 2.000 1.0000 -0.0200 2.000 0.0000
90 + Slab 4
91 1 14.19796067
92 Fe_3
93 0.0000000000 0.0000000000 0.0000000000
94 -1.0000000000 0.0000000000 0.0000000000
95 1 0.5000000000
96 0.5000000000 0.5000000000 0.5000000000
97 0.0000 2.000 1.0000 -0.0200 2.000 1.0000
98 0.0000 2.000 1.0000 -0.0200 2.000 0.0000
99 + Slab 5
100 1 14.19796067
101 Fe_2
102 0.0000000000 0.0000000000 0.0000000000
103 -1.0000000000 0.0000000000 0.0000000000
104 1 0.5000000000
105 0.5000000000 0.5000000000 0.5000000000
106 0.0000 2.000 1.0000 -0.0200 2.000 1.0000
107 0.0000 2.000 1.0000 -0.0200 2.000 0.0000
108 + Slab 6
109 1 14.19796067
110 Fe_1
111 0.0000000000 0.0000000000 0.0000000000
112 -1.0000000000 0.0000000000 0.0000000000
113 1 0.5000000000
114 0.5000000000 0.5000000000 0.5000000000
115 0.0000 2.000 1.0000 -0.0200 2.000 1.0000
116 0.0000 2.000 1.0000 -0.0200 2.000 0.0000
117 + Slab 7
118 1 14.19796067
119 Fe
120 0.0000000000 0.0000000000 0.0000000000
121 -1.0000000000 0.0000000000 0.0000000000
122 1 0.5000000000
123 0.5000000000 0.5000000000 0.5000000000
124 0.0000 2.000 1.0000 -0.0200 2.000 1.0000
125 0.0000 2.000 1.0000 -0.0200 2.000 0.0000
126 + k-parallel and angular parameters ++++++
127 2
128 0
129 -0.140 0.140 0.004 -0.140 0.140 0.004
130 0
131 1 k.mesh
132 0
133 1 k.mesh
```


Bibliography

- ¹F. Scheidler, *Blätter für deutsche und internationale Politik* **4/21**, 12 (2021).
- ²G. E. Moore, *Proceedings of the IEEE* **86**, 82–85 (1998).
- ³A. Makarov, T. Windbacher, V. Sverdlov, and S. Selberherr, *Semiconductor Science and Technology* **31**, 113006 (2016).
- ⁴A. Hirohata, K. Yamada, Y. Nakatani, I.-L. Prejbeanu, B. Diény, P. Pirro, and B. Hillebrands, *Journal of Magnetism and Magnetic Materials* **509**, 166711 (2020).
- ⁵S. A. Nikitov, A. R. Safin, D. V. Kalyabin, A. V. Sadovnikov, E. N. Beginin, M. V. Logunov, M. A. Morozova, S. A. Odintsov, S. A. Osokin, A. Y. Sharaevskaya, Y. P. Sharaevsky, and A. I. Kirilyuk, *Physics-Uspekhi* **63**, 945–974 (2020).
- ⁶E. Beaurepaire, J.-C. Merle, A. Daunois, and J.-Y. Bigot, *Physical Review Letters* **76**, 4250–4253 (1996).
- ⁷C. Dornes, Y. Acremann, M. Savoini, M. Kubli, M. J. Neugebauer, E. Abreu, L. Huber, G. Lantz, C. A. F. Vaz, H. Lemke, E. M. Bothschafter, M. Porer, V. Esposito, L. Rettig, M. Buzzi, A. Alberca, Y. W. Windsor, P. Beaud, U. Staub, D. Zhu, S. Song, J. M. Glowia, and S. L. Johnson, *Nature* **565**, 209–212 (2019).
- ⁸S. R. Tauchert, M. Volkov, D. Ehberger, D. Kazenwadel, M. Evers, H. Lange, A. Donges, A. Book, W. Kreuzpaintner, U. Nowak, and P. Baum, *Nature* **602**, 73–77 (2022).
- ⁹C. D. Stanciu, F. Hansteen, A. V. Kimel, A. Kirilyuk, A. Tsukamoto, A. Itoh, and T. Rasing, *Physical Review Letters* **99**, 047601 (2007).
- ¹⁰I. Radu, K. Vahaplar, C. Stamm, T. Kachel, N. Pontius, H. A. Dürr, T. A. Ostler, J. Barker, R. F. L. Evans, R. W. Chantrell, A. Tsukamoto, A. Itoh, A. Kirilyuk, T. Rasing, and A. V. Kimel, *Nature* **472**, 205–208 (2011).
- ¹¹C.-H. Lambert, S. Mangin, B. S. D. C. S. Varaprasad, Y. K. Takahashi, M. Hehn, M. Cinchetti, G. Malinowski, K. Hono, Y. Fainman, M. Aeschlimann, and E. E. Fullerton, *Science* **345**, 1337–1340 (2014).
- ¹²J. T. Heron, J. L. Bosse, Q. He, Y. Gao, M. Trassin, L. Ye, J. D. Clarkson, C. Wang, J. Liu, S. Salahuddin, D. C. Ralph, D. G. Schlom, J. Íñiguez, B. D. Huey, and R. Ramesh, *Nature* **516**, 370–373 (2014).

- ¹³J. Gorchon, Y. Yang, and J. Bokor, *Physical Review B* **94**, 020409 (2016).
- ¹⁴J. Gorchon, C.-H. Lambert, Y. Yang, A. Pattabi, R. B. Wilson, S. Salahuddin, and J. Bokor, *Applied Physics Letters* **111**, 042401 (2017).
- ¹⁵M. L. M. Laliou, M. J. G. Peeters, S. R. R. Haenen, R. Lavrijsen, and B. Koopmans, *Physical Review B* **96**, 220411 (2017).
- ¹⁶S. Iihama, Y. Xu, M. Deb, G. Malinowski, M. Hehn, J. Gorchon, E. E. Fullerton, and S. Mangin, *Advanced Materials* **30**, 1804004 (2018).
- ¹⁷M. Fechner, A. Sukhov, L. Chotorlishvili, C. Kenel, J. Berakdar, and N. A. Spaldin, *Physical Review Materials* **2**, 064401 (2018).
- ¹⁸P. Němec, M. Fiebig, T. Kampfrath, and A. V. Kimel, *Nature Physics* **14**, 229–241 (2018).
- ¹⁹T. S. Seifert, S. Jaiswal, J. Barker, S. T. Weber, I. Razdolski, J. Cramer, O. Gueckstock, S. F. Maehrlein, L. Nadvornik, S. Watanabe, C. Ciccarelli, A. Melnikov, G. Jakob, M. Münzenberg, S. T. B. Goennenwein, G. Woltersdorf, B. Rethfeld, P. W. Brouwer, M. Wolf, M. Kläui, and T. Kampfrath, *Nature Communications* **9**, 2899 (2018).
- ²⁰J. Chen, U. Bovensiepen, A. Eschenlohr, T. Müller, P. Elliott, E. K. U. Gross, J. K. Dewhurst, and S. Sharma, *Physical Review Letters* **122**, 067202 (2019).
- ²¹F. Siegrist, J. A. Gessner, M. Ossiander, C. Denker, Y.-P. Chang, M. C. Schröder, A. Guggenmos, Y. Cui, J. Walowski, U. Martens, J. K. Dewhurst, U. Kleineberg, M. Münzenberg, S. Sharma, and M. Schultze, *Nature* **571**, 240–244 (2019).
- ²²E. Y. Vedmedenko, R. K. Kawakami, D. D. Sheka, P. Gambardella, A. Kirilyuk, A. Hirohata, C. Binck, O. Chubykalo-Fesenko, S. Sanvito, B. J. Kirby, J. Grollier, K. Everschor-Sitte, T. Kampfrath, C.-Y. You, and A. Berger, *Journal of Physics D: Applied Physics* **53**, 453001 (2020).
- ²³A. Höfer, K. Duncker, M. Kiel, S. Forster, and W. Widdra, *IBM Journal of Research and Development* **55**, 4:1–4:8 (2011).
- ²⁴A. Höfer, M. Fechner, K. Duncker, M. Hölzer, I. Mertig, and W. Widdra, *Physical Review Letters* **108**, 087602 (2012).
- ²⁵A. Sander, M. Christl, C.-T. Chiang, M. Alexe, and W. Widdra, *Journal of Applied Physics* **118**, 224102 (2015).
- ²⁶K. Gillmeister, D. Golež, C.-T. Chiang, N. Bittner, Y. Pavlyukh, J. Berakdar, P. Werner, and W. Widdra, *Nature Communications* **11**, 4095 (2020).
- ²⁷W. Kohn and N. Rostoker, *Physical Review* **94**, 1111–1120 (1954).
- ²⁸J. Korrynga, *Physica* **13**, 392–400 (1947).

- ²⁹M. Henzler and W. Göpel, *Oberflächenphysik des Festkörpers*, 2., durchges. Aufl., Teubner-Studienbücher Physik (Teubner, Stuttgart, 1994).
- ³⁰K. Oura, M. Katayama, A. V. Zotov, V. G. Lifshits, and A. A. Saranin, *Surface science*, Advanced Texts in Physics (Springer Berlin Heidelberg, Berlin, Heidelberg, 2003).
- ³¹M. Rocca, T. S. Rahman, and L. Vattuone, eds., *Springer handbook of surface science*, Springer Handbooks (Springer International Publishing, Cham, 2020).
- ³²A. Einstein, *Annalen der Physik* **322**, 132–148 (1905).
- ³³P. Lenard, *Annalen der Physik* **307**, 359–375 (1900).
- ³⁴P. Lenard, *Annalen der Physik* **313**, 149–198 (1902).
- ³⁵David Cahen, *Advanced Materials* **15**, 271–277 (2003).
- ³⁶S. Doniach and M. Sunjic, *Journal of Physics C: Solid State Physics* **3**, 285–291 (1970).
- ³⁷J. Braun, G. Thörner, and G. Borstel, *physica status solidi (b)* **130**, 643–654 (1985).
- ³⁸G. Thörner and G. Borstel, *physica status solidi (b)* **126**, 617–628 (1984).
- ³⁹J. Braun, G. Borstel, and W. Nolting, *Physical Review B* **46**, 3510–3519 (1992).
- ⁴⁰W. Nolting, W. Borgiel, V. Dose, and T. Fauster, *Physical Review B* **40**, 5015–5027 (1989).
- ⁴¹C. M. Schneider and J. Kirschner, *Critical Reviews in Solid State and Materials Sciences* **20**, 179–283 (1995).
- ⁴²B. Schmiedeskamp, B. Vogt, and U. Heinzmann, *Physical Review Letters* **60**, 651–654 (1988).
- ⁴³A. Winkelmann, C. Tusche, A. Akin Ünal, M. Ellguth, J. Henk, and J. Kirschner, *New Journal of Physics* **14**, 043009 (2012).
- ⁴⁴J. Hermanson, *Solid State Communications* **22**, 9 (1977).
- ⁴⁵W. Eberhardt and F. J. Himpsel, *Physical Review B* **21**, 5572–5576 (1980).
- ⁴⁶G. Borstel, *Applied Physics A* **38**, 193–204 (1985).
- ⁴⁷G. Borstel, M. Neumann, and M. Wöhlecke, *Physical Review B* **23**, 3121–3124 (1981).
- ⁴⁸M. Wöhlecke and G. Borstel, *Physical Review B* **23**, 980–985 (1981).
- ⁴⁹W. Kuch and C. M. Schneider, *Reports on Progress in Physics* **64**, 147–204 (2001).
- ⁵⁰C. M. Schneider and G. Schönhense, *Reports on Progress in Physics* **65**, 1785–1839 (2002).

- ⁵¹A. Höfer, “Laser-angeregte Photoemissions-Elektronenmikroskopie an oxidischen Oberflächen”, PhD thesis (Martin-Luther-Universität Halle-Wittenberg, Halle (Saale), 2012).
- ⁵²L. I. Chelaru, M. Horn-von Hoegen, D. Thien, and F.-J. Meyer zu Heringdorf, *Physical Review B* **73**, 115416 (2006).
- ⁵³M. Ouyang, Y. Cao, H. Gao, J. Shi, J. Zhou, and D. Liu, *Optics & Laser Technology* **40**, 201–207 (2008).
- ⁵⁴M. T. Tavassoly, M. Amiri, A. Darudi, R. Aalipour, A. Saber, and A.-R. Moradi, *Journal of the Optical Society of America A* **26**, 540 (2009).
- ⁵⁵M. T. Tavassoly, I. M. Haghighi, and K. Hassani, *Applied optics* **48**, 5497–5501 (2009).
- ⁵⁶M. P. Seah and W. A. Dench, *Surface and Interface Analysis* **1**, 2–11 (1979).
- ⁵⁷Lexikon der Physik, (1998) <https://www.spektrum.de/lexikon/physik/inelastische-mittlere-freie-weglaenge/7219> (visited on 11/23/2021).
- ⁵⁸G. Schönhense and H. C. Siegmann, *Annalen der Physik* **505**, 465–474 (1993).
- ⁵⁹M. Rollinger, “Investigation of magnetic and magneto-plasmonic effects via photoemission electron microscopy”, PhD thesis (Technische Universität Kaiserslautern, Kaiserslautern, 2018).
- ⁶⁰J. Hong and D. L. Mills, *Physical Review B* **62**, 5589–5600 (2000).
- ⁶¹V. P. Zhukov, E. V. Chulkov, and P. M. Echenique, *Physical Review B* **73**, 125105 (2006).
- ⁶²R. Zdyb, T. O. Menteş, A. Locatelli, M. A. Niño, and E. Bauer, *Physical Review B* **87**, 075436 (2013).
- ⁶³C. Chantler and J. Bourke, *Ultramicroscopy* **201**, 38–48 (2019).
- ⁶⁴D. Geelen, J. Jobst, E. E. Krasovskii, S. J. van der Molen, and R. M. Tromp, *Physical Review Letters* **123**, 086802 (2019).
- ⁶⁵O. Y. Ridzel, V. Astašauskas, and W. S. Werner, *Journal of Electron Spectroscopy and Related Phenomena* **241**, 146824 (2020).
- ⁶⁶L. Frank, I. Müllerová, D. A. Valdaitsev, A. Gloskovskii, S. A. Nepijko, H.-J. Elmers, and G. Schönhense, *Journal of Applied Physics* **100**, 093712 (2006).
- ⁶⁷H. C. Siegmann, *Journal of Physics: Condensed Matter* **4**, 8395–8434 (1992).
- ⁶⁸K. Göhler, A. B. Schmidt, and M. Donath, *Journal of Vacuum Science & Technology A* **39**, 023205 (2021).

- ⁶⁹A. Jablonski and C. J. Powell, *Journal of Physical and Chemical Reference Data* **49**, 033102 (2020).
- ⁷⁰Y. Ishida, J. K. Jung, M. S. Kim, J. Kwon, Y. S. Kim, D. Chung, I. Song, C. Kim, T. Otsu, and Y. Kobayashi, *Communications Physics* **3**, 158 (2020).
- ⁷¹N. M. Buckanie, J. Göhre, P. Zhou, D. von der Linde, M. Horn-von Hoegen, and F.-J. Meyer zu Heringdorf, *Journal of Physics: Condensed Matter* **21**, 314003 (2009).
- ⁷²F. P. Orsitto, D. Del Bugaro, M. DiFino, A. Maiolo, M. Montecchi, E. Nichelatti, C. Gowers, and P. Nielsen, *Review of Scientific Instruments* **72**, 540–544 (2001).
- ⁷³K. Duncker, M. Kiel, and W. Widdra, *Surface Science* **606**, L87–L90 (2012).
- ⁷⁴C.-T. Chiang, M. Huth, A. Trützscher, M. Kiel, F. O. Schumann, J. Kirschner, and W. Widdra, *New Journal of Physics* **17**, 013035 (2015).
- ⁷⁵K. Gillmeister, M. Kiel, and W. Widdra, *Physical Review B* **97**, 085424 (2018).
- ⁷⁶D. J. Richardson, J. Nilsson, and W. A. Clarkson, *Journal of the Optical Society of America B* **27**, B63 (2010).
- ⁷⁷M. N. Zervas and C. A. Codemard, *IEEE Journal of Selected Topics in Quantum Electronics* **20**, 219–241 (2014).
- ⁷⁸D. Strickland and G. Mourou, *Optics Communications* **55**, 447–449 (1985).
- ⁷⁹J. Limpert, T. Clausnitzer, A. Liem, T. Schreiber, H.-J. Fuchs, H. Zellmer, E.-B. Kley, and A. Tnnermann, *Optics Letters* **28**, 1984–1986 (2003).
- ⁸⁰C. Homann, C. Schriever, P. Baum, and E. Riedle, *Optics Express* **16**, 5746 (2008).
- ⁸¹K. Duncker, “Homo- und heterochirale kommensurate Molekülstrukturen in der Sexithiophen-Monolage auf einer Ag(001)-Oberfläche” (Martin-Luther-Universität Halle-Wittenberg, Halle (Saale), 2008).
- ⁸²K. Gillmeister, “Zeitaufgelöste Zweiphotonen-Photoemission an ultradünnen Nickeloxidschichten auf Silber(001)”, PhD thesis (Martin-Luther-Universität Halle-Wittenberg, Halle (Saale), 2014).
- ⁸³G. Schönhense and U. Heinzmann, *Journal of Physics E: Scientific Instruments* **16**, 74–82 (1983).
- ⁸⁴C. T. Rueden, J. Schindelin, M. C. Hiner, B. E. DeZonia, A. E. Walter, E. T. Arena, and K. W. Eliceiri, *BMC Bioinformatics* **18**, 529 (2017).
- ⁸⁵J. Schindelin, I. Arganda-Carreras, E. Frise, V. Kaynig, M. Longair, T. Pietzsch, S. Preibisch, C. Rueden, S. Saalfeld, B. Schmid, J.-Y. Tinevez, D. J. White, V. Hartenstein, K. Eliceiri, P. Tomancak, and A. Cardona, *Nature Methods* **9**, 676–682 (2012).
- ⁸⁶G. Bradski, *Dr. Dobb’s Journal of Software Tools* **25**, 120 (2000).

- ⁸⁷*Originpro*, version 2019, MA, USA: OriginLab Corporation.
- ⁸⁸E. Merritt, *Annalen der Physik und Chemie* **291**, 49–64 (1895).
- ⁸⁹C. Mathieu, C. Lubin, G. Le Doueff, M. Cattelan, P. Gemeiner, B. Dkhil, E. K. H. Salje, and N. Barrett, *Scientific Reports* **8**, 1–7 (2018).
- ⁹⁰Y. Motoyui, T. Taniuchi, P. Scheiderer, J. N. Lee, J. Gabel, F. Pfaff, M. Sing, M. Lippmaa, R. Claessen, and S. Shin, *Journal of the Physical Society of Japan* **88**, 034717 (2019).
- ⁹¹T. A. Ostler, J. Barker, R. F. L. Evans, R. W. Chantrell, U. Atxitia, O. Chubykalo-Fesenko, S. El Moussaoui, L. Le Guyader, E. Mengotti, L. J. Heyderman, F. Nolting, A. Tsukamoto, A. Itoh, D. Afanasiev, B. A. Ivanov, A. M. Kalashnikova, K. Vahaplar, J. Mentink, A. Kirilyuk, T. Rasing, and A. V. Kimel, *Nature Communications* **3**, 666 (2012).
- ⁹²M. Staab, D. Kutnyakhov, R. Wallauer, S. Chernov, K. Medjanik, H. J. Elmers, M. Kläui, and G. Schönhense, *Physical Review B* **95**, 165437 (2017).
- ⁹³K. Vahaplar, A. M. Kalashnikova, A. V. Kimel, S. Gerlach, D. Hinzke, U. Nowak, R. Chantrell, A. Tsukamoto, A. Itoh, A. Kirilyuk, and T. Rasing, *Physical Review B* **85**, 104402 (2012).
- ⁹⁴X. Wang and Z. Tang, *Small* **13**, 1601115 (2017).
- ⁹⁵K. Arai, T. Okuda, A. Tanaka, M. Kotsugi, K. Fukumoto, T. Ohkochi, T. Nakamura, T. Matsushita, T. Muro, M. Oura, Y. Senba, H. Ohashi, A. Kakizaki, C. Mitsumata, and T. Kinoshita, *Physical Review B* **85**, 104418 (2012).
- ⁹⁶T. Kinoshita, K. Arai, K. Fukumoto, T. Ohkochi, M. Kotsugi, F. Guo, T. Muro, T. Nakamura, H. Osawa, T. Matsushita, and T. Okuda, *Journal of the Physical Society of Japan* **82**, 021005 (2013).
- ⁹⁷E. Gentsch, <https://www.thorlabs.com/>, (2017) https://www.thorlabs.com/images/Tabimages/Polarization_Handedness_Tutorial.pdf.
- ⁹⁸P. A. Kahl, “Anregung, Propagation, Interferenz, Photoemission: Oberflächenplasmonpolaritonen in zeitaufgelöster Photoelektronenemissionsmikroskopie unter senkrechtem Lichteinfall”, PhD thesis (Universität Duisburg-Essen, Duisburg, 2016).
- ⁹⁹B. Schaefer, E. Collett, R. Smyth, D. Barrett, and B. Fraher, *American Journal of Physics* **75**, 163–168 (2007).
- ¹⁰⁰M. Kronseder, *Pattern evolution and fluctuations in a magnetic model system*, 1. Aufl, Dissertationsreihe Der Fakultät Für Physik Der Universität Regensburg 32 (Univ.-Verl, Regensburg, 2013).

- ¹⁰¹S. A. Maier, *Plasmonics: fundamentals and applications*, Vol. 1 (Springer, New York, 2007).
- ¹⁰²M. Cinchetti, A. Oelsner, G. H. Fecher, H. J. Elmers, and G. Schönhense, *Applied Physics Letters* **83**, 1503–1505 (2003).
- ¹⁰³M. Cinchetti and G. Schönhense, *Journal of Physics: Condensed Matter* **17**, S1319–S1328 (2005).
- ¹⁰⁴J. R. Krenn, A. Dereux, J. C. Weeber, E. Bourillot, Y. Lacroute, J. P. Goudonnet, G. Schider, W. Gotschy, A. Leitner, F. R. Aussenegg, and C. Girard, *Physical Review Letters* **82**, 2590–2593 (1999).
- ¹⁰⁵J. R. Krenn, M. Salerno, N. Felidj, B. Lamprecht, G. Schider, A. Leitner, F. R. Aussenegg, J. C. Weeber, A. Dereux, and J. P. Goudonnet, *Journal of Microscopy* **202**, 122–128 (2001).
- ¹⁰⁶B. Lamprecht, J. R. Krenn, G. Schider, H. Ditlbacher, M. Salerno, N. Felidj, A. Leitner, F. R. Aussenegg, and J. C. Weeber, *Applied Physics Letters* **79**, 51–53 (2001).
- ¹⁰⁷J.-C. Weeber, J. R. Krenn, A. Dereux, B. Lamprecht, Y. Lacroute, and J. P. Goudonnet, *Physical Review B* **64**, 045411 (2001).
- ¹⁰⁸G. Banfi, G. Ferrini, M. Peloi, and F. Parmigiani, *Physical Review B* **67**, 035428 (2003).
- ¹⁰⁹A. Kubo, N. Pontius, and H. Petek, *Nano Letters* **7**, 470–475 (2007).
- ¹¹⁰L. I. Chelaru and F.-J. Meyer zu Heringdorf, *Surface Science* **601**, 4541–4545 (2007).
- ¹¹¹P. Johnson and R. Christy, *Physical Review B* **9**, 5056–5070 (1974).
- ¹¹²J. M. Pitarke, V. M. Silkin, E. V. Chulkov, and P. M. Echenique, *Reports on Progress in Physics* **70**, 1–87 (2007).
- ¹¹³P. Kahl, D. Podbiel, C. Schneider, A. Makris, S. Sindermann, C. Witt, D. Kilbane, M. Horn-von Hoegen, M. Aeschlimann, and F.-J. Meyer zu Heringdorf, *Plasmonics* **13**, 239–246 (2018).
- ¹¹⁴Y. Qin, B. Ji, X. Song, and J. Lin, *Photonics Research* **8**, 1042 (2020).
- ¹¹⁵P. Feibelman, *Progress in Surface Science* **12**, 287–407 (1982).
- ¹¹⁶M. A. Cazalilla, J. S. Dolado, A. Rubio, and P. M. Echenique, *Physical Review B* **61**, 8033–8042 (2000).
- ¹¹⁷A. Marini, R. Del Sole, and G. Onida, *Physical Review B* **66**, 115101 (2002).
- ¹¹⁸A. Ciesielski, L. Skowronski, M. Trzcinski, and T. Szoplik, *Applied Surface Science* **421**, 349–356 (2017).

- ¹¹⁹M. Dabrowski, Y. Dai, A. Argondizzo, Q. Zou, X. Cui, and H. Petek, *ACS Photonics* **3**, 1704–1713 (2016).
- ¹²⁰G. Armelles, A. Cebollada, A. García-Martín, and M. U. González, *Advanced Optical Materials* **1**, 10–35 (2013).
- ¹²¹D. T. L. Alexander, D. Forrer, E. Rossi, E. Lidorikis, S. Agnoli, G. D. Bernasconi, J. Butet, O. J. F. Martin, and V. Amendola, *Nano Letters* **19**, 5754–5761 (2019).
- ¹²²V. Bonanni, S. Bonetti, T. Pakizeh, Z. Pirzadeh, J. Chen, J. Nogués, P. Vavassori, R. Hillenbrand, J. Åkerman, and A. Dmitriev, *Nano Letters* **11**, 5333–5338 (2011).
- ¹²³B. C. Choi, H. Xu, G. Hajisalem, and R. Gordon, *Applied Physics Letters* **112**, 022403 (2018).
- ¹²⁴H. M. Luong, M. T. Pham, B. Ai, T. D. Nguyen, and Y. Zhao, *Physical Review B* **99**, 224413 (2019).
- ¹²⁵N. Maccaferri, I. Zubritskaya, I. Razdolski, I.-A. Chioar, V. Belotelov, V. Kapaklis, P. M. Oppeneer, and A. Dmitriev, *Journal of Applied Physics* **127**, 080903 (2020).
- ¹²⁶K. K. Tikuišis, L. Beran, P. Cejpek, K. Uhlířová, J. Hamrle, M. Vaňatka, M. Urbánek, and M. Veis, *Materials & Design* **114**, 31–39 (2017).
- ¹²⁷H. A. Hagelin-Weaver, J. F. Weaver, G. B. Hoflund, and G. N. Salaita, *Journal of Electron Spectroscopy and Related Phenomena* **134**, 139–171 (2004).
- ¹²⁸F. Bisio, R. Proietti Zaccaria, R. Moroni, G. Maidecchi, A. Alabastri, G. Gonella, A. Giglia, L. Andolfi, S. Nannarone, L. Mattera, and M. Canepa, *ACS Nano* **8**, 9239–9247 (2014).
- ¹²⁹M. Sujak and D. Djuhana, *Key Engineering Materials* **855**, 243–247 (2020).
- ¹³⁰N. Maccaferri, X. Inchausti, A. García-Martín, J. C. Cuevas, D. Tripathy, A. O. Adeyeye, and P. Vavassori, *ACS Photonics* **2**, 1769–1779 (2015).
- ¹³¹M. Rollinger, P. Thielen, E. Melander, E. Östman, V. Kapaklis, B. Obry, M. Cinchetti, A. García-Martín, M. Aeschlimann, and E. T. Papaioannou, *Nano Letters* **16**, 2432–2438 (2016).
- ¹³²P. Marchenko, S. Orlov, C. Huber, P. Banzer, S. Quabis, U. Peschel, and G. Leuchs, *Optics Express* **19**, 7244 (2011).
- ¹³³R. C. Word, J. Fitzgerald, and R. Könenkamp, *Ultramicroscopy* **160**, 84–89 (2016).
- ¹³⁴K. Y. Bliokh and F. Nori, *Physical Review A* **85**, 061801 (2012).
- ¹³⁵K. Y. Bliokh, A. Y. Bekshaev, and F. Nori, *Nature Communications* **5**, 3300 (2014).
- ¹³⁶K. Y. Bliokh, F. J. Rodríguez-Fortuño, F. Nori, and A. V. Zayats, *Nature Photonics* **9**, 796–808 (2015).

- ¹³⁷J. Lin, J. P. B. Mueller, Q. Wang, G. Yuan, N. Antoniou, X.-C. Yuan, and F. Capasso, *Science* **340**, 331–334 (2013).
- ¹³⁸Y. Dai, M. Dabrowski, V. A. Apkarian, and H. Petek, *ACS Nano* **12**, 6588–6596 (2018).
- ¹³⁹Y. Dai and H. Petek, *ACS Photonics* **6**, 2005–2013 (2019).
- ¹⁴⁰M. Paleschke, C.-T. Chiang, L. Brandt, N. Liebing, G. Woltersdorf, and W. Widdra, *New Journal of Physics* **23**, 093006 (2021).
- ¹⁴¹D. Babonneau, S. Camelio, L. Simonot, F. Pailloux, P. Gu erin, B. Lamongie, and O. Lyon, *EPL (Europhysics Letters)* **93**, 26005 (2011).
- ¹⁴²Z. Fan and A. O. Govorov, *Nano Letters* **10**, 2580–2587 (2010).
- ¹⁴³J. M. Slocik, A. O. Govorov, and R. R. Naik, *Nano Letters* **11**, 701–705 (2011).
- ¹⁴⁴A. Maradudin, R. Wallis, and G. Stegeman, *Progress in Surface Science* **33**, 171–257 (1990).
- ¹⁴⁵A. V. Zayats, I. I. Smolyaninov, and A. A. Maradudin, *Physics Reports* **408**, 131–314 (2005).
- ¹⁴⁶P. Drude, *Annalen der Physik* **306**, 566–613 (1900).
- ¹⁴⁷N. Buckanie, P. Kirschbaum, S. Sindermann, and F.-J. Meyer zu Heringdorf, *Ultra-microscopy* **130**, 49–53 (2013).
- ¹⁴⁸K. Creath, J. Wyant, and E. Malacara, “Moir e and fringe projection techniques”, in *Optical shop testing*, 2nd ed, Wiley Series in Pure and Applied Optics (Wiley, New York, 1992).
- ¹⁴⁹P. Kahl, S. Wall, C. Witt, C. Schneider, D. Bayer, A. Fischer, P. Melchior, M. Horn-von Hoegen, M. Aeschlimann, and F.-J. Meyer zu Heringdorf, *Plasmonics* **9**, 1401–1407 (2014).
- ¹⁵⁰M. Salou, B. Lescop, S. Rioual, A. Lebon, J. B. Youssef, and B. Rouvellou, *Surface Science* **602**, 2901–2906 (2008).
- ¹⁵¹W. Weiss and W. Ranke, *Progress in Surface Science* **70**, 1–151 (2002).
- ¹⁵²R. Huber, F. Tauser, A. Brodschelm, M. Bichler, G. Abstreiter, and A. Leitenstorfer, *Nature* **414**, 286–289 (2001).
- ¹⁵³K. Ishioka, K. Brixius, U. H ofer, A. Rustagi, E. M. Thatcher, C. J. Stanton, and H. Petek, *Physical Review B* **92**, 205203 (2015).
- ¹⁵⁴L. Landau and E. Lifshits, *Phys. Zeitsch. der Sow.* **8**, 153–169 (1935).
- ¹⁵⁵T. Nakagawa, K. Watanabe, Y. Matsumoto, and T. Yokoyama, *Journal of Physics: Condensed Matter* **21**, 314010 (2009).

- ¹⁵⁶D. E. Aspnes, S. M. Kelso, R. A. Logan, and R. Bhat, *Journal of Applied Physics* **60**, 754–767 (1986).
- ¹⁵⁷I. Vurgaftman, J. R. Meyer, and L. R. Ram-Mohan, *Journal of Applied Physics* **89**, 5815–5875 (2001).
- ¹⁵⁸W. M. Haynes and D. R. Lide, eds., *Crc handbook of chemistry and physics*, 95th ed. (CRC Press, Boca Raton, FL, USA, 2014).
- ¹⁵⁹A. K. Basak, H. Petek, K. Ishioka, E. M. Thatcher, and C. J. Stanton, *Physical Review B* **91**, 125201 (2015).
- ¹⁶⁰J. Sjakste, N. Vast, and V. Tyuterev, *Physical Review Letters* **99**, 236405 (2007).
- ¹⁶¹H. J. Zeiger, J. Vidal, T. K. Cheng, E. P. Ippen, G. Dresselhaus, and M. S. Dresselhaus, *Physical Review B* **45**, 768–778 (1992).
- ¹⁶²G. Xiong, R. Shao, T. C. Droubay, A. G. Joly, K. M. Beck, S. A. Chambers, and W. P. Hess, *Advanced Functional Materials* **17**, 2133–2138 (2007).
- ¹⁶³V. V. Temnov, G. Armelles, U. Woggon, D. Guzatov, A. Cebollada, A. Garcia-Martin, J.-M. Garcia-Martin, T. Thomay, A. Leitenstorfer, and R. Bratschitsch, *Nature Photonics* **4**, 107–111 (2010).
- ¹⁶⁴W. Zheng, X. Liu, A. T. Hanbicki, B. T. Jonker, and G. Lüpke, *Optical Materials Express* **5**, 2597 (2015).
- ¹⁶⁵H. Hopster and H. P. Oepen, eds., 1st ed, *Nanoscience and Technology 1434-4904* (Springer, Berlin ; New York, 2004).
- ¹⁶⁶A. Hubert and R. Schäfer, *Magnetic domains: the analysis of magnetic microstructures* (Springer, Berlin ; New York, 1998).
- ¹⁶⁷J. Stöhr and H. C. Siegmann, *Magnetism: from fundamentals to nanoscale dynamics*, Springer Series in Solid-State Sciences 152 (Springer, Berlin ; New York, 2006).
- ¹⁶⁸J. L. Morán-López, *Physics of low dimensional systems* (Kluwer Academic / Plenum Publishers, 2001).
- ¹⁶⁹G. Schönhense, K. Medjanik, and H.-J. Elmers, *Journal of Electron Spectroscopy and Related Phenomena* **200**, 94–118 (2015).
- ¹⁷⁰C. Tusche, M. Ellguth, A. A. Ünal, C.-T. Chiang, A. Winkelmann, A. Krasnyuk, M. Hahn, G. Schönhense, and J. Kirschner, *Applied Physics Letters* **99**, 032505 (2011).
- ¹⁷¹G. K. L. Marx, H. J. Elmers, and G. Schönhense, *Physical Review Letters* **84**, 5888–5891 (2000).
- ¹⁷²G. K. L. Marx, P.-O. Jubert, A. Bischof, and R. Allenspach, *Applied Physics Letters* **83**, 2925–2927 (2003).

- ¹⁷³T. Nakagawa and T. Yokoyama, *Physical Review Letters* **96**, 237402 (2006).
- ¹⁷⁴K. Hild, J. Maul, T. Meng, M. Kallmayer, G. Schönhense, H. J. Elmers, R. Ramos, S. K. Arora, and I. V. Shvets, *Journal of Physics: Condensed Matter* **20**, 235218 (2008).
- ¹⁷⁵K. Hild, J. Maul, G. Schönhense, H. J. Elmers, M. Amft, and P. M. Oppeneer, *Physical Review Letters* **102**, 057207 (2009).
- ¹⁷⁶K. Hild, G. Schönhense, H. J. Elmers, T. Nakagawa, T. Yokoyama, K. Tarafder, and P. M. Oppeneer, *Physical Review B* **82**, 195430 (2010).
- ¹⁷⁷K. Hild, G. Schönhense, H. J. Elmers, T. Nakagawa, T. Yokoyama, K. Tarafder, and P. M. Oppeneer, *Physical Review B* **85**, 014426 (2012).
- ¹⁷⁸T. Nakagawa, T. Yokoyama, M. Hosaka, and M. Katoh, *Rev. Sci. Instrum.*, **6** (2007).
- ¹⁷⁹T. Nakagawa and T. Yokoyama, *Journal of Electron Spectroscopy and Related Phenomena* **185**, 356–364 (2012).
- ¹⁸⁰M. Kronseder, J. Minár, J. Braun, S. Günther, G. Woltersdorf, H. Ebert, and C. H. Back, *Physical Review B* **83**, 132404 (2011).
- ¹⁸¹T. N. G. Meier, M. Kronseder, and C. H. Back, *Physical Review B* **96**, 144408 (2017).
- ¹⁸²T. Taniuchi, Y. Kotani, and S. Shin, *Review of Scientific Instruments* **86**, 023701 (2015).
- ¹⁸³T. Taniuchi, Y. Motoyui, K. Morozumi, T. C. Rödel, F. Fortuna, A. F. Santander-Syro, and S. Shin, *Nature Communications* **7**, 11781 (2016).
- ¹⁸⁴Y. Zhao, H. Lyu, G. Yang, B. Dong, J. Qi, J. Zhang, Z. Zhu, Y. Sun, G. Yu, Y. Jiang, H. Wei, J. Wang, J. Lu, Z. Wang, J. Cai, B. Shen, W. Zhan, F. Yang, S. Zhang, and S. Wang, *Ultramicroscopy* **202**, 156–162 (2019).
- ¹⁸⁵W. Zheng, P. Jiang, L. Zhang, Y. Wang, Q. Sun, Y. Liu, Q. Gong, and C. Wu, *Review of Scientific Instruments* **92**, 043709 (2021).
- ¹⁸⁶M. A. Ruderman and C. Kittel, *Physical Review* **96**, 99–102 (1954).
- ¹⁸⁷T. Kasuya, *Progress of Theoretical Physics* **16**, 45–57 (1956).
- ¹⁸⁸K. Yosida, *Physical Review* **106**, 893–898 (1957).
- ¹⁸⁹W. Pauli, *Physik* **43**, 601–623 (1927).
- ¹⁹⁰E. C. Stoner and E. P. Wohlfarth, *Philosophical Transactions of the Royal Society of London. Series A, Mathematical and Physical Sciences* **240**, 599 (1948).
- ¹⁹¹C. Kittel, *Reviews of Modern Physics* **21**, 541–583 (1949).
- ¹⁹²W. H. Meiklejohn and C. P. Bean, *Physical Review* **102**, 1413–1414 (1956).

- ¹⁹³A. Vansteenkiste, J. Leliaert, M. Dvornik, M. Helsen, F. Garcia-Sanchez, and B. Van Waeyenberge, *AIP Advances* **4**, 107133 (2014).
- ¹⁹⁴R. F. L. Evans, W. J. Fan, P. Chureemart, T. A. Ostler, M. O. A. Ellis, and R. W. Chantrell, *Journal of Physics: Condensed Matter* **26**, 103202 (2014).
- ¹⁹⁵G. Schönhense, *Journal of Physics: Condensed Matter* **11**, 9517–9547 (1999).
- ¹⁹⁶P. M. Oppeneer, T. Maurer, J. Sticht, and J. Kübler, *Physical Review B* **45**, 10924–10933 (1992).
- ¹⁹⁷J. Sass, *Surface Science* **51**, 199–212 (1975).
- ¹⁹⁸J. L. Erskine and E. A. Stern, *Physical Review B* **8**, 1239–1255 (1973).
- ¹⁹⁹R. Feder and J. Henk, in *Spin-Orbit-Influenced Spectroscopies of Magnetic Solids*, Vol. 466, edited by H. Ebert and G. Schütz, red. by H. Araki, E. Brézin, J. Ehlers, U. Frisch, K. Hepp, R. L. Jaffe, R. Kippenhahn, H. A. Weidenmüller, J. Wess, J. Zittartz, and W. Beiglböck, *Lecture Notes in Physics* (Springer Berlin Heidelberg, Berlin, Heidelberg, 1996), pp. 85–104.
- ²⁰⁰J. Henk, T. Scheunemann, S. V. Halilov, and R. Feder, *Journal of Physics: Condensed Matter* **8**, 47–65 (1996).
- ²⁰¹W. Kuch, A. Dittschar, K. Meinel, M. Zharnikov, C. M. Schneider, J. Kirschner, J. Henk, and R. Feder, *Physical Review B* **53**, 11621–11630 (1996).
- ²⁰²D. Venus, *Physical Review B* **49**, 8821–8829 (1994).
- ²⁰³D. Venus, *Journal of Magnetism and Magnetic Materials* **170**, 29–39 (1997).
- ²⁰⁴E. Tamura, W. Piepke, and R. Feder, *Physical Review Letters* **59**, 934–937 (1987).
- ²⁰⁵E. P. Wigner, *Communications on Pure and Applied Mathematics* **13**, 1–14 (1960).
- ²⁰⁶W. Kuch, A. Dittschar, K. Meinel, M. Zharnikov, C. M. Schneider, J. Kirschner, J. Henk, and R. Feder, *Physical Review B* **53**, 11621–11630 (1996).
- ²⁰⁷J. Henk and B. Johansson, *Journal of Electron Spectroscopy and Related Phenomena* **94**, 259–270 (1998).
- ²⁰⁸W. Kuch, J. Gilles, S. S. Kang, S. Imada, S. Suga, and J. Kirschner, *Physical Review B* **62**, 3824–3833 (2000).
- ²⁰⁹C. Klein, R. Ramchal, A. K. Schmid, and M. Farle, *Physical Review B* **75**, 193405 (2007).
- ²¹⁰S. van Dijken, R. Vollmer, B. Poelsema, and J. Kirschner, *Journal of Magnetism and Magnetic Materials* **210**, 316–328 (2000).
- ²¹¹W. L. O’Brien, T. Droubay, and B. P. Tonner, *Physical Review B* **54**, 9297–9303 (1996).

- ²¹²S. Müller, B. Schulz, G. Kostka, M. Farle, K. Heinz, and K. Baberschke, *Surface Science* **364**, 235–241 (1996).
- ²¹³M.-T. Lin, J. Shen, W. Kuch, H. Jenniches, M. Klaua, C. M. Schneider, and J. Kirschner, *Physical Review B* **55**, 5886–5897 (1997).
- ²¹⁴D. A. Porter and K. E. Easterling, *Phase transformations in metals and alloys* (Springer US, Boston, MA, 1992).
- ²¹⁵H. P. Oepen and J. Kirschner, *Physical Review Letters* **62**, 819–822 (1989).
- ²¹⁶D. Tomalin and C. McMahon, *Materials Science and Engineering* **8**, 54–56 (1971).
- ²¹⁷H. Grabke, W. Paulitschke, G. Tauber, and H. Viefhaus, *Surface Science* **63**, 377–389 (1977).
- ²¹⁸M. A. Fresnel, *Mémoire sur la loi des modifications que la réflexion imprime à la lumière polarisée* (Academie des sciences, 1823).
- ²¹⁹J. H. Weaver, C. G. Olson, and D. W. Lynch, *Physical Review B* **15**, 4115–4118 (1977).
- ²²⁰H. Huang, X.-y. Zhu, and J. Hermanson, *Physical Review B* **29**, 2270–2273 (1984).
- ²²¹G. Doyen, *Surface Science* **122**, 505–518 (1982).
- ²²²J. Hong, R. Q. Wu, J. Lindner, E. Kosubek, and K. Baberschke, *Physical Review Letters* **92**, 147202 (2004).
- ²²³R. H. Wade, *Proceedings of the Physical Society* **79**, 1237–1244 (1962).
- ²²⁴B. Lilley, *The London, Edinburgh, and Dublin Philosophical Magazine and Journal of Science* **41**, 792–813 (1950).
- ²²⁵A. Michels, J. Weissmüller, A. Wiedenmann, and J. G. Barker, *Journal of Applied Physics* **87**, 5953–5955 (2000).
- ²²⁶K. Niitsu, *Journal of Physics D: Applied Physics* **53**, 39LT01 (2020).
- ²²⁷O. Hjortstam, K. Baberschke, J. M. Wills, B. Johansson, and O. Eriksson, *Physical Review B* **55**, 15026–15032 (1997).
- ²²⁸T. N. G. Meier, M. Kronseder, M. Zimmermann, and C. H. Back, *Physical Review B* **93**, 064424 (2016).
- ²²⁹H. J. Hug, B. Stiefel, A. Moser, I. Parashikov, A. Klicznik, D. Lipp, H.-J. Güntherodt, G. Bochi, D. I. Paul, and R. C. O’Handley, *Journal of Applied Physics* **79**, 5609 (1996).
- ²³⁰P. Sparks, N. Stern, D. Snowden, B. Kappus, J. Checkelsky, S. Harberger, A. Fusello, and J. Eckert, *Journal of Magnetism and Magnetic Materials* **272–276**, E1339–E1340 (2004).

- ²³¹S. Hameed, P. Talagala, R. Naik, L. E. Wenger, V. M. Naik, and R. Proksch, *Physical Review B* **64**, 184406 (2001).
- ²³²D. M. Gottlob, H. Doğanay, F. Nickel, S. Cramm, I. P. Krug, S. Nemšák, and C. M. Schneider, *Ultramicroscopy* **159**, 503–507 (2015).
- ²³³B. Kaplan and G. Gehring, *Journal of Magnetism and Magnetic Materials* **128**, 111–116 (1993).
- ²³⁴G. Bochi, H. J. Hug, D. I. Paul, B. Stiefel, A. Moser, I. Parashikov, H.-J. Güntherodt, and R. C. O’Handley, *Physical Review Letters* **75**, 1839–1842 (1995).
- ²³⁵W. Kuch, M. Zharnikov, A. Dittschar, K. Meinel, C. M. Schneider, J. Kirschner, J. Henk, and R. Feder, *Journal of Applied Physics* **79**, 6426 (1996).
- ²³⁶S. V. Halilov, E. Tamura, D. Meinert, H. Gollisch, and R. Feder, *Journal of Physics: Condensed Matter* **5**, 3859–3870 (1993).
- ²³⁷W. Kuch, A. Dittschar, M. Salvietti, M.-T. Lin, M. Zharnikov, C. M. Schneider, J. Camarero, J. J. de Miguel, R. Miranda, and J. Kirschner, *Physical Review B* **57**, 5340–5346 (1998).
- ²³⁸T. Nakagawa, I. Yamamoto, Y. Takagi, and T. Yokoyama, *Journal of Electron Spectroscopy and Related Phenomena* **181**, 164–167 (2010).
- ²³⁹H. Kawano, *Progress in Surface Science*, 100583 (2021).
- ²⁴⁰H. Kawano, *Progress in Surface Science* **83**, 1–165 (2008).
- ²⁴¹P. Błoński, A. Kiejna, and J. Hafner, *Surface Science* **590**, 88–100 (2005).
- ²⁴²H. W. Hugosson, W. Cao, S. Seetharaman, and A. Delin, *The Journal of Physical Chemistry C* **117**, 6161–6171 (2013).
- ²⁴³R. Feder, *Journal of Physics C: Solid State Physics* **14**, 2049–2091 (1981).
- ²⁴⁴F. Giebels, H. Gollisch, R. Feder, F. O. Schumann, C. Winkler, and J. Kirschner, *Physical Review B* **84**, 165421 (2011).
- ²⁴⁵J. A. Stroscio, D. T. Pierce, A. Davies, R. J. Celotta, and M. Weinert, *Physical Review Letters* **75**, 2960–2963 (1995).
- ²⁴⁶M. M. J. Bischoff, T. K. Yamada, C. M. Fang, R. A. de Groot, and H. van Kempen, *Physical Review B* **68**, 045422 (2003).
- ²⁴⁷V. Baltz, A. Manchon, M. Tsoi, T. Moriyama, T. Ono, and Y. Tserkovnyak, *Reviews of Modern Physics* **90**, 015005 (2018).
- ²⁴⁸J. H. Mentink, *Journal of Physics: Condensed Matter* **29**, 453001 (2017).
- ²⁴⁹W. L. Roth, *Journal of Applied Physics* **31**, 2000–2011 (1960).

- ²⁵⁰F. U. Hillebrecht, H. Ohldag, N. B. Weber, C. Bethke, U. Mick, M. Weiss, and J. Bahrtdt, *Physical Review Letters* **86**, 3419–3422 (2001).
- ²⁵¹N. Weber, C. Bethke, and F. Hillebrecht, *Journal of Magnetism and Magnetic Materials* **226–230**, 1573–1576 (2001).
- ²⁵²N. B. Weber, H. Ohldag, H. Gomonaj, and F. U. Hillebrecht, *Physical Review Letters* **91**, 237205 (2003).
- ²⁵³M. van Veghel and P. Zeijlmans van Emmichoven, *Journal of Magnetism and Magnetic Materials* **311**, 565–577 (2007).
- ²⁵⁴J. Stöhr, A. Scholl, T. J. Regan, S. Anders, J. Lüning, M. R. Scheinfein, H. A. Padmore, and R. L. White, *Physical Review Letters* **83**, 4 (1999).
- ²⁵⁵M. Fiebig, D. Fröhlich, T. Lottermoser, V. V. Pavlov, R. V. Pisarev, and H.-J. Weber, *Physical Review Letters* **87**, 137202 (2001).
- ²⁵⁶M. Nývlt, F. Bisio, and J. Kirschner, *Physical Review B* **77**, 014435 (2008).
- ²⁵⁷K. Arai, T. Okuda, A. Tanaka, K. Fukumoto, T. Hasegawa, T. Nakamura, T. Matsushita, T. Muro, A. Kakizaki, and T. Kinoshita, *Journal of Applied Physics* **110**, 084306 (2011).
- ²⁵⁸Y. Meng, J. Li, A. Tan, E. Jin, J. Son, J. S. Park, A. Doran, A. T. Young, A. Scholl, E. Arenholz, J. Wu, C. Hwang, H. W. Zhao, and Z. Q. Qiu, *Applied Physics Letters* **98**, 212508 (2011).
- ²⁵⁹F. Nolting, A. Scholl, J. Stöhr, J. W. Seo, J. Fompeyrine, H. Siegart, J.-P. Locquet, S. Anders, J. Lüning, E. E. Fullerton, M. F. Toney, M. R. Scheinfein, and H. A. Padmore, *Nature* **405**, 767–769 (2000).
- ²⁶⁰A. Scholl, J. Stöhr, J. Lüning, J. W. Seo, J. Fompeyrine, H. Siegart, J.-P. Locquet, F. Nolting, S. Anders, E. E. Fullerton, M. R. Scheinfein, and H. A. Padmore, *Science* **287**, 1014–1016 (2000).
- ²⁶¹A. Scholl, F. Nolting, J. W. Seo, H. Ohldag, J. Stöhr, S. Raoux, J.-P. Locquet, and J. Fompeyrine, *Applied Physics Letters* **85**, 4085–4087 (2004).
- ²⁶²T. Zhao, A. Scholl, F. Zavaliche, K. Lee, M. Barry, A. Doran, M. P. Cruz, Y. H. Chu, C. Ederer, N. A. Spaldin, R. R. Das, D. M. Kim, S. H. Baek, C. B. Eom, and R. Ramesh, *Nature Materials* **5**, 823–829 (2006).
- ²⁶³M. S. Lee, P. Lyu, R. V. Chopdekar, A. Scholl, S. T. Retterer, and Y. Takamura, *Journal of Applied Physics* **127**, 203901 (2020).
- ²⁶⁴A. A. Sapozhnik, M. Filianina, S. Y. Bodnar, A. Lamirand, M.-A. Mawass, Y. Skourski, H.-J. Elmers, H. Zabel, M. Kläui, and M. Jourdan, *Physical Review B* **97**, 134429 (2018).

- ²⁶⁵Z. Zhang and J. T. Yates, *Chemical Reviews* **112**, 5520–5551 (2012).
- ²⁶⁶K. Sell, I. Barke, S. Polei, C. Schumann, V. von Oeynhausen, and K.-H. Meiwes-Broer, *physica status solidi (b)* **247**, 1087 (2010).
- ²⁶⁷L. Kronik and Y. Shapira, *Surface Science Reports* **37**, 1–206 (1999).
- ²⁶⁸J. P. Long and V. M. Bermudez, *Physical Review B* **66**, 121308 (2002).
- ²⁶⁹N. R. Huck, R. S. C. Smart, and S. M. Thurgate, *Surface science* **169**, 245–252 (1986).
- ²⁷⁰C. Denker, S. Nielsen, E. Lage, M. Römer-Stumm, H. Heyen, Y. Junk, J. Walowski, K. Waldorf, and M. Münzenberg, (2020) <https://arxiv.org/abs/2011.07336>.
- ²⁷¹J. Gorchon, R. B. Wilson, Y. Yang, A. Pattabi, J. Y. Chen, L. He, J. P. Wang, M. Li, and J. Bokor, *Physical Review B* **94**, 184406 (2016).
- ²⁷²L. Le Guyader, M. Savoini, S. El Moussaoui, M. Buzzi, A. Tsukamoto, A. Itoh, A. Kirilyuk, T. Rasing, A. V. Kimel, and F. Nolting, *Nature Communications* **6**, 1–6 (2015).
- ²⁷³D. Bauer, K. Papp, J. Polimeni, K. Mayumi, M. Giampietro, and B. Alcott, *Sustainability: Science, Practice and Policy* **5**, 48–54 (2009).
- ²⁷⁴R. Feder, W. Gudat, E. Kisker, A. Rodriguez, and K. Schröder, *Solid state communications* **46**, 619 (1983).
- ²⁷⁵R. Reitinger, B. Sepiol, G. Vogl, B. Pfau, L.-M. Stadler, S. Stankov, F. Zontone, N. Spiridis, and J. Korecki, *Journal of Applied Physics* **102**, 034310 (2007).
- ²⁷⁶J. Lawler, R. Schad, S. Jordan, and H. van Kempen, *Journal of Magnetism and Magnetic Materials* **165**, 224–226 (1997).
- ²⁷⁷S. M. Jordan, J. F. Lawler, R. Schad, and H. van Kempen, *Journal of Applied Physics* **84**, 1499–1503 (1998).
- ²⁷⁸G. Fahsold, A. Priebe, and A. Pucci, *Applied Physics A Materials Science & Processing* **73**, 39–43 (2001).
- ²⁷⁹J. Henk, W. Schattke, H. Cartensen, R. Manzke, and M. Skibowski, *Physical Review B* **47**, 2251–2264 (1993).
- ²⁸⁰W. S. M. Werner, K. Glantschnig, and C. Ambrosch-Draxl, *Journal of Physical and Chemical Reference Data* **38**, 1013–1092 (2009).

The layout of this thesis is based on a LaTeX template from [LaTeXTemplates.com](http://www.LaTeXTemplates.com). Version 2.x major modifications were done by Vel (vel@latextemplates.com). This template is based on a template by Steve Gunn (<http://users.ecs.soton.ac.uk/srg/softwaretools/document/templates/>) and Sunil Patel (<http://www.sunilpatel.co.uk/thesis-template/>) and is licensed by CC BY-NC-SA 3.0 (<http://creativecommons.org/licenses/by-nc-sa/3.0/>).

Curriculum Vitae

Personal Information

Name: Maximilian Paleschke
Date of Birth: 16.01.1994
Place of Birth: Halle (Saale)
Gender: Male
Address: [REDACTED]
Citizenship: German

Education

- since 2018 PhD Studies at Martin Luther University
Halle-Wittenberg in the Surface Science group
Part of the Collaborative Research Center with FU Berlin
„CRC/TRR 227: Ultrafast Spin Dynamics“
PhD Thesis: „Dichroic Photoemission Electron Microscopy
Imaging of Magnetic Surfaces“
Supervisor: Prof. Dr. Wolf Widdra
Member of the *Integrated research and
training group* of the SFB/TRR 227
- 2015 - 2017 Master Studies at Martin Luther University
Halle-Wittenberg in the Nanostructured Materials group
Master Thesis: „Ferromagnetic Resonance and
Spin Waves in YIG nanostructures“
Supervisor: Prof. Dr. Georg Schmidt
Degree: Master of Science in Physics, Score: 1.1
- 2012 - 2015 Bachelor Studies at Martin Luther University
Halle-Wittenberg in the Nanostructured Materials group
Bachelor Thesis: „Spin pumping and inverse spin Hall
effect in oxide heterostructures“
Supervisor: Prof. Dr. Georg Schmidt
Degree: Bachelor of Science in Physics, Score: 1.6
- 2004 - 2012 Gymnasium Landsberg
in Landsberg
Degree: Abitur, Score: 1.0

Employment and extracurricular activities

- since 2018 Co-Founder of *Dezernat Zukunft e.V.*
(Macro-economic and finance think-tank in Berlin)
- since 2018 PhD representative of the CRC/TRR 227
- 2016 - 2018 Student Senator at Martin Luther University
Halle-Wittenberg
- 2015 - 2017 Founder of academic policy group
D.C. Universe (Diversity Changes University)
- 2017 Internship at Moscow Polytechnical University
in Moscow (Russia)
- 2016 - 2017 Internship at d-fine GmbH in Munich
(Consulting company in risk and finance)
- 2016 - 2017 Research Assistant at Surface Science group
at Martin Luther University Halle-Wittenberg
- 2015 - 2016 Research Assistant at Fraunhofer Center
for Silicon Photovoltaics in Halle

Signed:

Date:

List of publications

1. **M. Paleschke**, C.-T. Chiang, L. Brandt, N. Liebing, G. Woltersdorf, and W. Widdra: *Plasmonic spin-Hall effect of propagating surface plasmon polaritons in $Ni_{80}Fe_{20}$ microstructures*, *New Journal of Physics*, **23**, 9, 093006, 2021.
2. G. Schmidt, C. Hauser, P. Trempler, **M. Paleschke**, and E. T. Papaioannou: *Ultra thin films of yttrium iron garnet with very low damping: A review*, *Physica Status Solidi B*, 1900644, 2020.
3. T. Richter, **M. Paleschke**, M. Wahler, F. Heyroth, H. Deniz, D. Hesse, and G. Schmidt: *Spin pumping and inverse spin-Hall effect in ultrathin $SrRuO_3$ films around the percolation limit*, *Physical Review B* **96**, 18, 184407, 2017.
4. S. Schenk, S. Förster, K. Meinel, R. Hammer, B. Leibundgut, **M. Paleschke**, J. Pantzer, C. Dresler, F. O. Schumann, and W. Widdra: *Observation of a dodecagonal oxide quasicrystal and its complex approximant in the $SrTiO_3$ -Pt (111) system*, *Journal of Physics: Condensed Matter* **29**, 13, 134002, 2017.

Acknowledgements

I want to thank the whole Surface Science group as well as all the colleagues at the CRC/TRR 227 and the corresponding Research School for helping me to complete this thesis. Such a work is always a team effort and would not be possible without the support of many excellent scientists. Especially, I want to highlight the following people:

My supervisor Prof. Dr. Wolf WIDDRA for giving me the opportunity to write this thesis in his group and supporting me with everything needed in order to complete it. I want to specially thank him for the trust put into me and the freedom he gave me in finding my own way to completing this thesis. The sheer scope of the project, whilst intimidating, gave me the opportunity to design a very complex experiment from scratch, which is an experience not many experimentalists can gather. Additionally, I want to thank him for all the conferences I had the pleasure to visit and share my ideas and results with the field, which again shows an anticipation of trust towards me I am very happy to have witnessed.

My colleague and former principal investigator of the laser project Dr. Cheng-Tien Chiang for his didactically superb council over the years, his many experimental ideas and literature knowledge, as well as proofreading this thesis. Also, without his tremendous effort in writing the initial proposal, my PhD position probably would not have been funded.

Ralf Kulla for his overall technical support. Especially at the building phase of the project, he had a large impact in making this experiment a reality. Without him, I would probably still have to deal with ordinary UHV problems, and the setup would not have delivered such nice data so soon, if any. I want to also thank the whole workshop team of the university, who made a remarkably great job in supporting the setup of the experiment.

My former and current colleagues dealing with the laser setup, namely Dr. Konrad Gillmeister, Robin Kamrla, Friederike Wührl and Matthias Augstein.

Dr. Frank Schumann for his continuous experimental and theoretical support. Regardless of MOKE, MBE, LEED, PES or any other surface science technique, his knowledge in the field enriched this thesis immensely.

XXX

Dr. Jürgen Henk for the support regarding the Omni simulations as well as providing the potentials. The discussions concerning the peculiarities of photoemission are always a pleasure.

Dr. Stefan Förster for proofreading this thesis and always helping me in the lab when I was at the end of my tether. I learned so much from his experimental approaches and his overall mindset.

Liane Brandt and Niklas Liebing for providing the structured permalloy samples as well as MOKE measurements and spare laser chiller. I also want to thank Prof. Dr. Georg Woltersdorf for the support over the years, be it as a TRR mentor, as a reviewer or when writing a paper.

Sebastian Schenk for his IT support and the pleasant time in the office. In general, I want to thank all Surface Science colleagues for the friendly and supportive atmosphere.

David Reiss and Dr. Britta Anstötz for being the best iRTG team possible, and for the guidance and support throughout the years. The exchange through the CRC is something I enjoyed dearly.

My family, who supported me throughout my whole life and in this period as well. I know I can always count on them, which is nothing I take for granted.

And last, but not least, thanks to all my dear friends which kept my sanity over these four years. I can not stress enough, how impossible this endeavor would have been for me if I had not the daily exchange with at least one of you to pull me through this. I will forget some of you (you know who you are), but I will try listing some here. Hugs and love go out to Tamino zum Felde, Alina Schürmann, Robert Reese, Luisa Allermann, Jonas Pantzer, Christine Köchy, Kyra Klocke, Paul Biesold and Judith Lorbach. Huge shout-out also to the whole MACH e.V. team. You created some of my fondest memories of this PhD time. Also, shout-out to the whole Dezernat Zukunft crew, especially the people on the bridge Philippa Sigl-Glöckner, Dr. Max Krahe, Kristina Berthel and Nicolas Gassen. I hope to have all of you by my side for many more years to come, whatever insane project I stumble into next. ♡

Declaration of Authorship

I, Maximilian PALESCHKE, declare that this thesis titled “Dichroic Photoemission Electron Microscopy Imaging of Magnetic Surfaces” and the work presented in it are my own. I confirm that:

- This work was done wholly or mainly while in candidature for a research degree at this University.
- Where any part of this thesis has previously been submitted for a degree or any other qualification at this University or any other institution, this has been clearly stated.
- Where I have consulted the published work of others, this is always clearly attributed.
- Where I have quoted from the work of others, the source is always given. With the exception of such quotations, this thesis is entirely my own work.
- I have acknowledged all main sources of help.
- Where the thesis is based on work done by myself jointly with others, I have made clear exactly what was done by others and what I have contributed myself.

Signed:

Date:
